Basic Theory and Applications of EPR

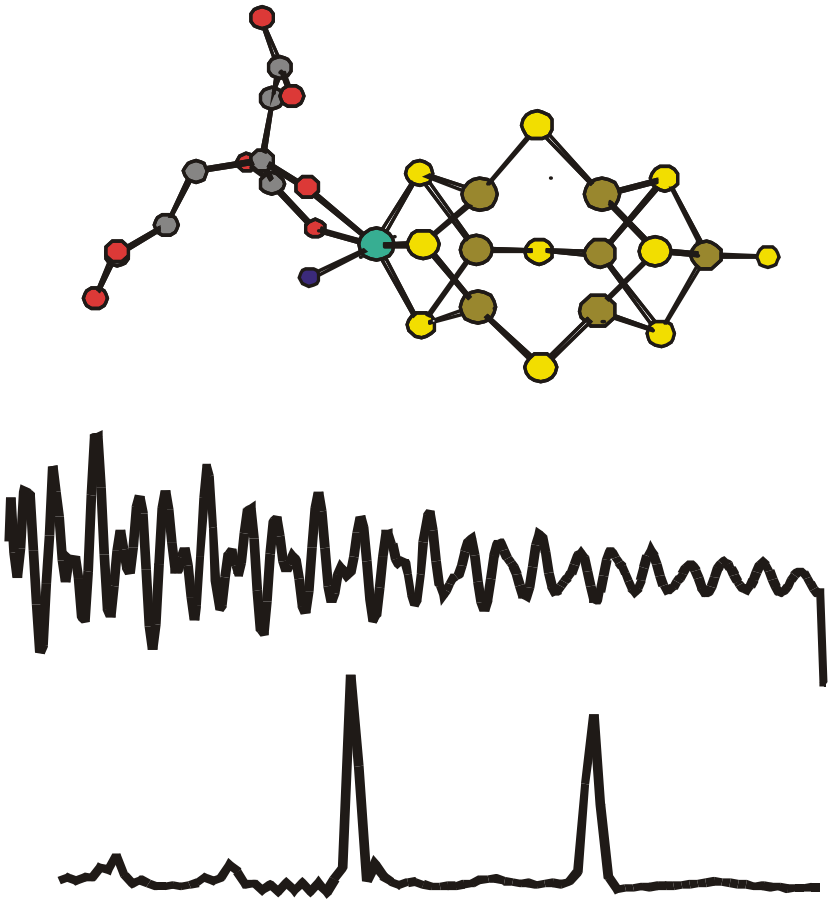

References

Good start: John A. Weil, James R. Bolton, John E. Wertz, ***Electron Paramagnetic Resonance***, John Wiley and Sons, Inc, 1994.

Pulsed EPR: Arthur Schweiger, Gunnar Jeschke, ***Principles of Pulse Electron Paramagnetic Resonance***, Oxford University Press, 2001.

Bit old but still good reference: A. Abragam, B. Bleaney, ***Electron Paramagnetic Resonance of Dransition Ions***, Dover Publications, Inc, 1970.

In hurry ? : Russell S. Drago, ***Physical Methods for Chemists***, Chapters 9, 13, Saunders College Publishing, 1992.

Spin trapping: Rosen, G. M., Britigan, B. E., Halpern, H. J., Pou, S. ***Free Radicals: Biology and Detection by Spin Trapping***. Oxford University Press, 1999

EPR Imaging: Eaton, G. R., Eaton, S. S., Ohno, K. ***EPR imaging and in vivo EPR***: CRC Press, Inc, 1991.

Diamond : M.H.Nazare, A.J. Neves, ***Properties, Growth and Applications of Diamond***: Institution of Engineering and Technology, 2001.

Paramagnec Centers in Si : Subvolume A2a '***Impurities and Defects in Group IV Elements, IV-IV and III-V Compounds. Part a: Group IV Elements***' of Volume 41 'Semiconductors' of Landolt-Börnstein - Group III Condensed Matter: Springer-Verlag, 2002.

The electron has spin, that it rotates !

"But don't you see what this implies? It means that there is a fourth degree of freedom for the electron. It means that the electron has spin, that it rotates."

- George Uhlenbeck to Samuel Goudsmit in 1925 on hearing of the Pauli principle -

(1928, Ann Arbor)

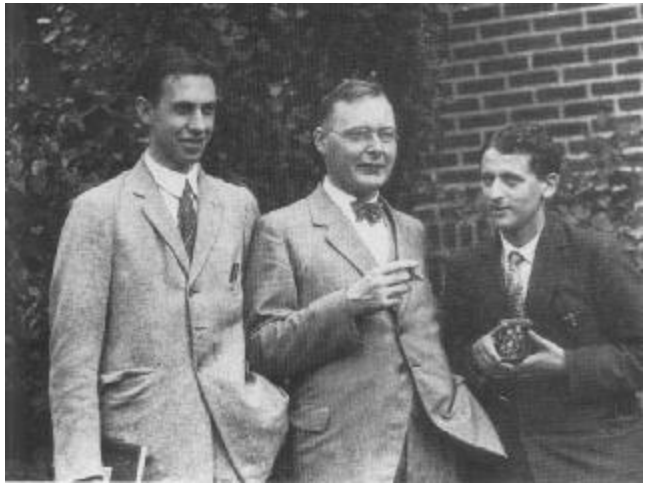

Uhlenbeck Kramer Goudsmit

The first !

Evgeny Konstantinovich Zavoisky
(1907 ~ 1976)

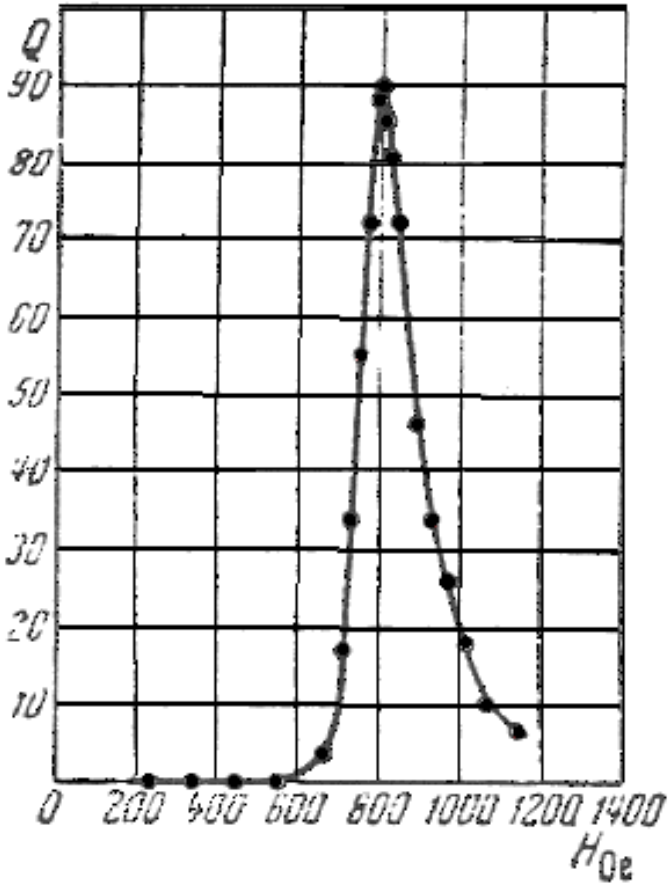

Zavoisky가 1944년에 얻은 최초의 EPR 스펙트럼, Kazan State University
J. Phys. USSR, 9, 1945, 221
(시료: $CuCl_2.2H_2O$, 자장의 세기: 47.6G, 전자기파의 주파수: 133MHz)

The first !

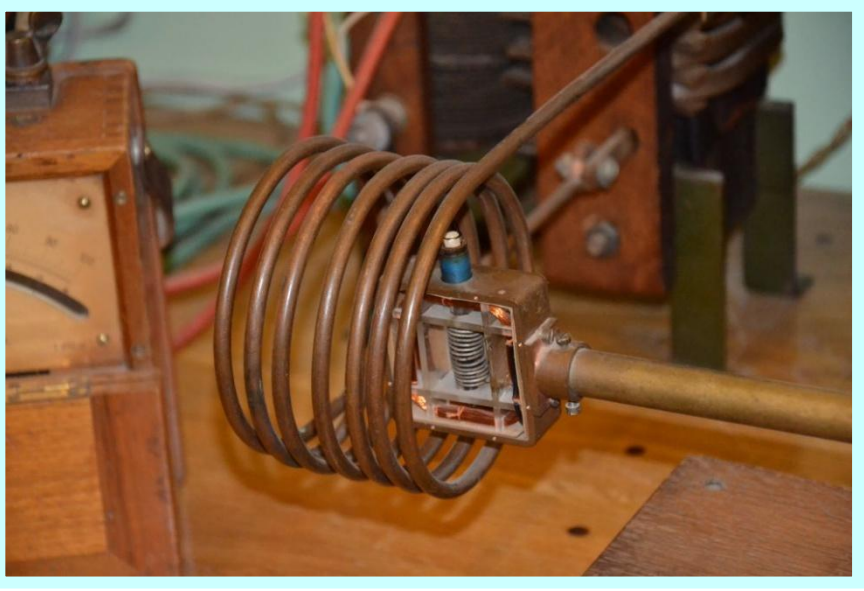

The first !

Brebis Bleaney
(1915 ~ 2006)

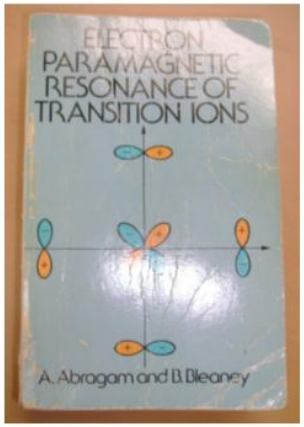

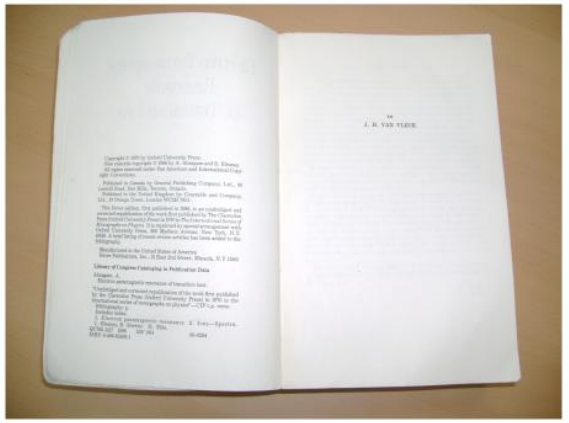

1970

*Independently, the first EPR experiments carried out in **Oxford**, in **1946**, showed that resonance could not be detected at room temperature in many paramagnetic substances. ····· Bleaney's first paper on EPR was published in **1948** ("**Paramagnetic Resonance at Low Temperatures in Chrome Alum**" in Proceedings of the Physical Society) with his colleague Roger Penrose and his second paper in **1949** ("**Paramagnetic Resonance in the Copper Tutton Salts**" in Proceedings of the Royal Society) with Penrose and his student Betty Plumpton, who became Bleaney's wife.*

There are spins everywhere !

인류학
화학반응
연대결정
엑사이톤
지리학
무기라디칼
광물학
고생물학
결점
방사선피해
전이금속
고고학
뭉치화합물
방사선량측정
강자성체
지질학
재료과학
금속함유단백질
유기금속라디칼
고분자
반도체
동물학
생화학
콜로이드
전기화학
범죄과학
유리
의학
현미경
광화학
환경과학
스핀라벨
생물
석탄
EPR 이미징
보석학
역사학
금속화학
유기라디칼
광합성
양자역학
스핀트랩

The spectroscopical techniques !

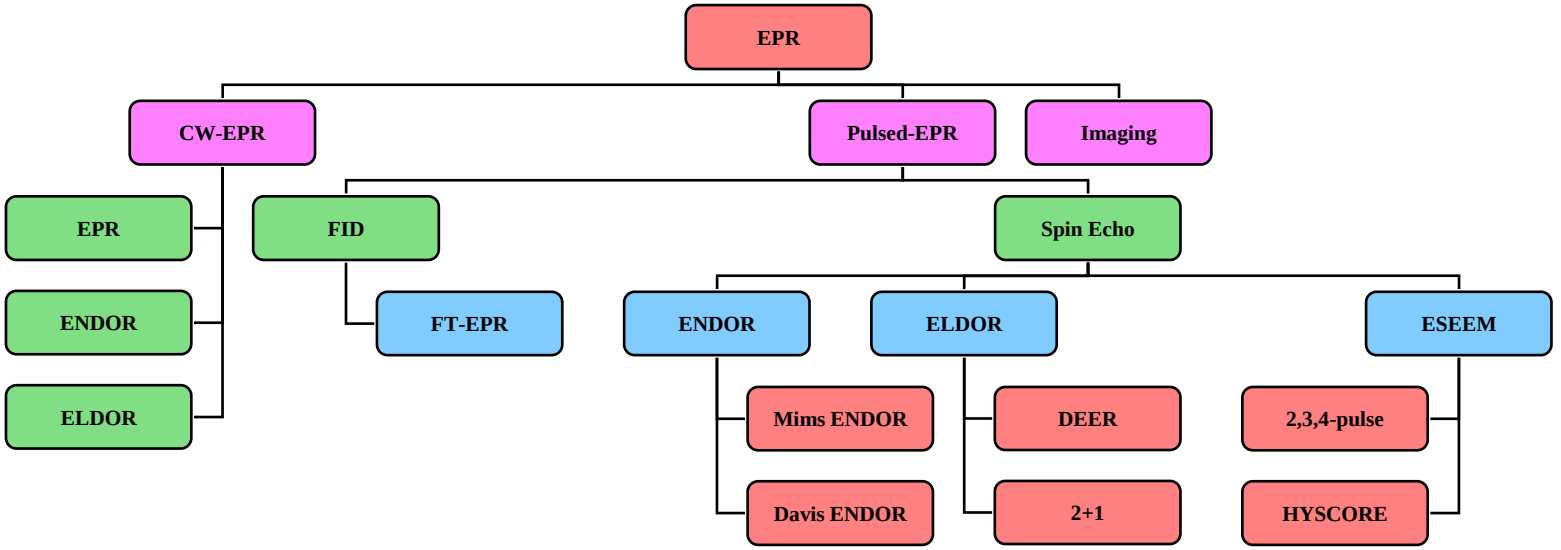

These are just scratches of modern EPR techniques.

Band	Frequency (GHz)	Resonance Field (G)
L	1.1	390
S	4.0	1,400
X	9.75	3,500
Q	34.0	12,000
W	94.0	34,000
higher	260	90,000

... higher and higher
1 THz (~ 35T)

The spectroscopical techniques !

- Meaning of CW –

- Meaning of pulse –

- Meaning of Fourier Transform and Pulse –

- No in the nature => Yes in math => Yes in the nature (What a surprise !!) -

- Magnetization -

- FID –

- Spin Echo (Hahn's echo) –

- Meaning of imaging -

- Why in high field ? -

The tools !

Bruker BioSpin

E680 The FT/CW Spectrometer

e-scan (X-Band)
EMX (X-Band)
E500 The CW Spectrometer (X-Band)
E540 The L-band Imaging Spectrometer
E560 The DICE ENDOR/TRIPLE System
E580 The FT/CW Spectrometer (X-Band)
E600 The CW Spectrometer for W-Band (94 GHz)
E680 The FT/CW Spectrometer (X/W-Band)
Super Q-FT (Q-Band)
Super L-FT (L-Band)
Super S-FT (S-BAnd)
ELDOR
Coherent ELDOR
Stochastic ENDOR

Bruker BioSpin's 263 GHz Project
Pulsed and CW-EPR at Very High-Frequency/High-Field

The tools !

Jeol

JES-FA300

X-band CW:	*JES-FA100*
	JES-FA200
	JES-FA300
X-band pulsed:	*JES-MQ*

.. and (many)$^{\infty}$ other individual labs

What is EPR ?

Electron Pramagnetic Resonance (EPR)
Electron Spin Resonance (ESR)
Electron Magnetic Resonace (EMR)

EPR ~ ESR ~ EMR

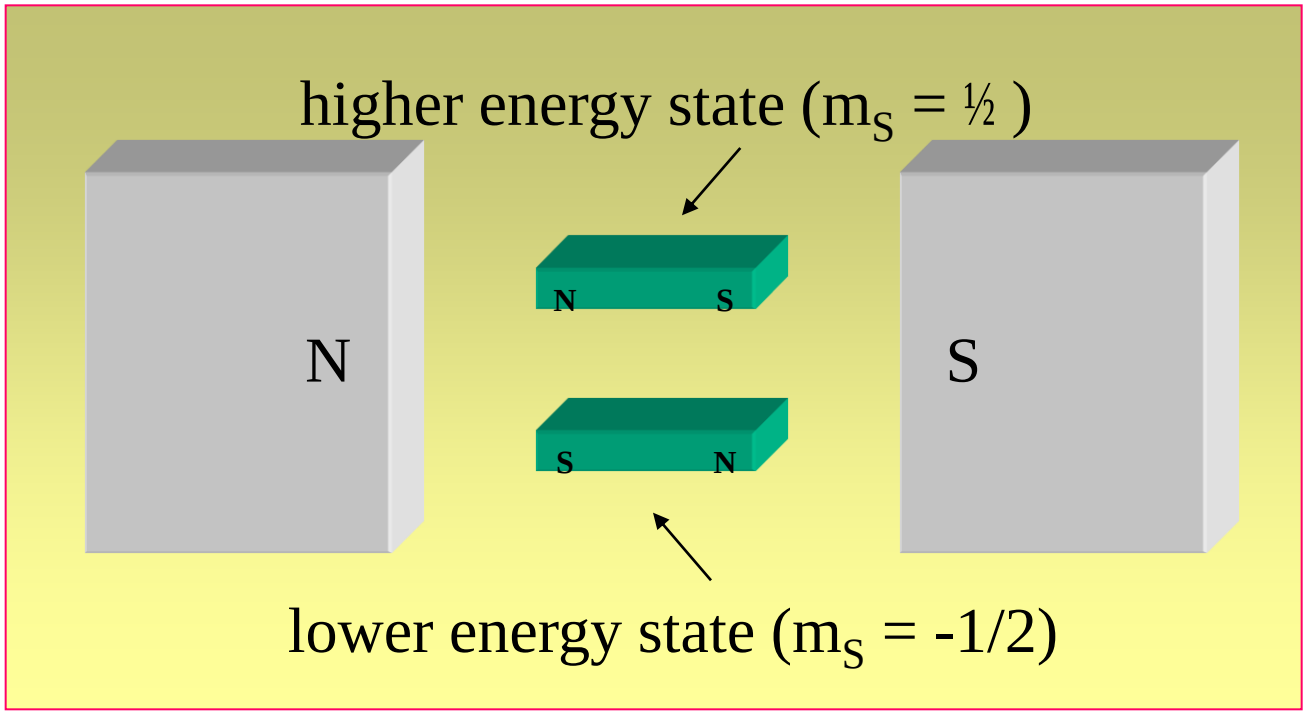

"Electron Zeeman Interaction"

What is EPR ?

EPR is the resonant absorption of microwave radiation
by paramagnetic systems in the presence of an applied magnetic field.

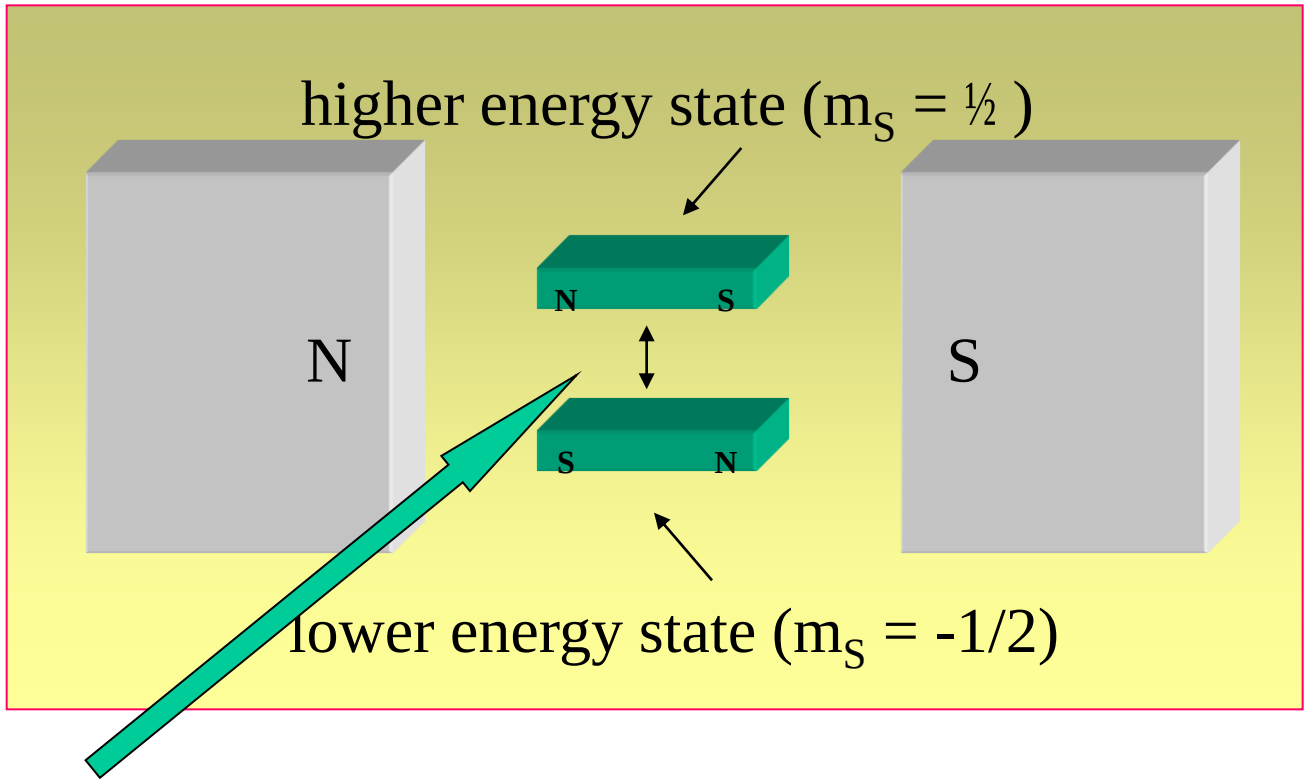

"Electron Zeeman Interaction"

What is EPR ?

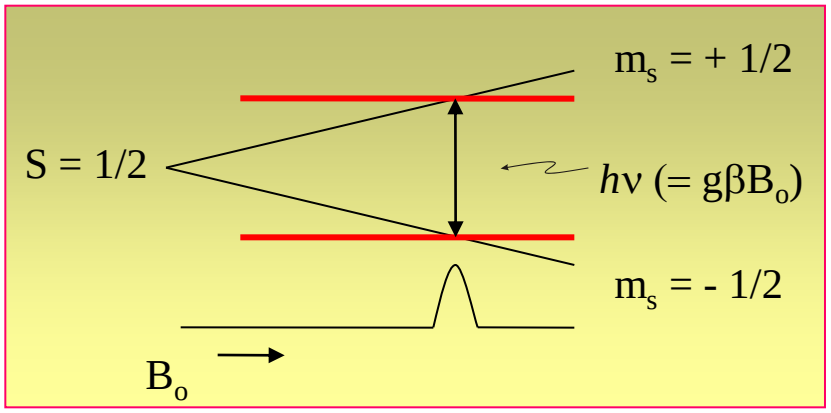

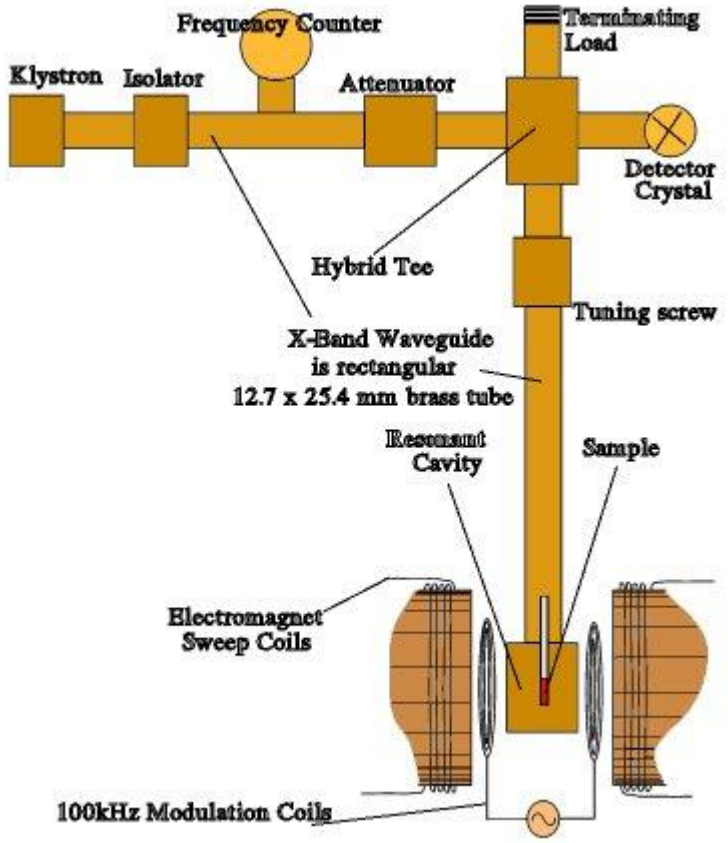

Conventional CW EPR spectrometer Arrangement

- ***h*** Planck's constant (6.626196 x 10^{-27} erg.sec)
- **ν** frequency (GHz or MHz)
- **g** g-factor (approximately 2.0)
- **β** Bohr magneton (9.2741 x 10^{-21} erg.Gauss^{-1})
- $\mathbf{B_o}$ magnetic field (Gauss or mT)

$$H = \beta \mathbf{S} \cdot \mathbf{g} \cdot \mathbf{H}$$

Selection Rule

$\Delta M_S = \pm 1$

"Electron Zeeman Interaction"

EPR Spectrometer - Scheme

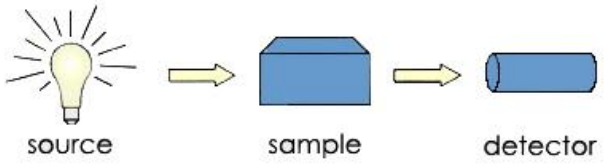

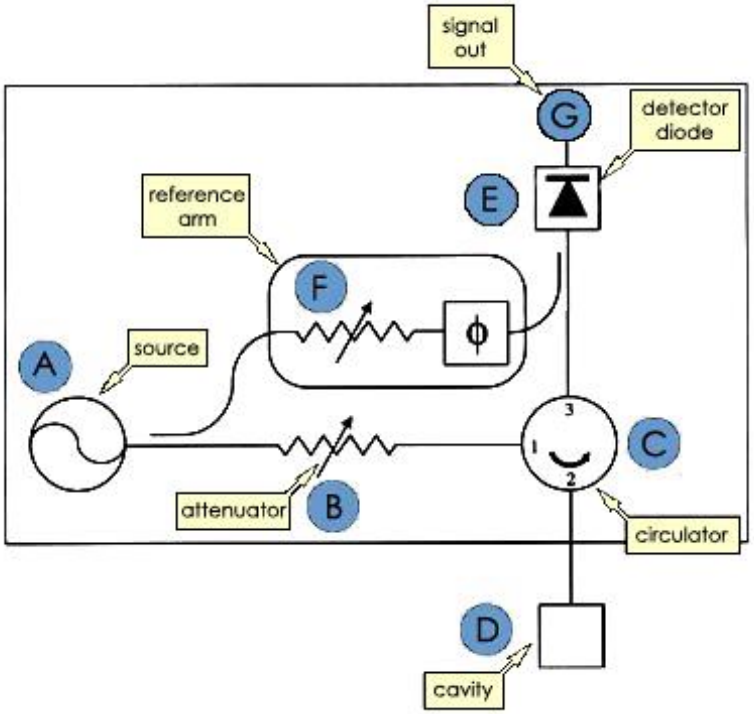

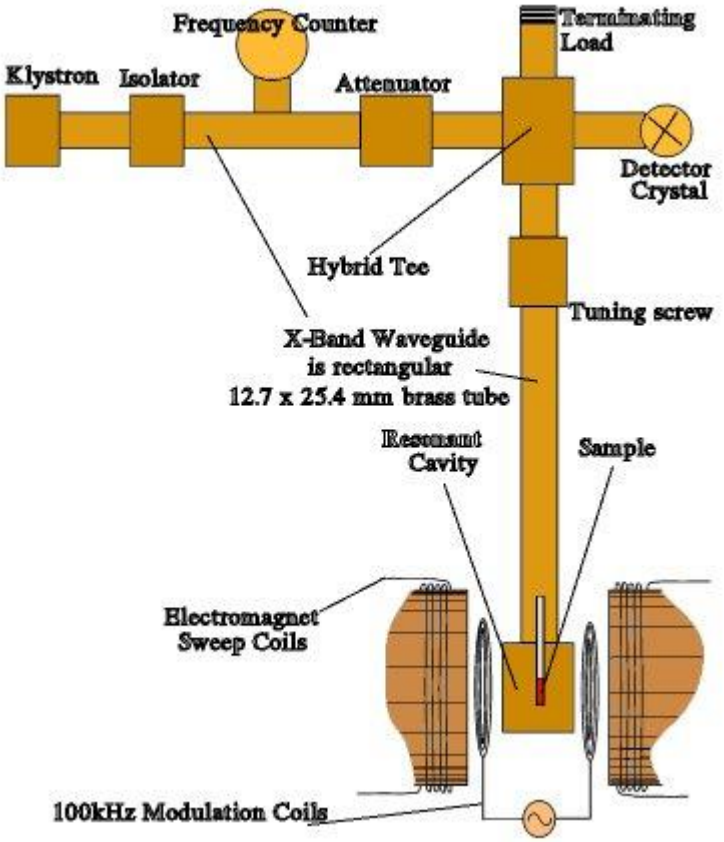

Conventional CW EPR spectrometer Arrangement

- Microwave sources (Klystron, Gunn diode, TWT) – Isolator - Attenuator - Circulator –

EPR Spectrometer - Cavity

Cavities are characterized by their Q or quality factor, which indicates how efficiently the cavity stores microwave energy. As Q increases, the sensitivity of the spectrometer increases. The Q factor is defined as:

$$Q = \frac{2\pi(\text{energy stored})}{\text{energy dissipated per cycle}}, \qquad [5\text{-}1]$$

where the energy dissipated per cycle is the amount of energy lost during one microwave period. Energy can be lost to the side walls of the cavity because the microwaves generate electrical currents in the side walls of the cavity which in turn generates heat. We can measure Q factors easily because there is another way of expressing Q:

$$Q = \frac{\nu_{res}}{\Delta\nu}, \qquad [5\text{-}2]$$

where ν_{res} is the resonant frequency of the cavity and $\Delta\nu$ is the width at half height of the resonance.

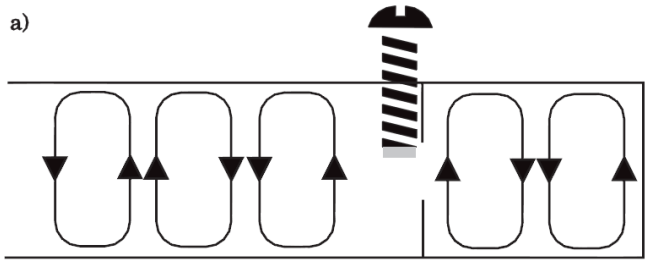

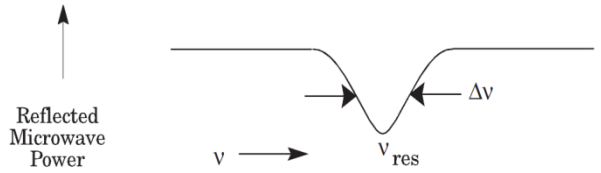

Figure 5-2 Reflected microwave power from a resonant cavity.

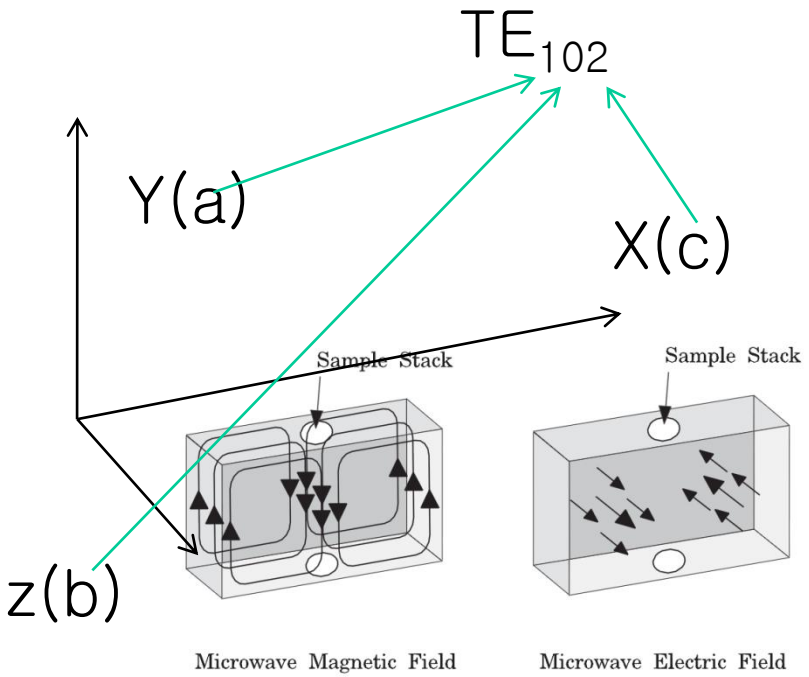

Figure 5-3 Magnetic and electric field patterns in a standard EPR cavity.

EPR Spectrotometer – Detection

- Field modulation and Phase sensitive detection –

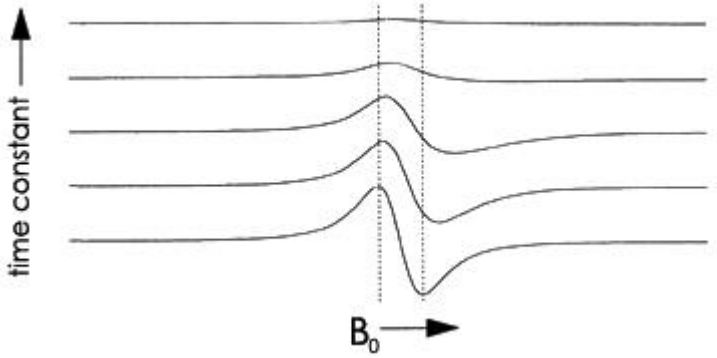

- time constant effect –

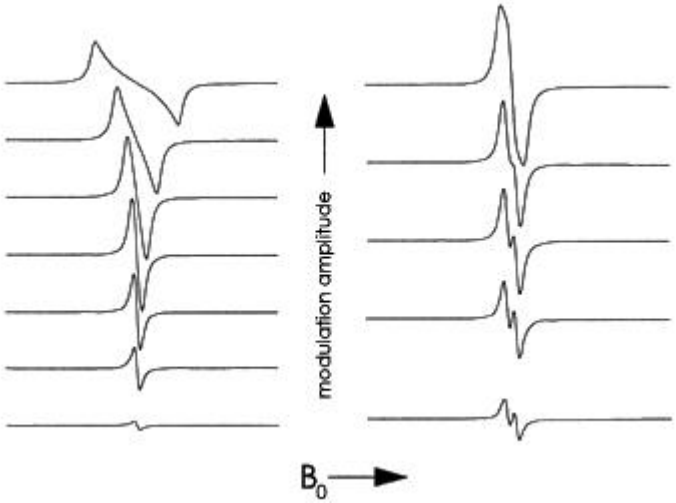

- modulation amplitude effect –

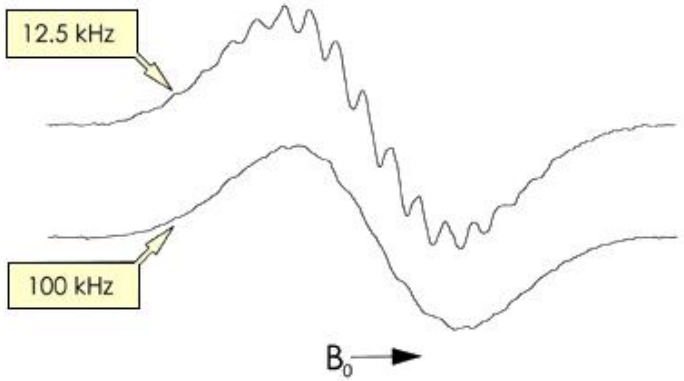

- modulation frequency effect –

$$\Delta x \cdot \Delta(m\upsilon) \geq \frac{\hbar}{2} \qquad \Delta E \cdot \Delta t \geq \frac{\hbar}{2} \qquad (\hbar = \frac{h}{2})$$

What is EPR ?

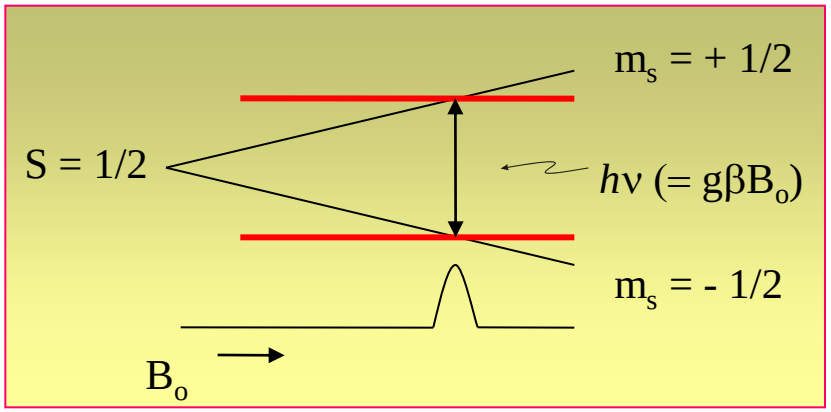

- ***h*** Planck's constant (6.626196 x 10^{-27} erg.sec)
- **ν** frequency (GHz or MHz)
- **g** g-factor (approximately 2.0)
- **β** Bohr magneton (9.2741 x 10^{-21} erg.Gauss^{-1})
- **B_o** magnetic field (Gauss or mT)

$$H = \beta \mathbf{S} \cdot \mathbf{g} \cdot \mathbf{H}$$

Selection Rule
$\Delta M_S = \pm 1$

Bruker EMX EPR spectrometer

"Electron Zeeman Interaction"

What is EPR ?

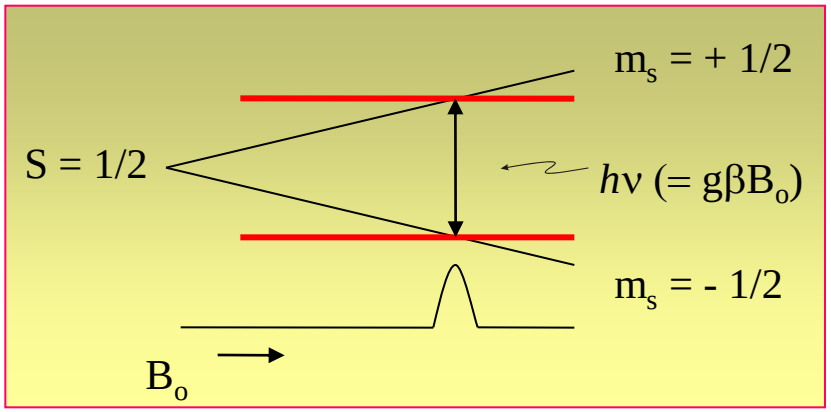

경북대학교

- ***h*** Planck's constant (6.626196 x 10^{-27} erg.sec)
- **ν** frequency (GHz or MHz)
- **g** g-factor (approximately 2.0)
- **β** Bohr magneton (9.2741 x 10^{-21} erg.Gauss^{-1})
- $\mathbf{B_o}$ magnetic field (Gauss or mT)

$$H = \beta \mathbf{S} \cdot \mathbf{g} \cdot \mathbf{H}$$

Selection Rule

$\Delta M_S = \pm 1$

"Electron Zeeman Interaction"

What is EPR ?

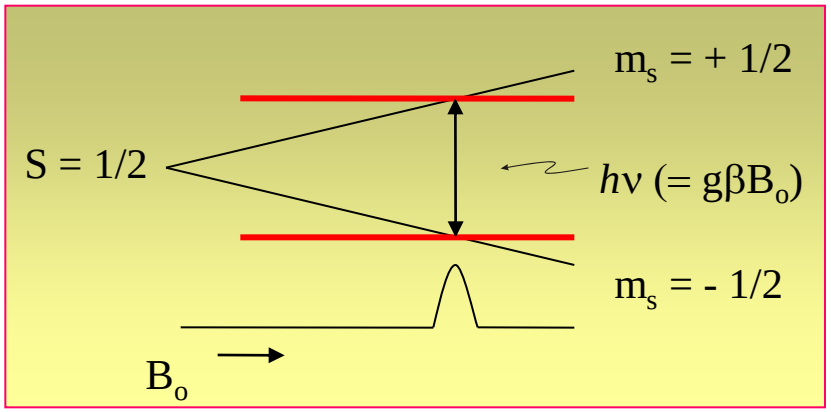

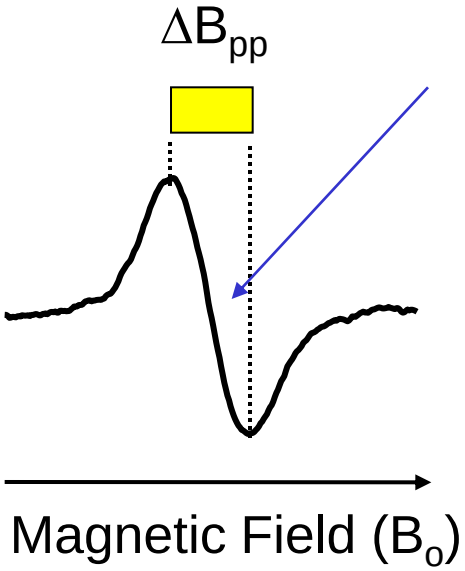

- ***h*** Planck's constant (6.626196 x 10^{-27} erg.sec)
- **ν** frequency (GHz or MHz)
- **g** g-factor (approximately 2.0)
- **β** Bohr magneton (9.2741 x 10^{-21} erg.Gauss^{-1})
- $\mathbf{B_o}$ magnetic field (Gauss or mT)

$$H = \beta \mathbf{S} \cdot \mathbf{g} \cdot \mathbf{H}$$

$$\mathbf{g} = h\nu / \beta \mathbf{B_o}$$

Selection Rule
$\Delta M_S = \pm 1$

"Electron Zeeman Interaction"

What is g ?

It is an inherent property of a system containing an unpaired spin.

Similar to the ***chemical shift*** observed in an NMR spectrum.

The g value for a single unpaired electron ***(free electron)*** has been calculated and experimentally determined. It is **2.0023192778 ± 0.0000000062 (= g_e)**. ***The g value for an S = 1/2 system is usually near g_e, but it is not exactly at g_e. Why not?***

This is due to ***spin orbit*** coupling which determines both the value of ***g and its anisotropy*** (how far the 3 g values are from g_{av}. ***The g value can often be calculated and the value is characteristic for a particular spin system.***

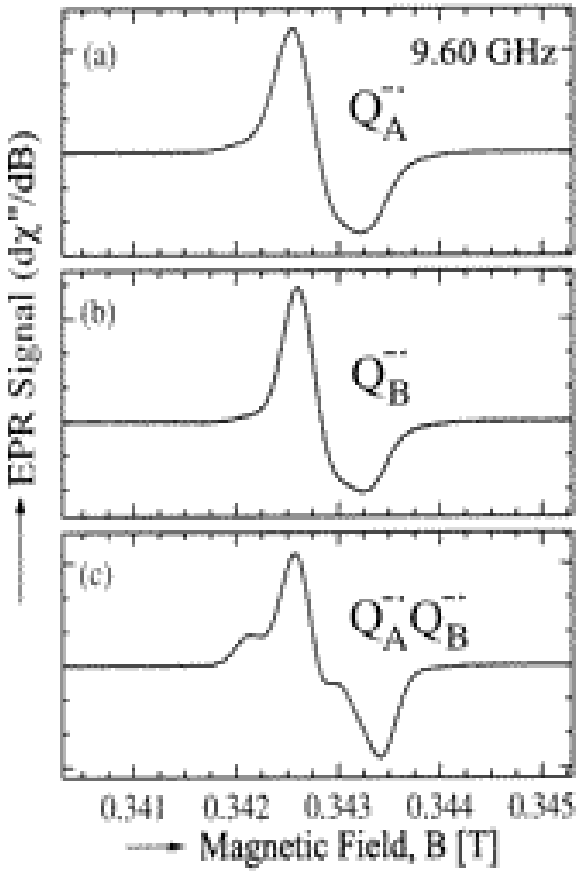

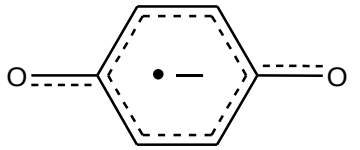

π-radical

What is g ?

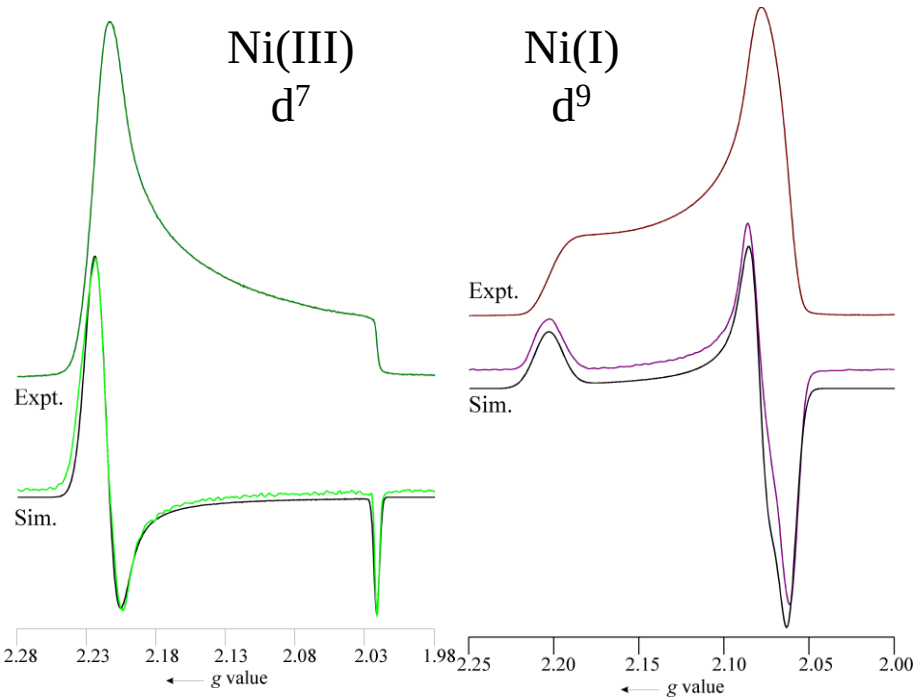

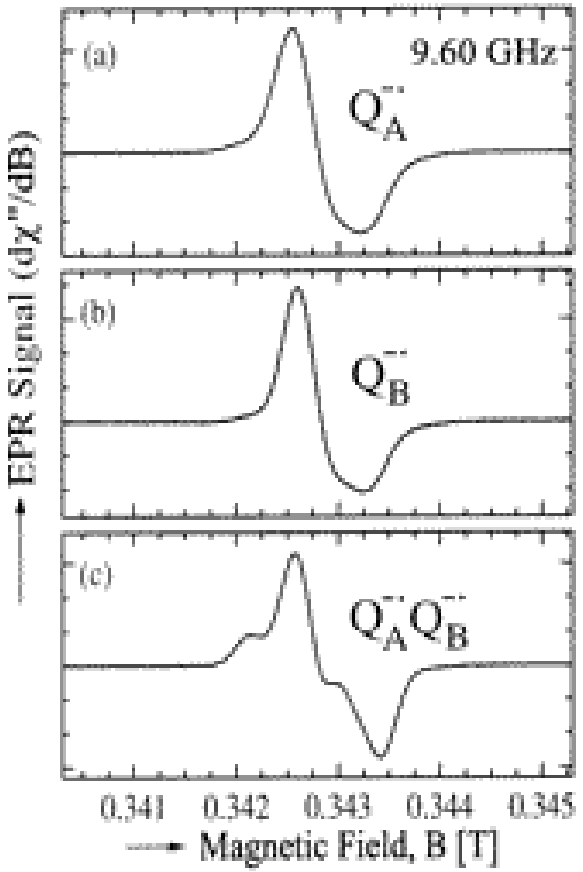

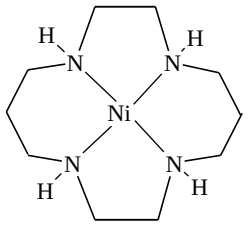

$[Ni(cyclam)]^{3+}$

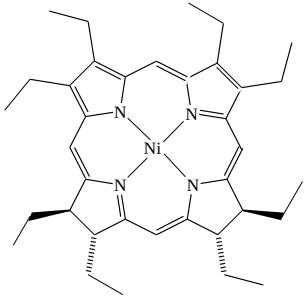

tct-Ni(OEiBC)$^-$

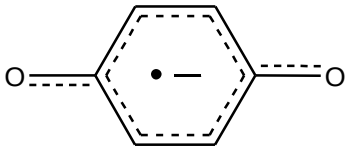

π-radical

What is g ?

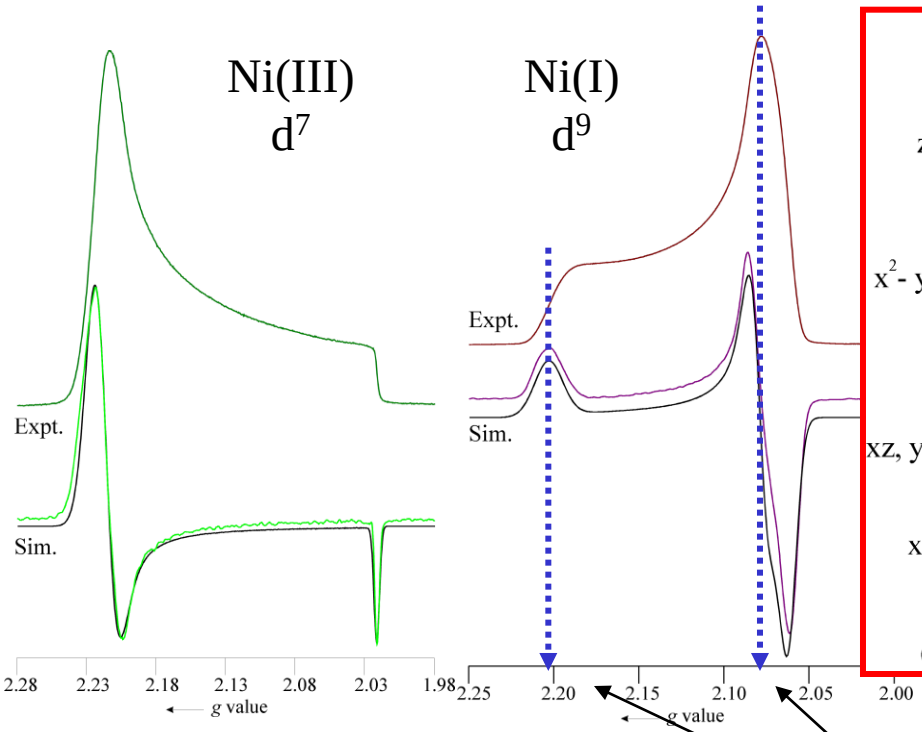

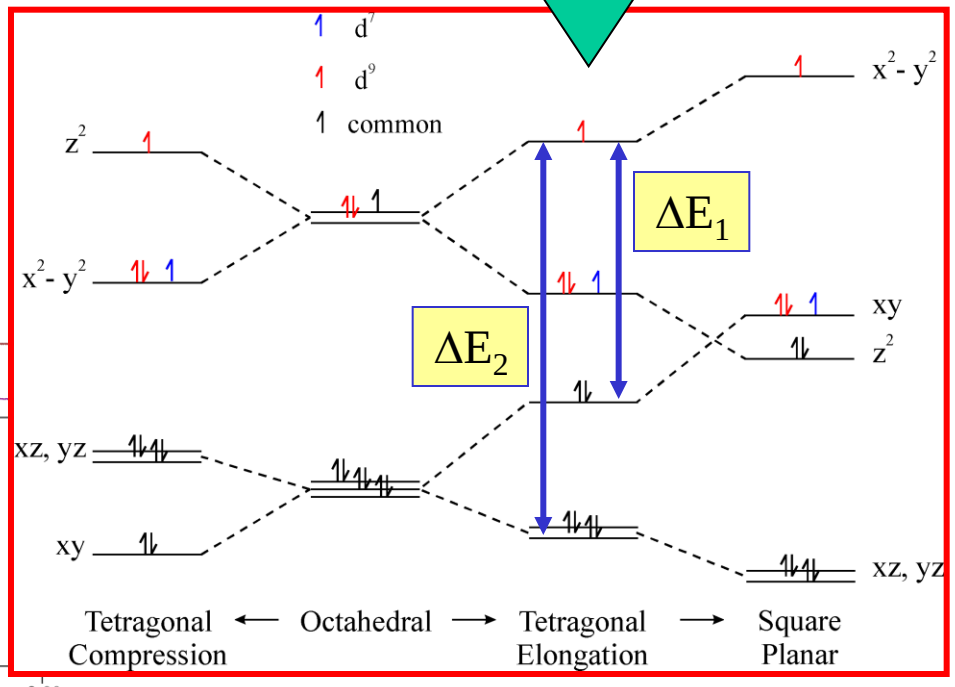

MO Scheme for Low-Spin $d^{7,9}$ Complexes

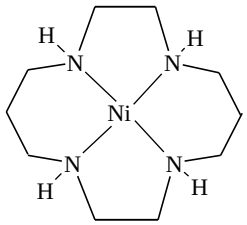

$[Ni(cyclam)]^{3+}$

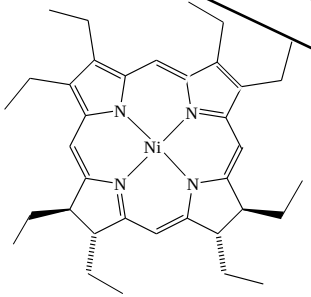

tct-Ni(OEiBC)$^-$

for d^9,

$g_z = g_e [1 + 8 \lambda / \Delta E_1] = g_\parallel$

$g_{x,y} = g_e [1 + 2\lambda / \Delta E_2] = g_\perp$

λ: spin-orbit coupling constant

What is g ?

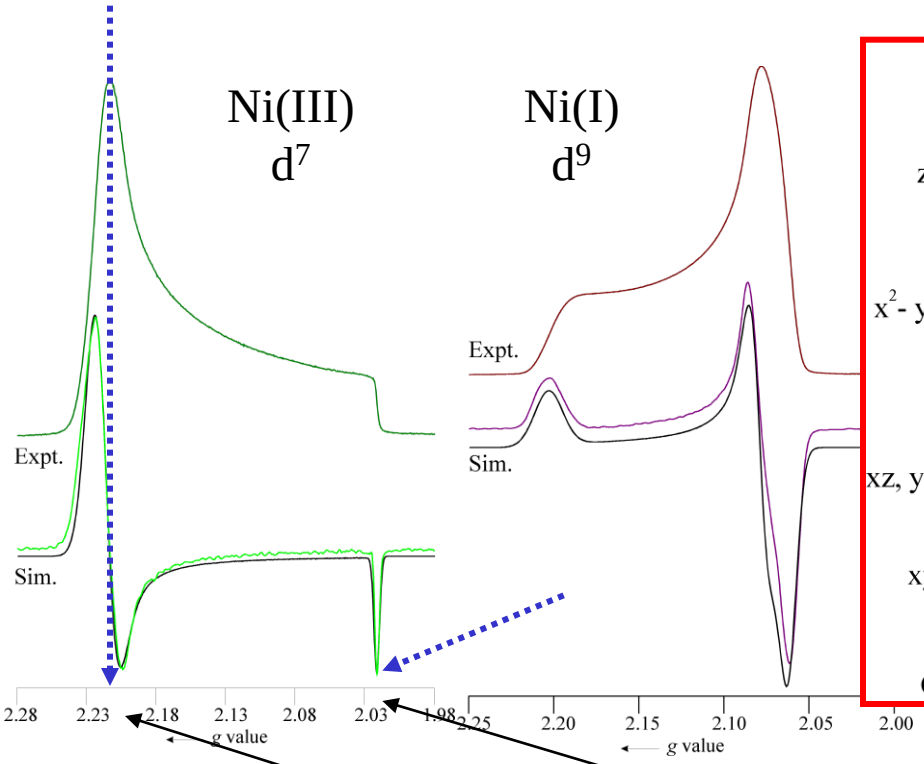

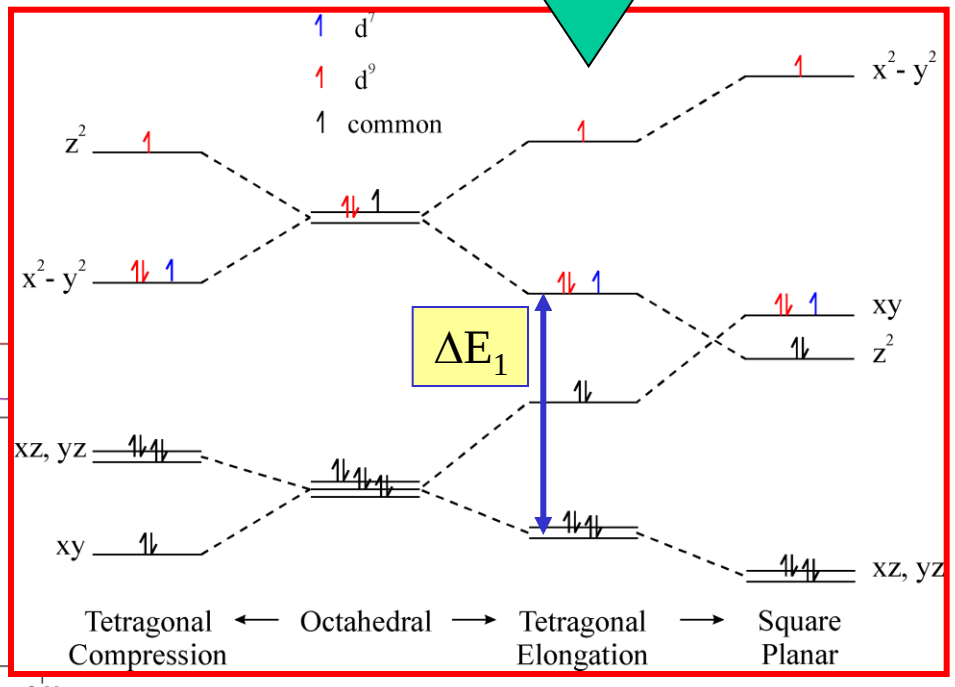

MO Scheme for Low-Spin $d^{7,9}$ Complexes

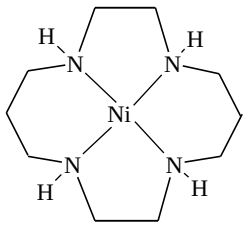

$[Ni(cyclam)]^{3+}$

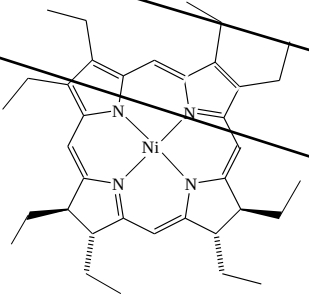

tct-Ni(OEiBC)$^-$

for d^7,

$g_z \sim g_e = g_\parallel$

$g_{x,y} = g_e [1 + 6\lambda / \Delta E_1] = g_\perp$

λ: spin-orbit coupling constant

What is g ?

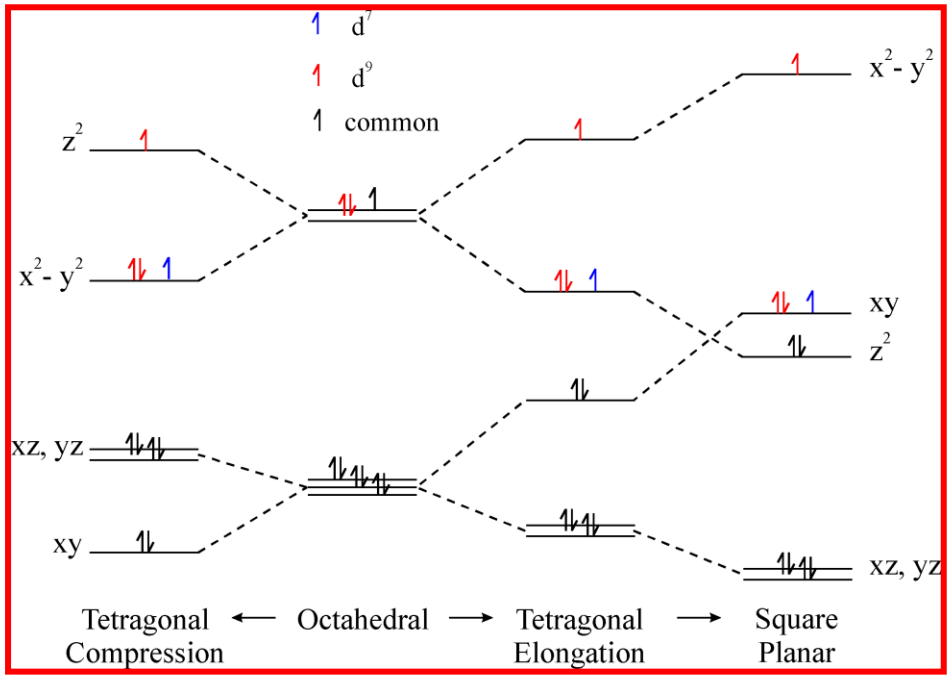

- Magic Pentagon –

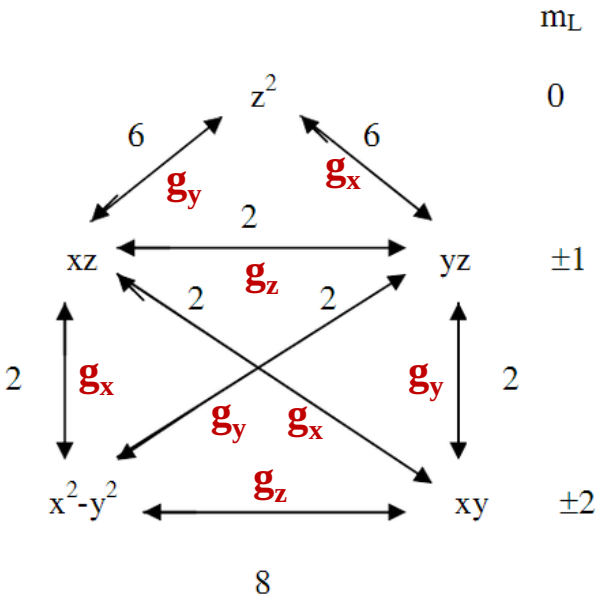

$$g = g_e[1 \pm \frac{n\lambda}{\text{E(ground state)} - \text{E(excited state)}}]$$

$$= g_e[1 + \frac{n\lambda}{\text{E(orbital of unpaired electron in ground state)} - \text{E(orbital of unpaired electron in excited state)}}]$$

for d^9,

$g_z = g_e\,[1 + 8\,\lambda / \Delta E_1] = g_{\parallel}$

$g_{x,y} = g_e\,[1 + 2\lambda / \Delta E_2] = g_{\perp}$

λ: spin-orbit coupling constant

for d^7,

$g_z \sim g_e = g_{\parallel}$

$g_{x,y} = g_e\,[1 + 6\lambda / \Delta E_1] = g_{\perp}$

λ: spin-orbit coupling constant

Powder Patterns of EPR Spectra

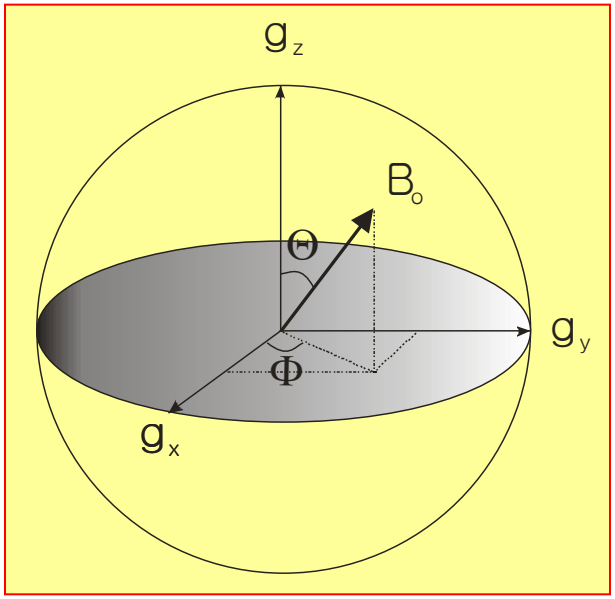

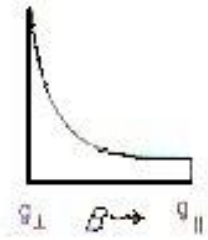

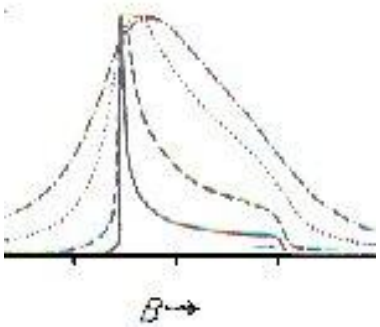

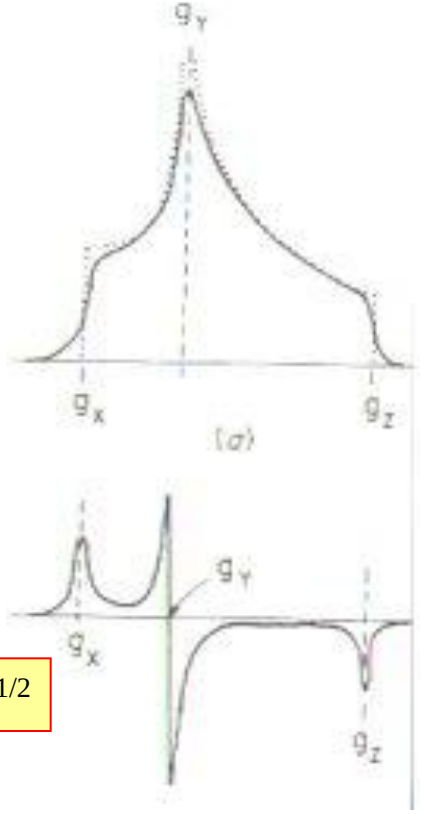

$$g_{eff} = (g_x^2\sin^2\theta\cos^2\phi + g_y^2\sin^2\theta\sin^2\phi + g_z^2\cos^2\theta)^{1/2}$$

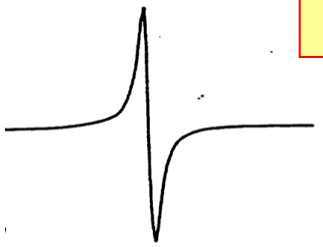

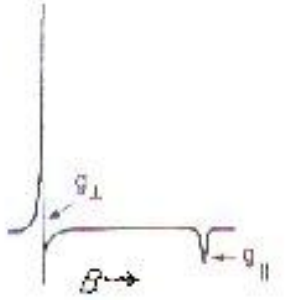

Isotropic ***g***: $g_x = g_y = g_z$

Axial ***g***: $g_x = g_y \neq g_z$

Rhombic ***g***: $g_x \neq g_y \neq g_z$

Powder*: randomly oriented samples such as frozen solutions, powders*

Even though we talk about ***g_x, g_y, and g_z,*** *the values should be more properly called* ***g_1, g_2, and g_3*** *unless we have evidence for the nature of the g tensor relative to the* ***molecular axes****.*

Powder Patterns of EPR Spectra

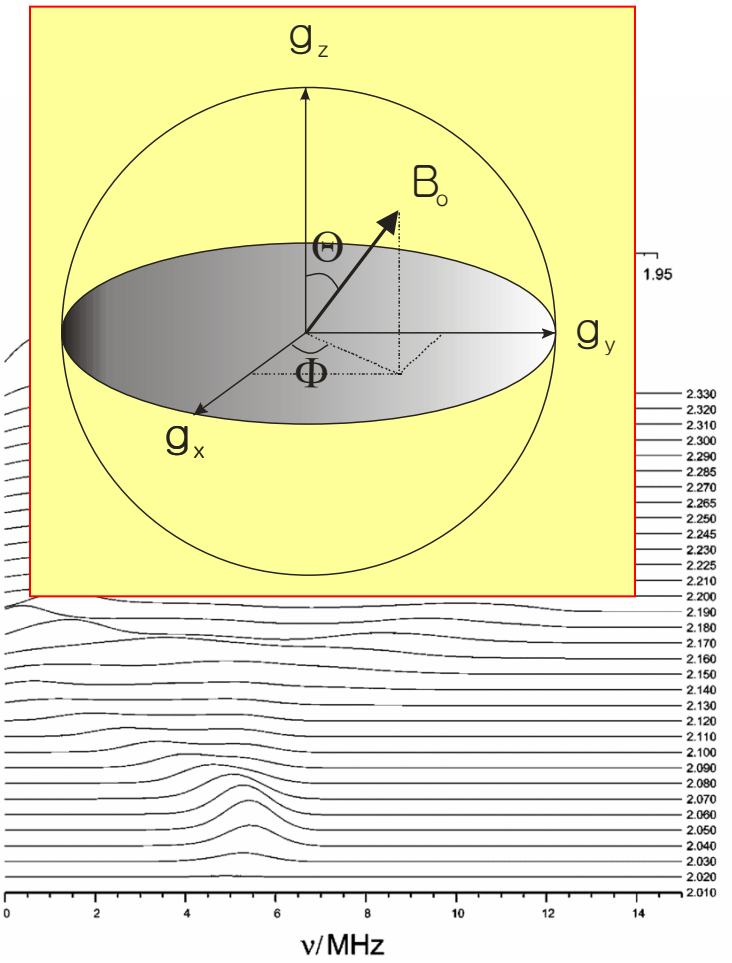

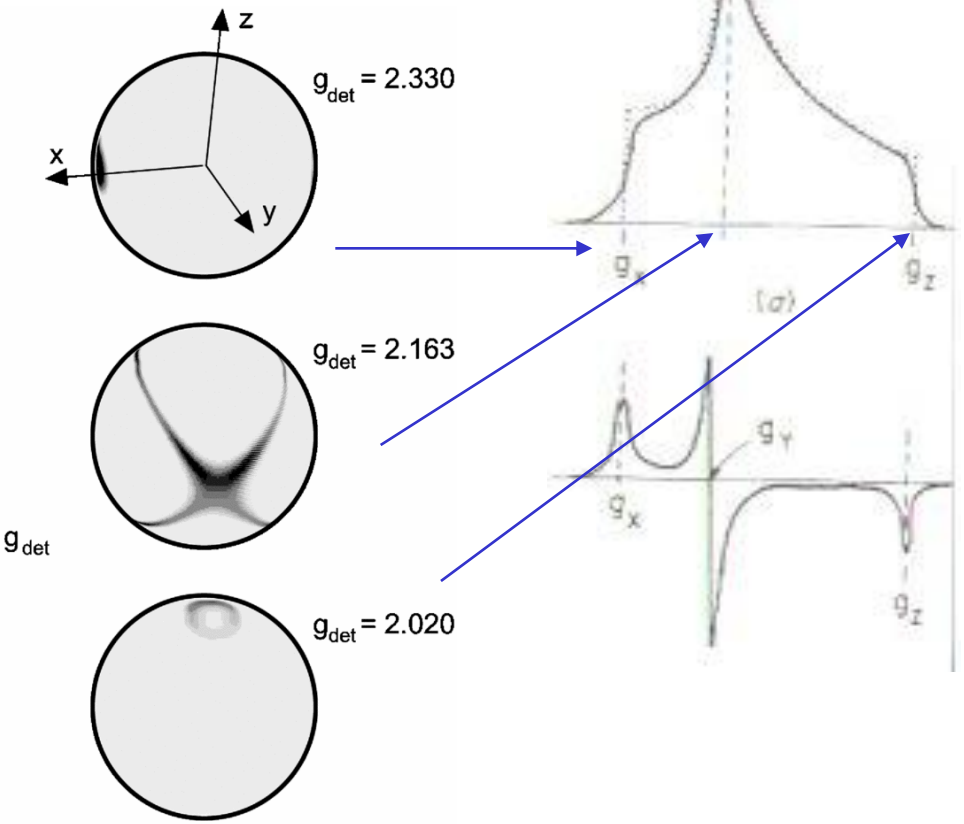

$$g_{eff} = (g_x^2 \sin^2\theta\cos^2\phi + g_y^2 \sin^2\theta\sin^2\phi + g_z^2\cos^2\theta)^{1/2}$$

Powder Patterns of EPR Spectra

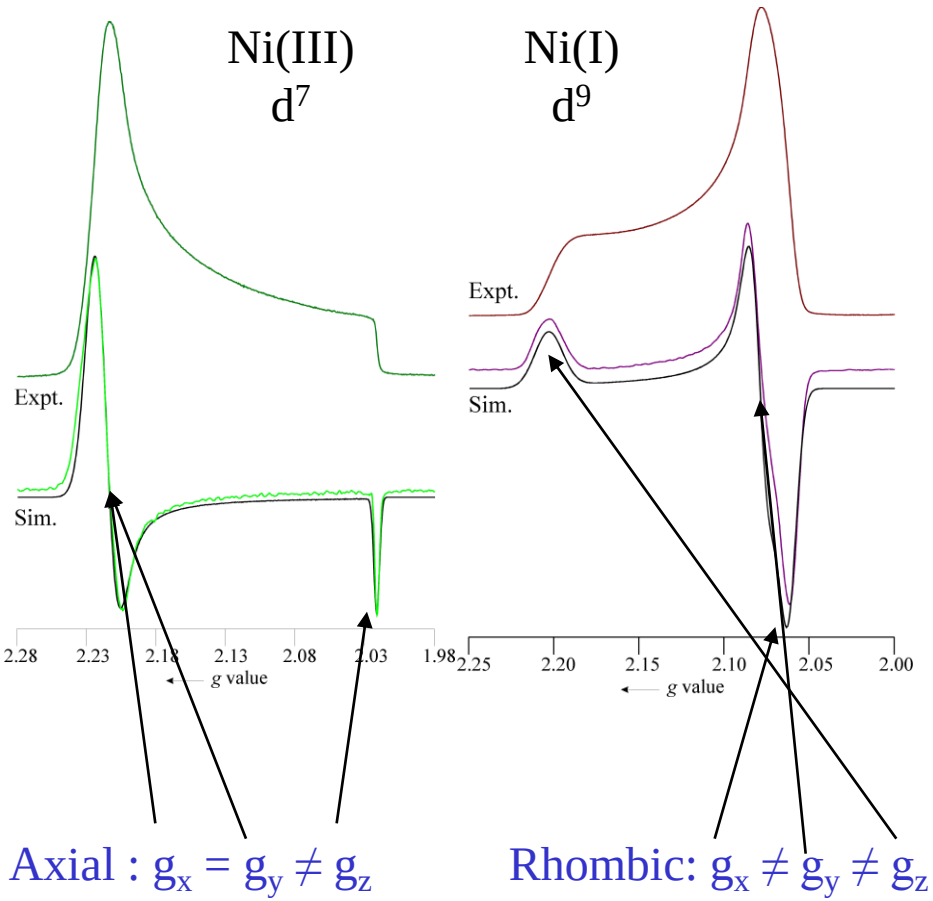

Axial : $g_x = g_y \neq g_z$

Rhombic: $g_x \neq g_y \neq g_z$

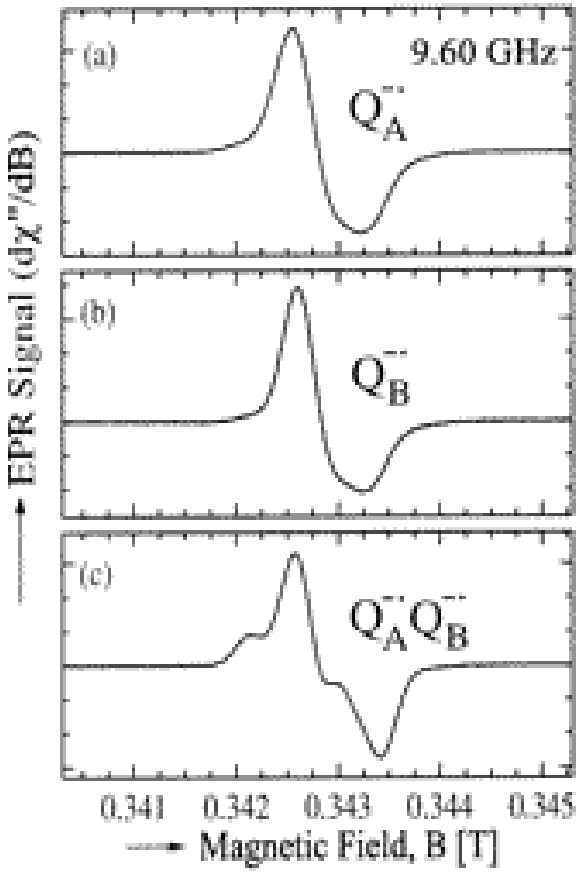

Near isotropic

EPR of Ni(I) and Ni(III)

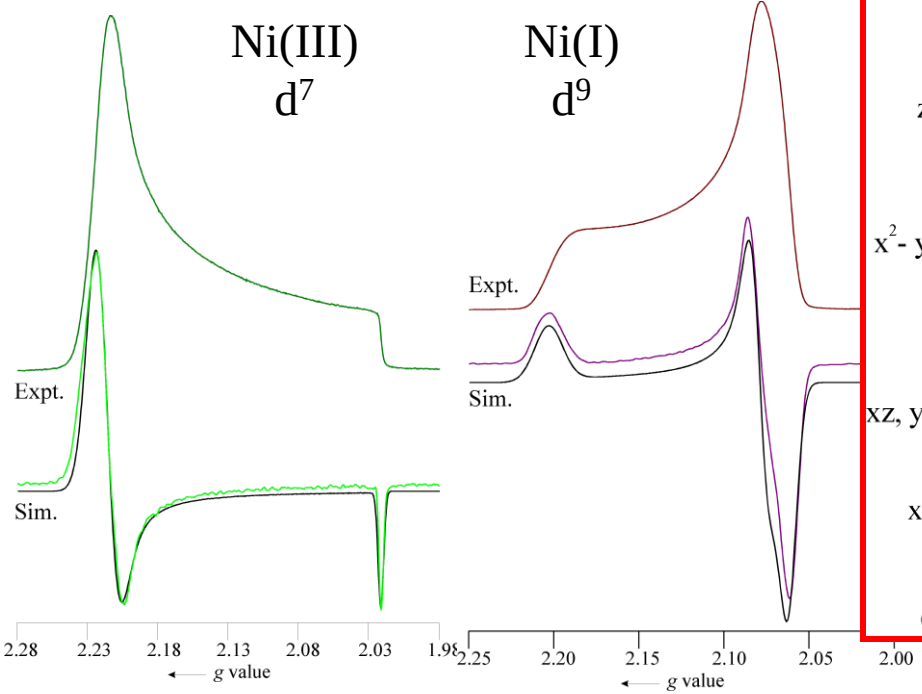

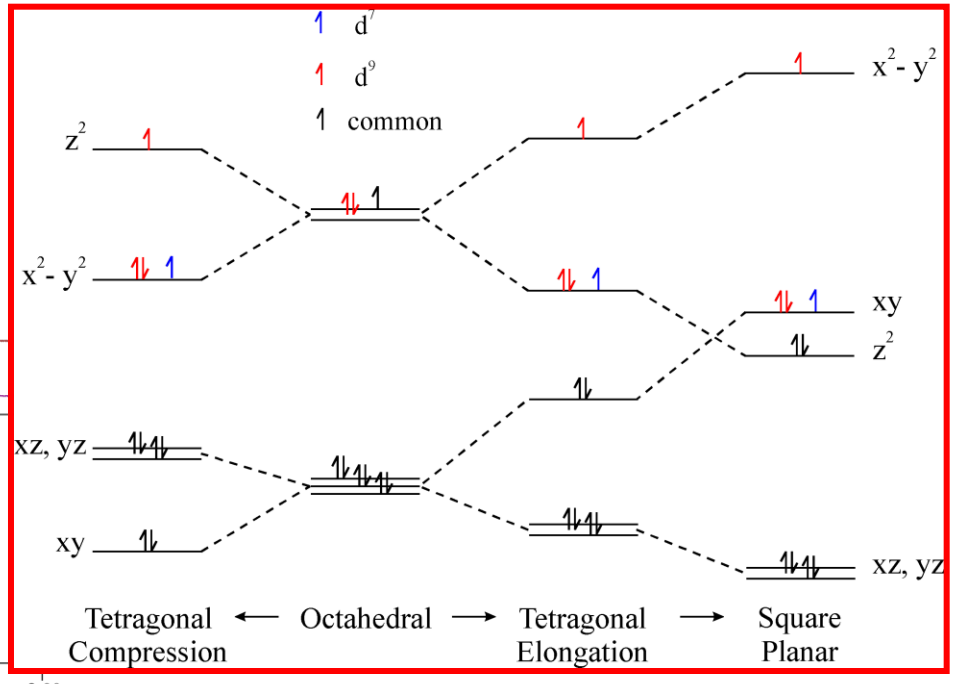

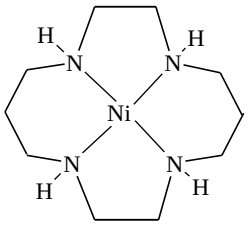

[Ni(cyclam)]$^{3+}$

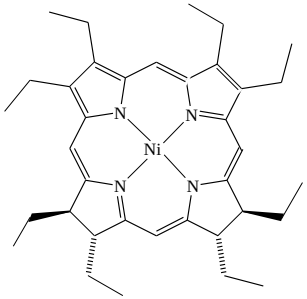

tct-Ni(OEiBC)$^{-}$

EPR of Cu(II) (S=1/2, d^9)

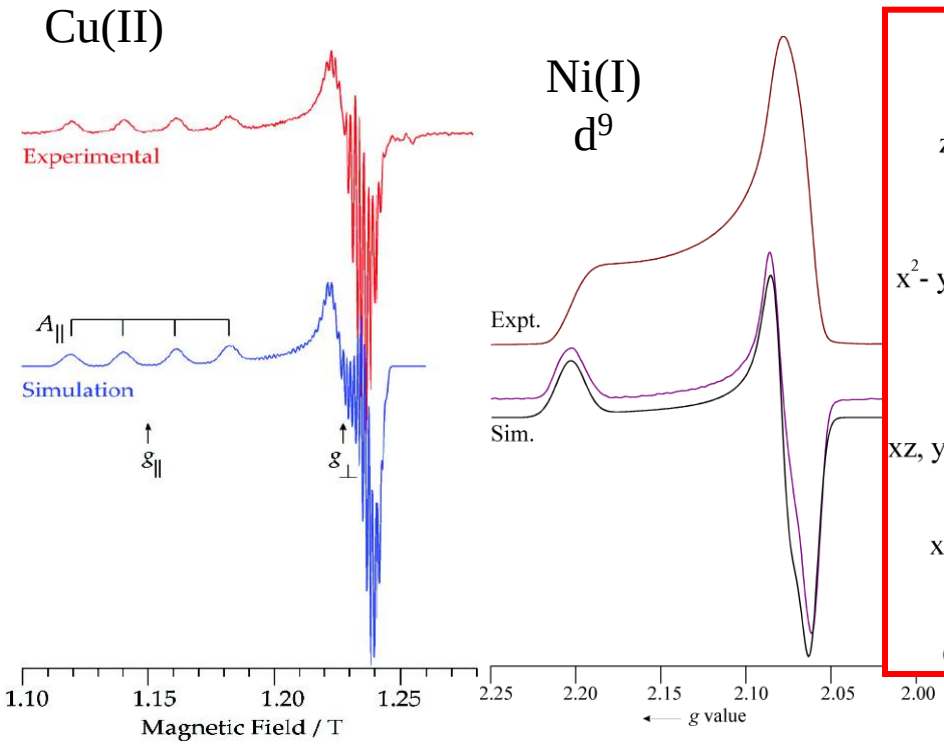

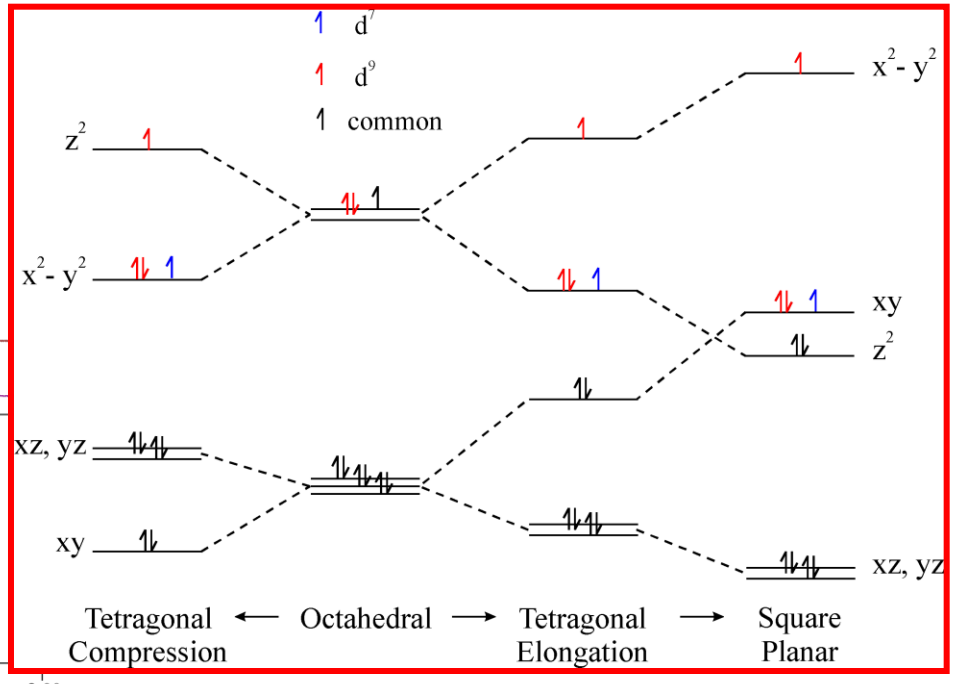

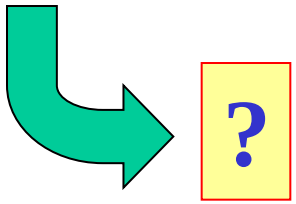

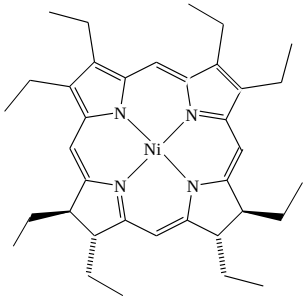

tct-Ni(OEiBC)$^-$

J. Braz. Chem. Soc. 17, 1501 (2006)

Solution EPR

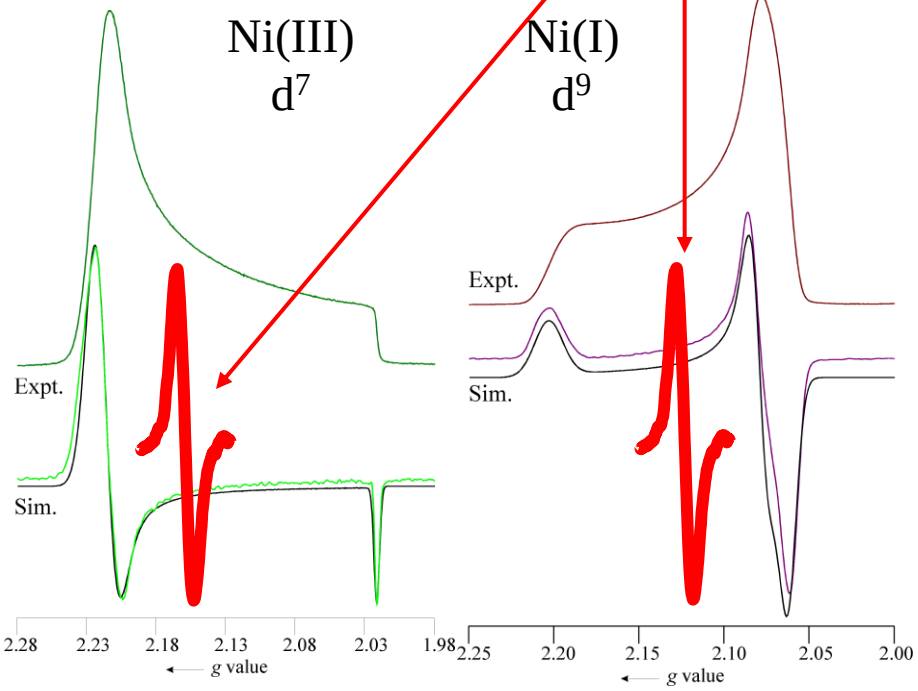

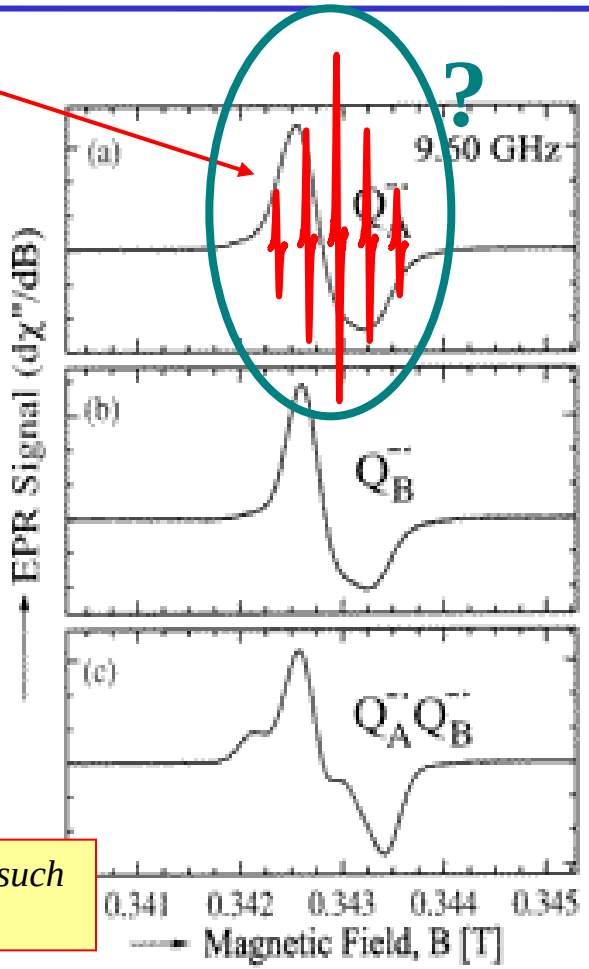

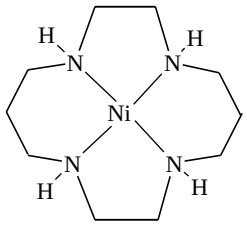

$[Ni(cyclam)]^{3+}$

***Powder**: randomly oriented samples such as frozen solutions, powders*

In solution**: when molecules are rapidly tumbling (within microwave time scale), **g-anisotropy is averaged out.

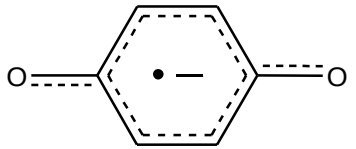

π-radical

tct-Ni(OEiBC)$^-$

Electron spin – Nuclear spin Interaction

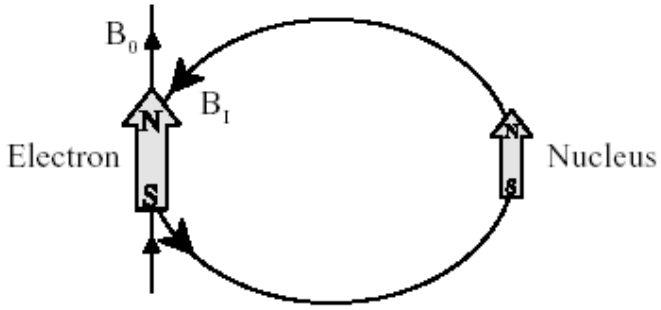

$$B_{eff} = B_0 - B_{Ind}$$

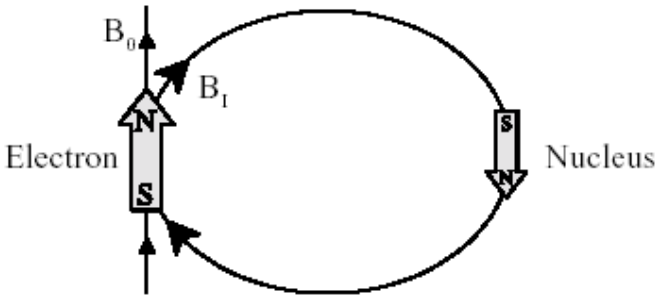

$$B_{eff} = B_0 + B_{Ind}$$

Isotope	Nuclear Spin (I)	% Abundance
^{1}H	1/2	99.9
^{2}H	1	0.02
^{12}C	0	98.9
^{13}C	1/2	1.1
^{14}N	1	99.6
^{15}N	1/2	0.37
^{16}O	0	99.8
^{17}O	5/2	0.037
^{32}S	0	95.0
^{33}S	3/2	0.76
^{51}V	7/2	99.8
^{55}Mn	5/2	100
^{56}Fe	0	91.7
^{57}Fe	1/2	2.19
^{59}Co	7/2	100
^{58}Ni & ^{60}Ni	0	68 & 26
^{61}Ni	3/2	1.19
^{63}Cu & ^{65}Cu	3/2	69 & 31
^{95}Mo & ^{97}Mo	5/2	16 & 9
^{183}W	1/2	14.4

"Hyperfine Interaction"

Electron spin – Nuclear spin Interaction

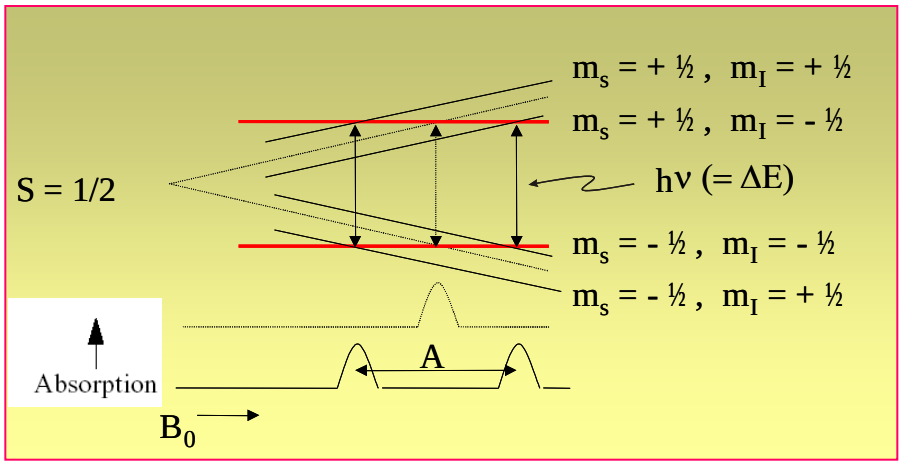

S=½;
I=½
Doublet

hfc (=A)

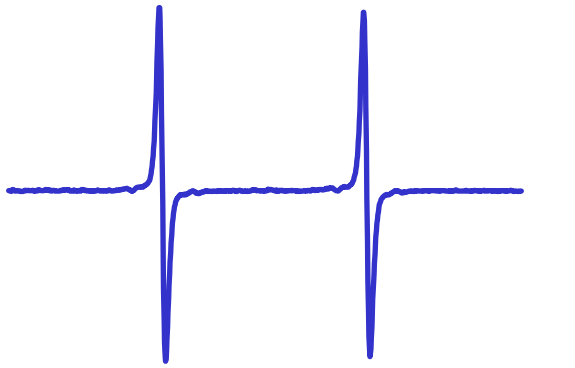

Magnetic Field →

hfc: hyperfine coupling constant

$$H = \beta \mathbf{S}\cdot\mathbf{g}\cdot\mathbf{H} + \mathbf{S}\cdot\mathbf{A}\cdot\mathbf{I}$$

Selection Rule
$\Delta M_S = \pm 1$; $\Delta M_I = 0$

"Hyperfine Interaction"

Electron spin – Nuclear spin Interaction

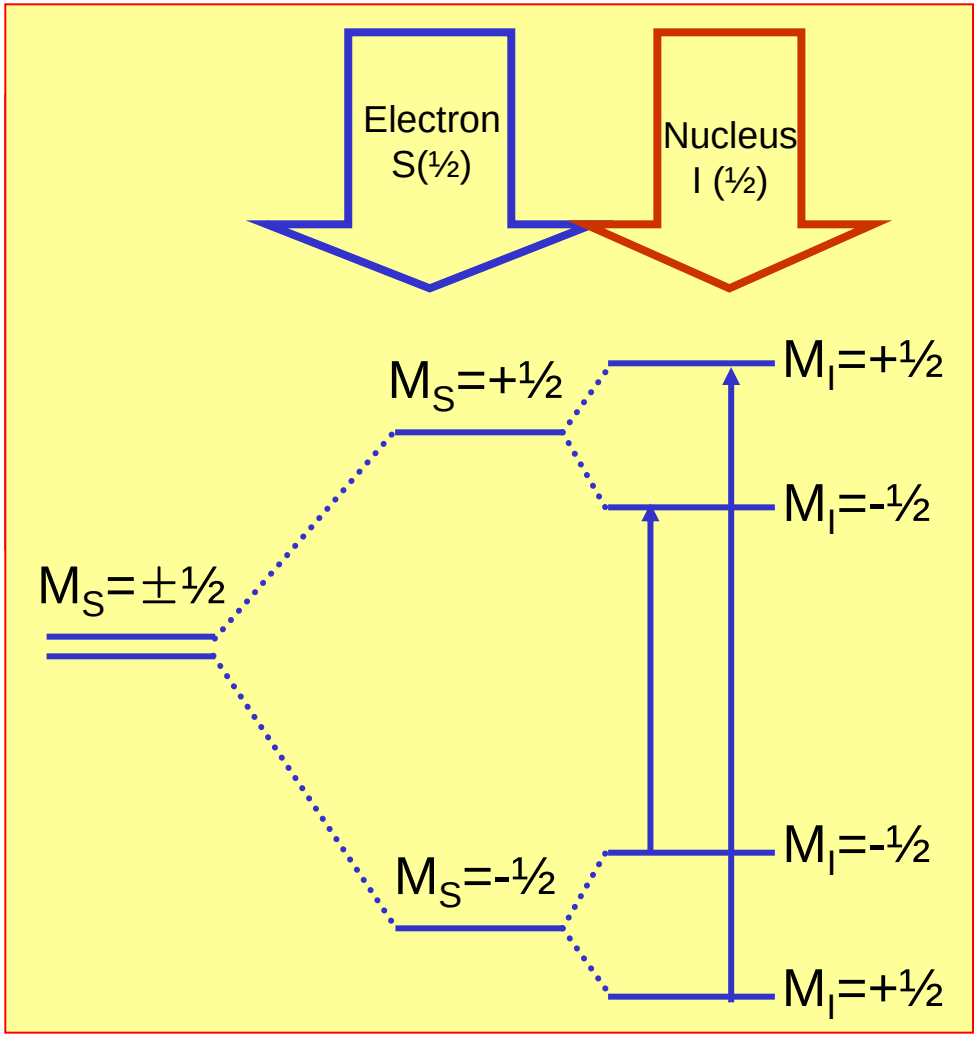

Selection Rule

$\Delta M_S = \pm 1; \Delta M_I = 0$

S=½;
I=½
Doublet

hfc (=A)

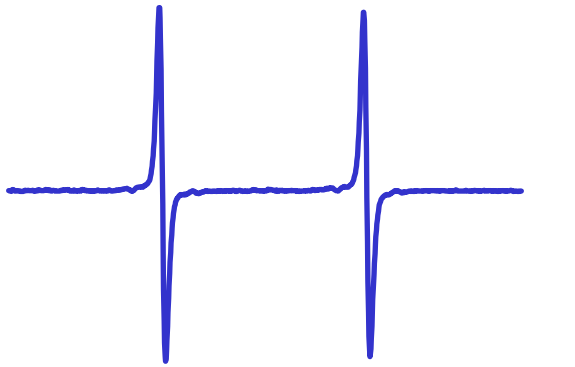

Magnetic Field →

hfc: hyperfine coupling constant

"Hyperfine Interaction"

Electron spin – Nuclear spin Interaction

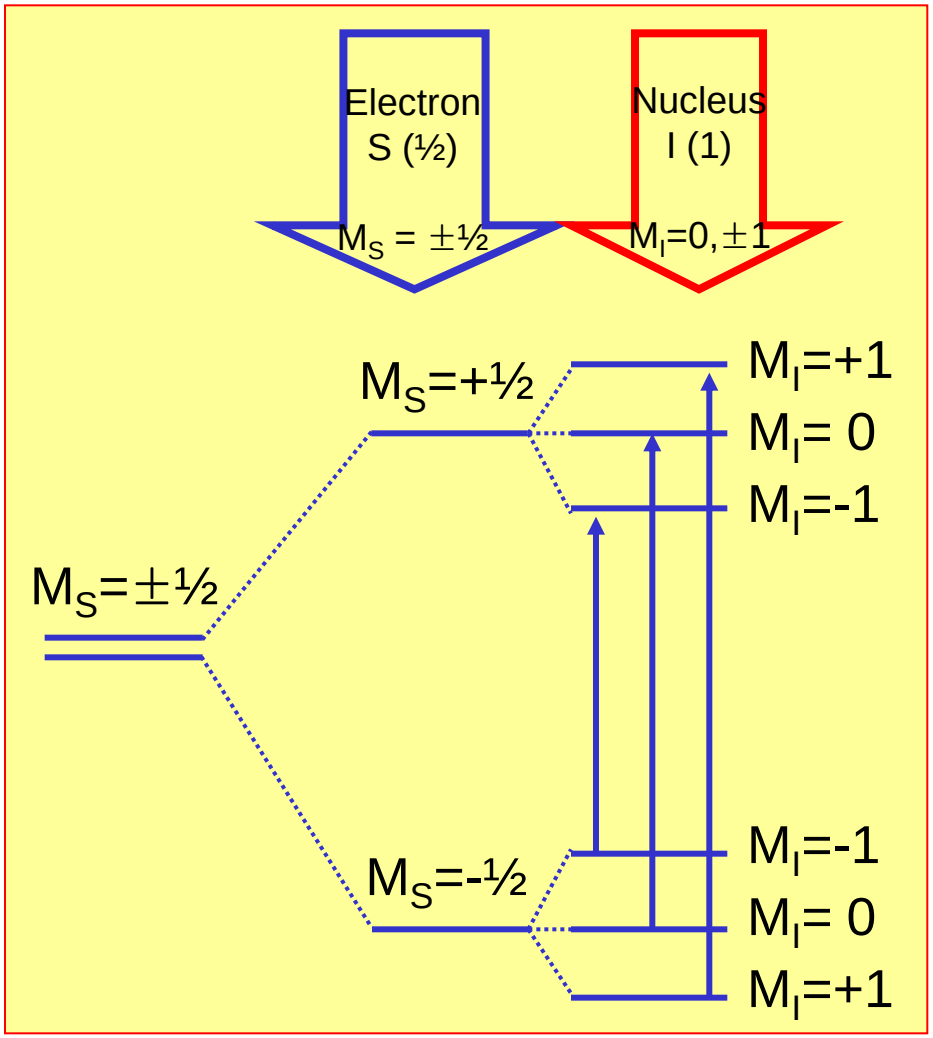

Selection Rule

$\Delta M_S = \pm 1; \Delta M_I = 0$

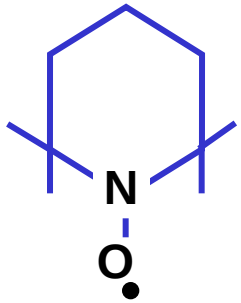

S=½;
I=1
Triplet

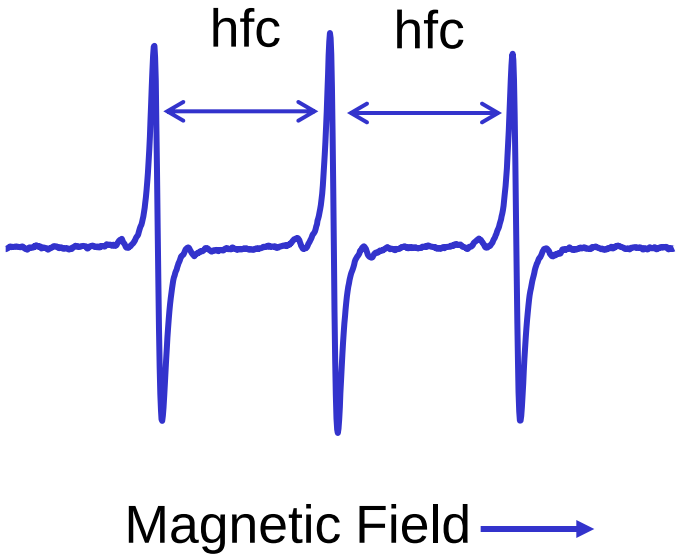

"Hyperfine Interaction"

Electron spin – Nuclear spin Interaction

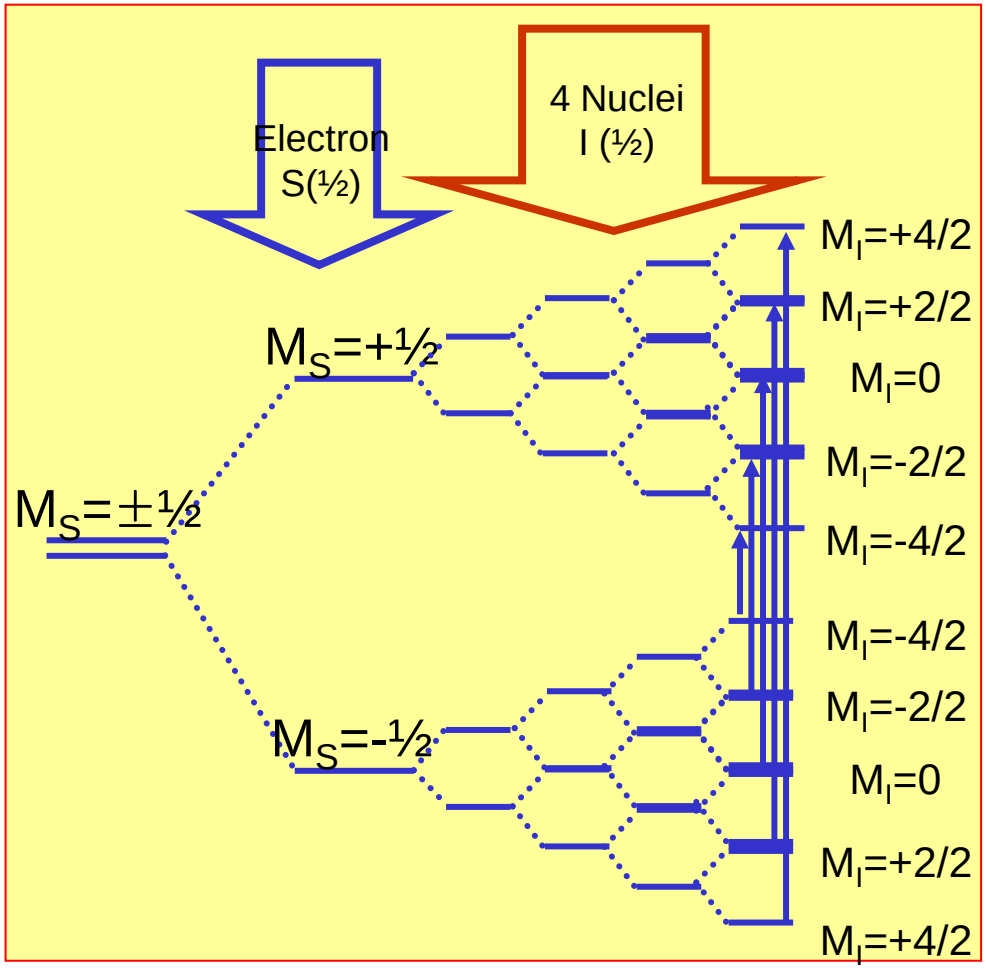

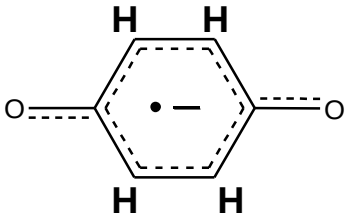

S=½;
I=1/2 x 4
Quintet

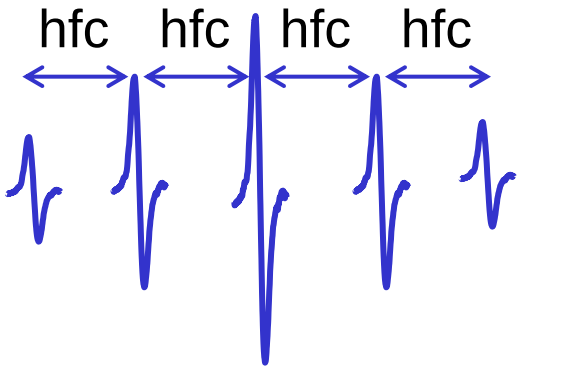

1 4 6 4 1

Pascal's triangle

So far, we have considered the cases of hyperfine interactions in solutions or in the samples with very narrow g-anisotropy. How about powder samples?

Electron spin – Nuclear spin Interaction

For ^{61}Ni, I = 3/2, so you expect (and see) 4 lines.

But the hyperfine splitting is unresolved in the $g_{\perp}$ direction.

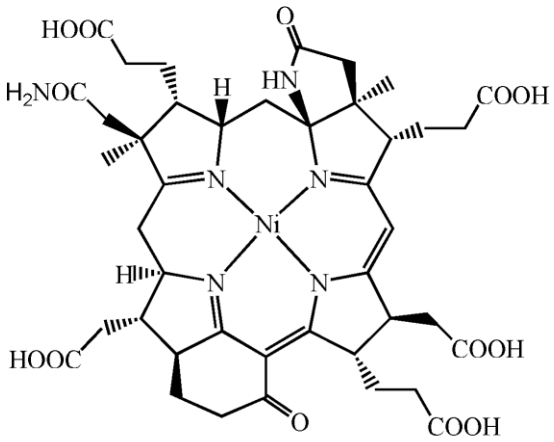

F_{430}

Ni(I)
d^9

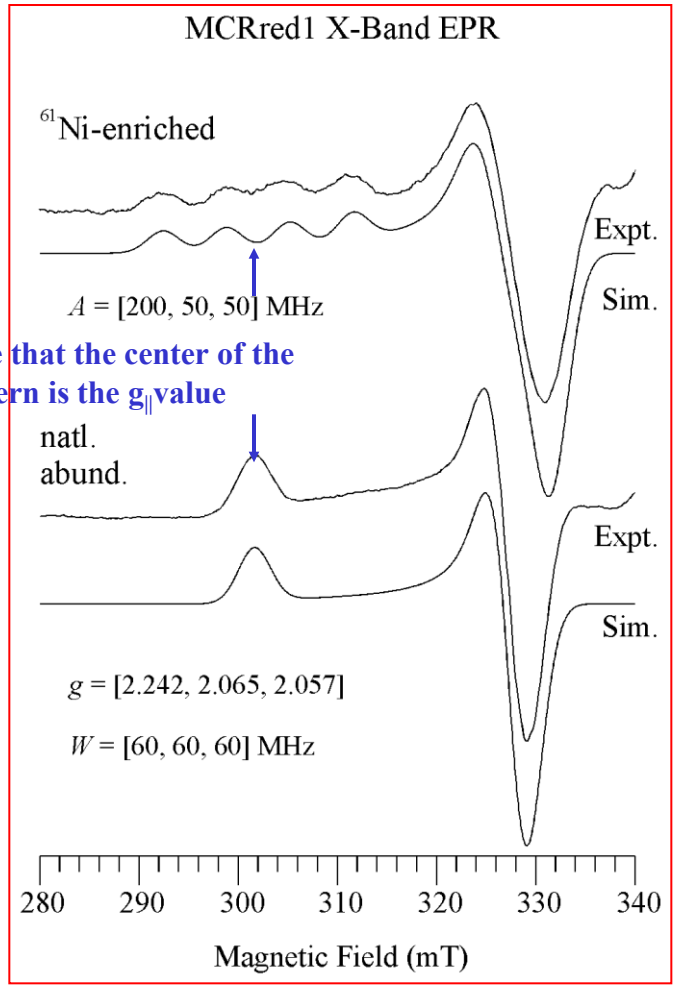

So far, we have considered the cases of hyperfine interactions in solutions or in the samples with very narrow g-anisotropy. How about powder samples?

Electron spin – Nuclear spin Interaction

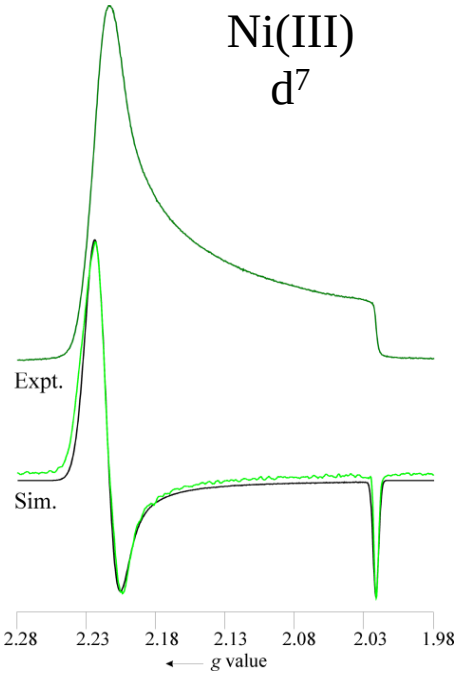

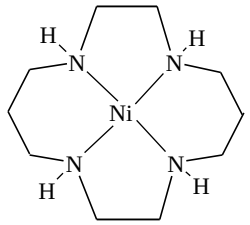

$[Ni(cyclam)]^{3+}$

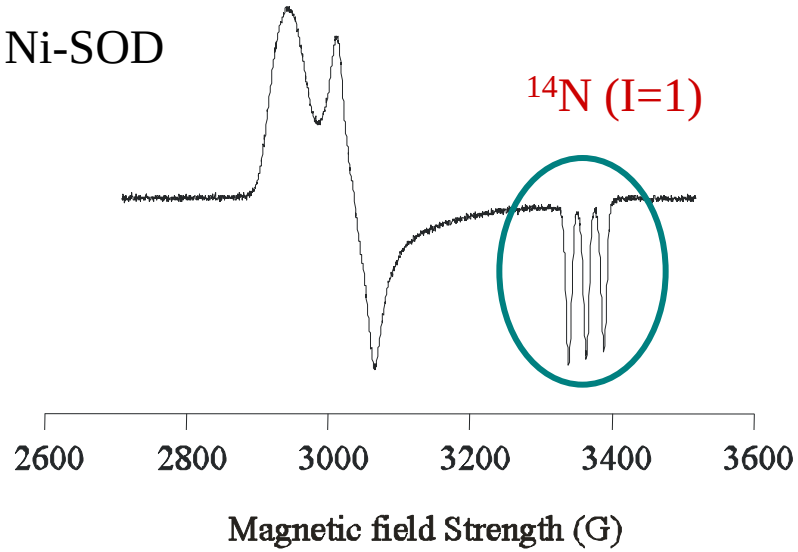

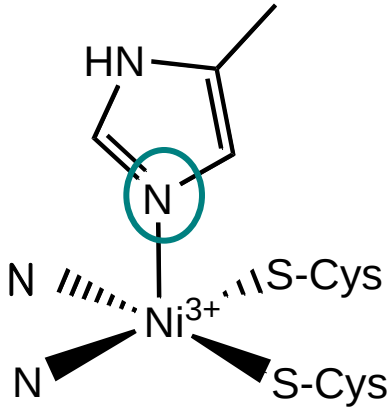

EPR of Cu(II) (S=1/2, d^9)

^{63}Cu (69 %), I = 3/2
^{65}Cu (31 %), I = 3/2

Superhyperfine Splitting

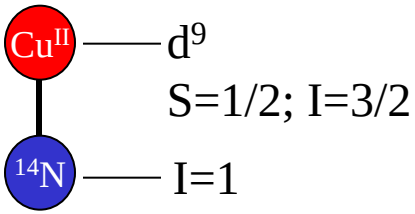

d^9
S=1/2; I=3/2
I=1

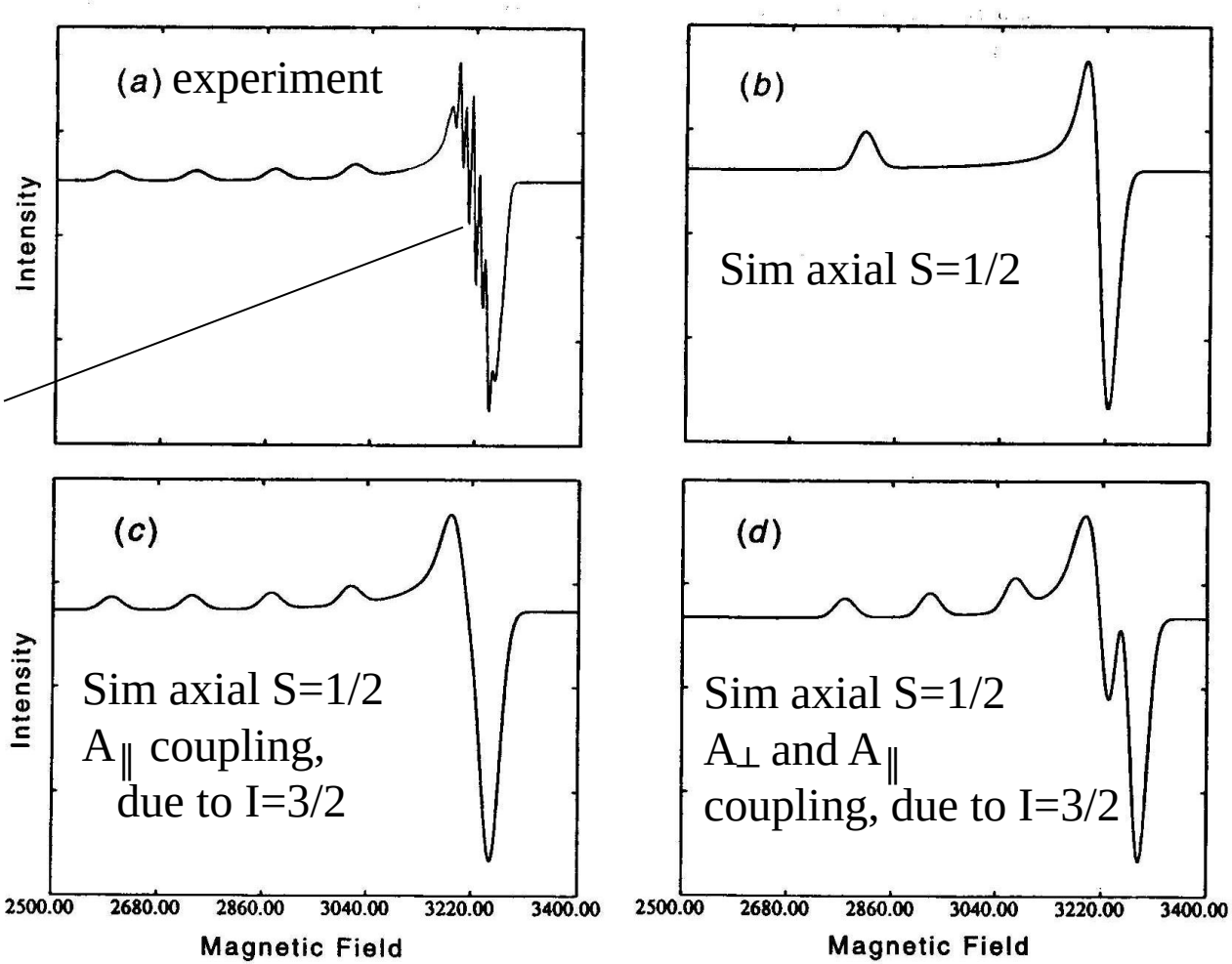

"Hyperfine Interaction"

EPR of Co(II) (S = 1/2, d^7)

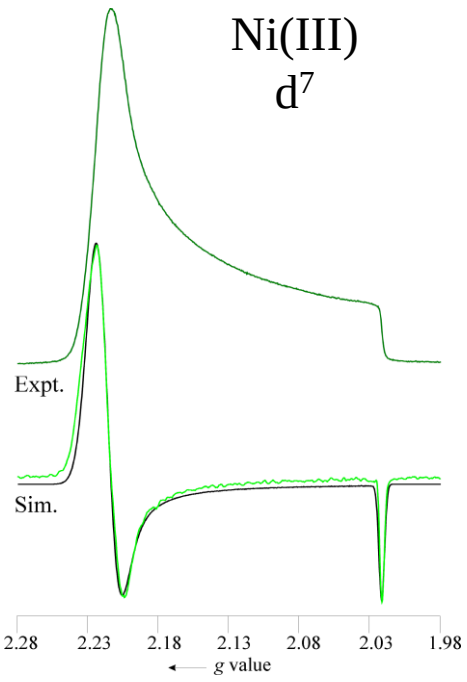

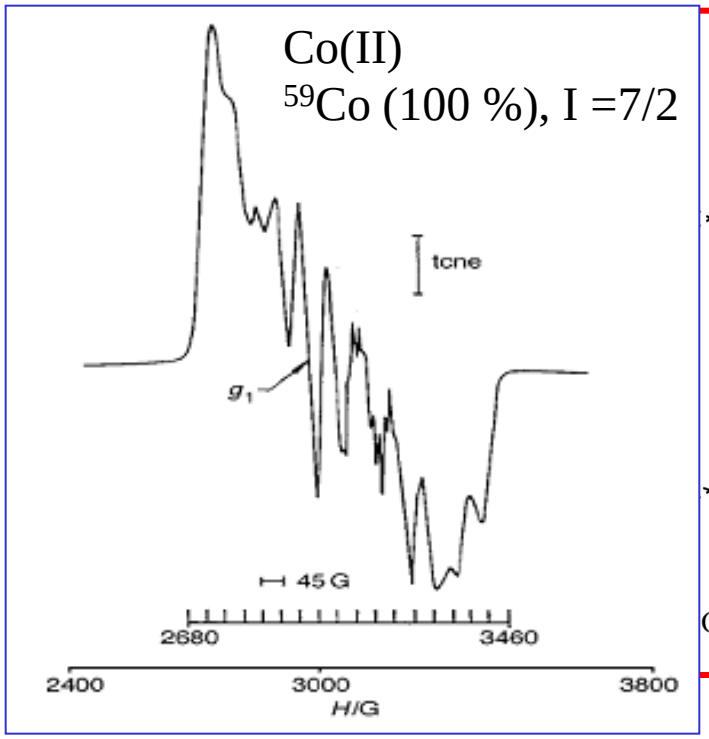

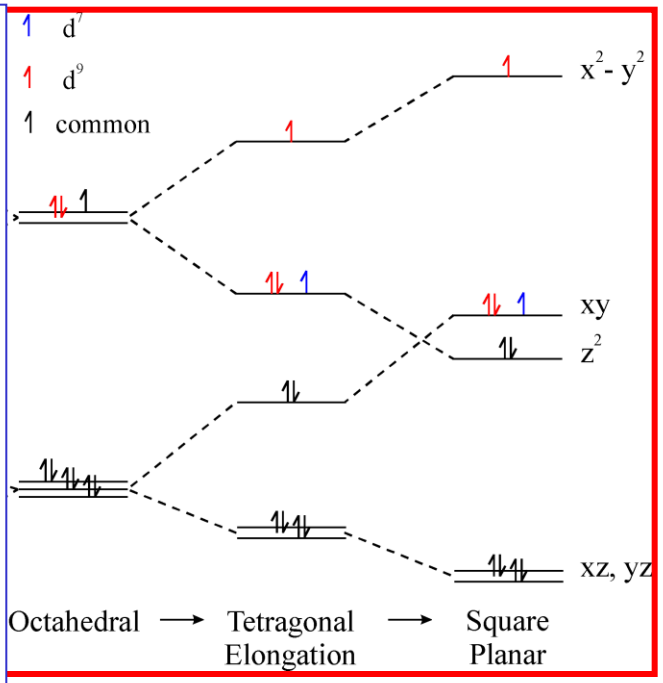

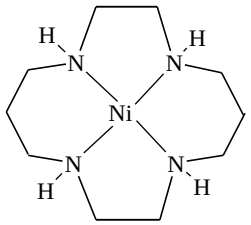

[Ni(cyclam)]$^{3+}$

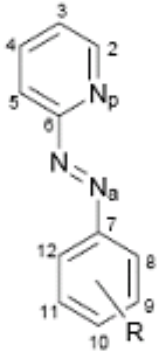

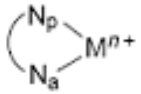

ML

FRBS Lett.. 409, 421 (1997)

EPR of Co(II) (S = 1/2, d^7)

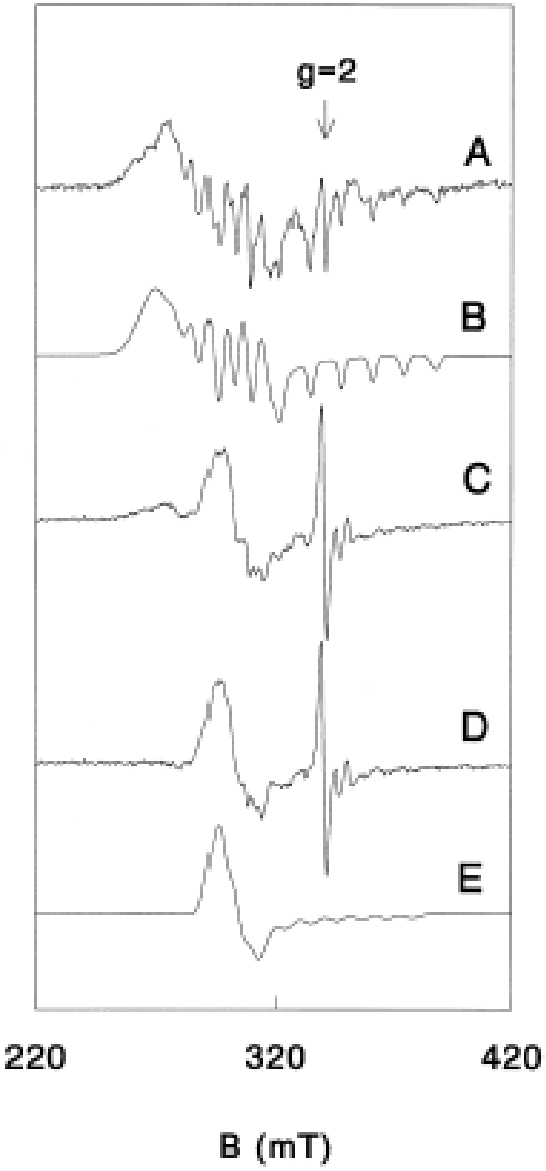

Redox chemistry of cobalamin and iron-sulfur cofactors in the tetrachloroethene reductase of *Dehalobacter restrictus*

A : spectrum of 4mg/ml enzyme in 25mM Tris-HCl buffer pH 8.0 poised at a redox potetial of -27mV.

B : simulation of A

C : spectrum of enzyme in 125mM ches buffer, pH 9.6, poised at redox potential of -293mV.

D : C-A spectrum

E : simulation of D

FRBS Lett.. 409, 421 (1997)

EPR of Co(II) (S = 3/2, d^7)

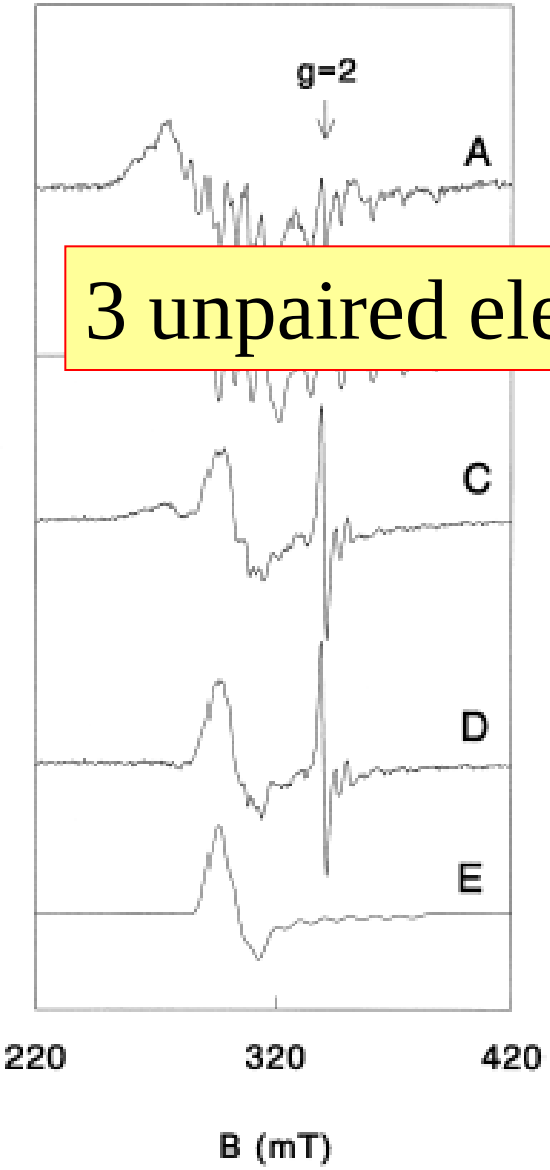

3 unpaired electrons ?

Redox che
tet

A : spectrum of
se

B : simulation o

C : spectrum of
redox potential

D : C-A spectrum

E : simulation of D

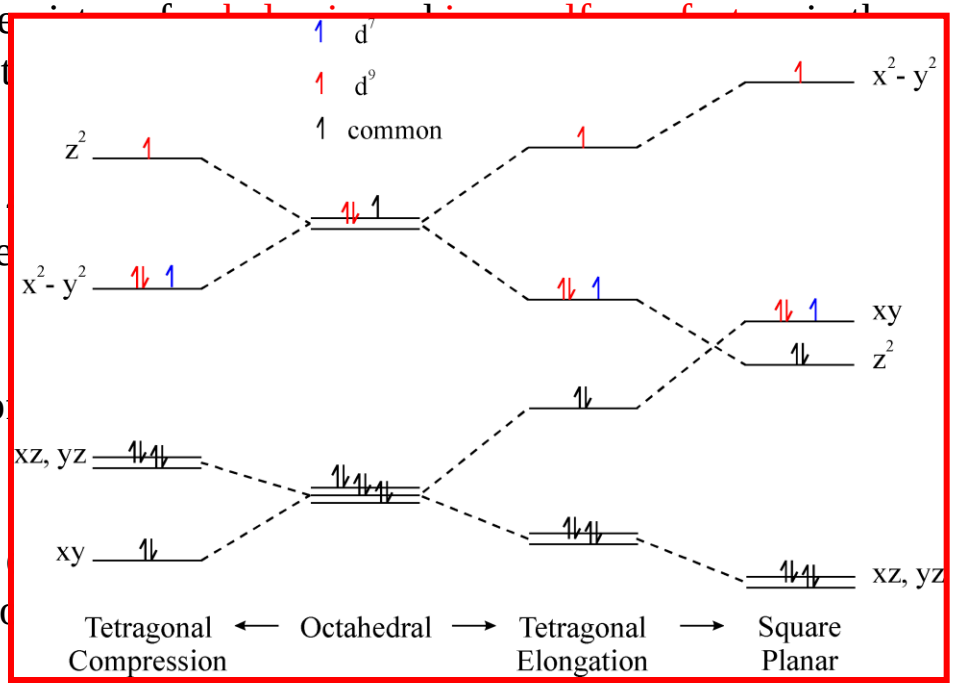

FRBS Lett.. 409, 421 (1997)

Electron spin – Electron spin Interaction

*When there is **more than one unpaired electron (S>1/2)**, the interaction between the spins must be considered. This term can be very large. The Hamiltonian for a system with a spin > 1/2 is:* $\mathbf{H = D [S_z^2 - 1/3\ S(S+1)\ + E/D\ (S_x^2 - S_y^2)] + g_o \beta S\ H}$

*The new terms are D and E/D. D is called the **zero-field splitting (ZFS) parameter**; E/D is the **rhombicity** (the ratio between D, the axial splitting parameter, and E, the rhombic splitting parameter, at zero field). The minimum value of E/D is 0 for an axial system. The maximum value is 1/2 for a rhombic system. The strength of the ZFS is determined by the nature of the ligands.*

So for a completely axial system (E/D = 0), $H = D [S_z^2 - 1/3\ S(S+1)] + g_o \beta S\ H$

Consider a case where S = 3/2, i.e., 4 unpaired electrons. These spins can interact to give a total spin moment, referred to as a system spin. There will be four sublevels for m_s*, where* S_z *= -3/2, -1/2, 1/2, and 3/2.*

*The energy for the + or -3/2 level will be: D[9/4-1/3(3/2*5/2)]= D[9/4-5/4]= D*
The energy for the + or - 1/2 level will be: -D.

Electron spin – Electron spin Interaction

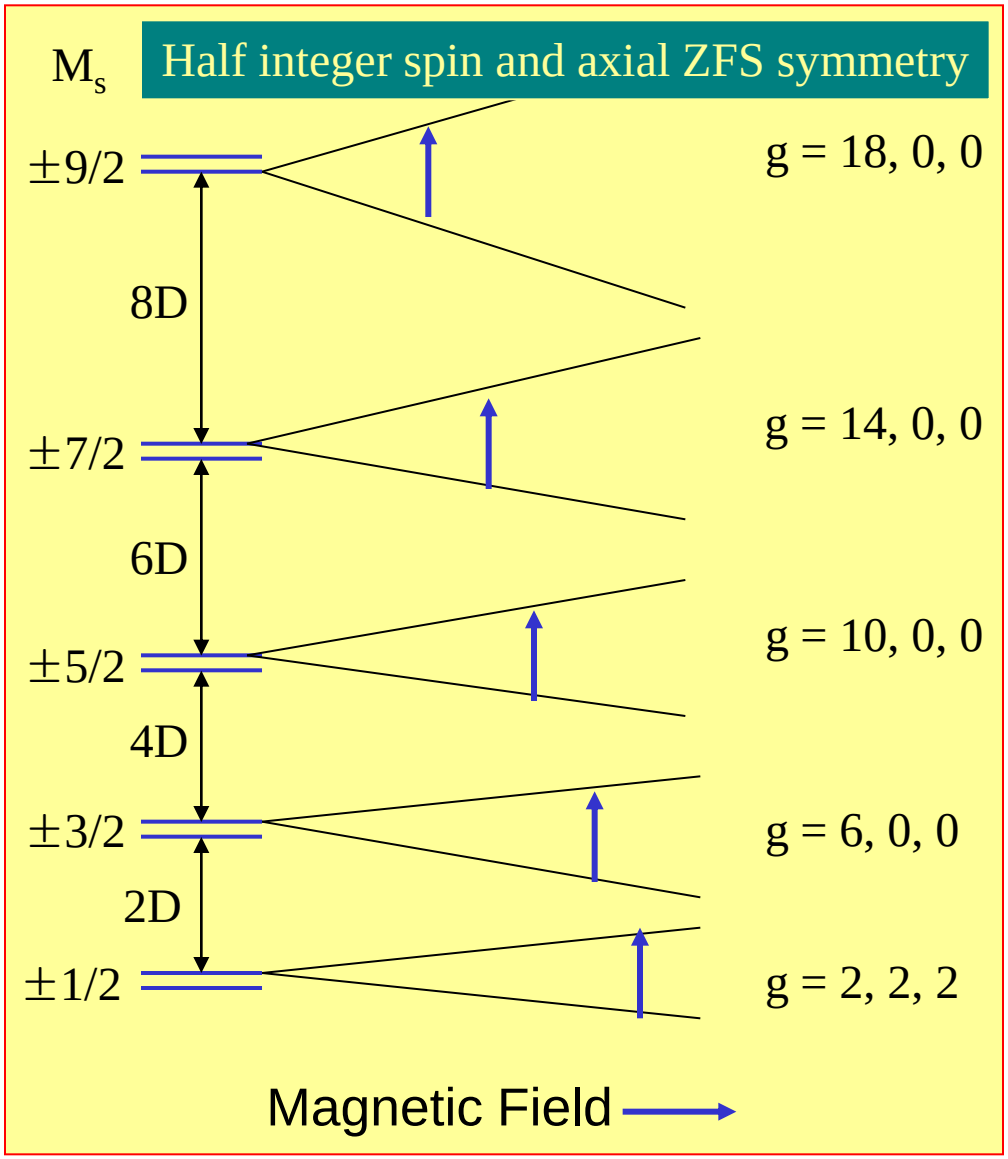

D >> *hν*

S = 9/2

S = 7/2

S = 5/2

S = 3/2

g = 2, 4, 4

g = 2, 6, 6

g = 2, 8, 8

g = 2, 10, 10

The magnitude of the ZFS can be determined by EPR. The populations of each of the doublet has a ***Boltzmann distribution****. By lowering the temperature to the same energy range as the ZFS and by measuring the EPR amplitude of each doublet, a value of the ZFS can be obtained.*

Or we can measure $\Delta M_s = \pm 1$ *transitions, such as* $+5/2 \leftrightarrow +3/2$, *at* ***higher fields****.*

EPR of Co(II) (S = 3/2, d^7)

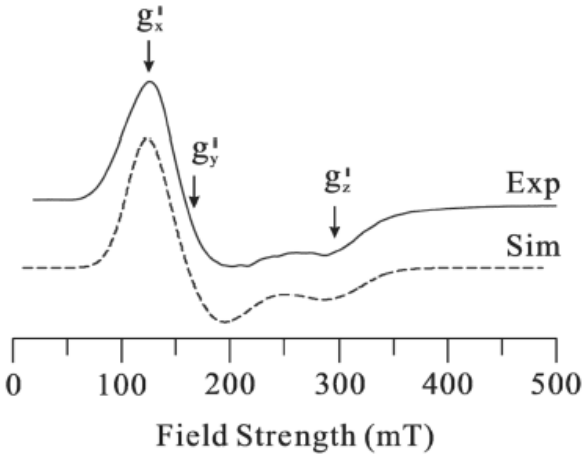

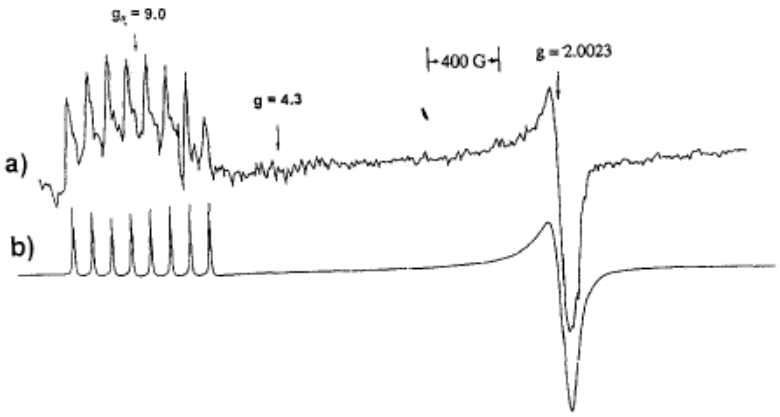

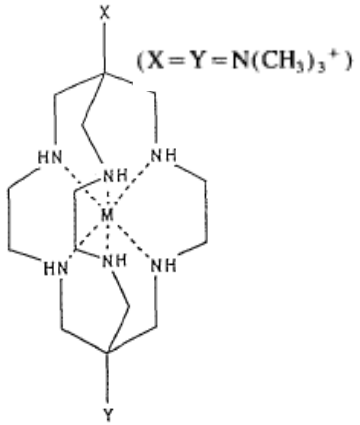

Inorg. Chim. Acta 241, 5 (1996)

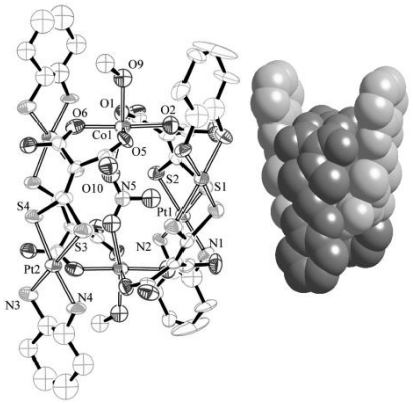

Bull. Kor. Chem. Soc. 27, 193 (2006)

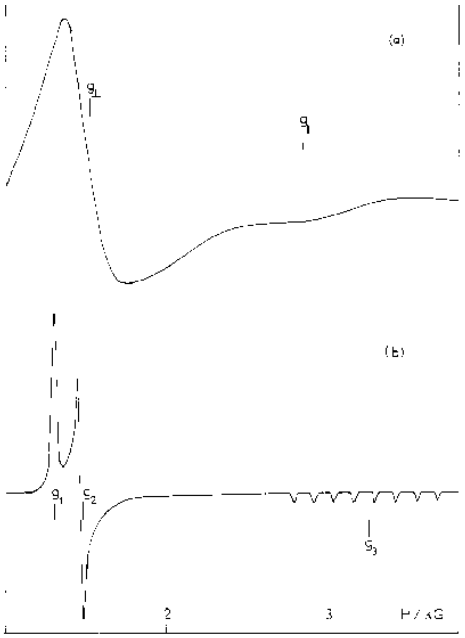

Figure 2. Polycrystalline powder EPR spectra recorded at X-band frequency at 4.2 K: (a) $[Co(DAPSC)(Cl)H_2O]Cl{\cdot}2H_2O$; (b) $[(Co,Zn)(DAPSC)(Cl)H_2O]Cl{\cdot}2H_2O$.

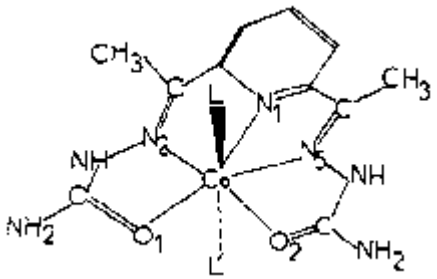

Inorg. Chem. 23, 2725 (1984)

EPR of Fe(III) (S = 5/2, d^5)

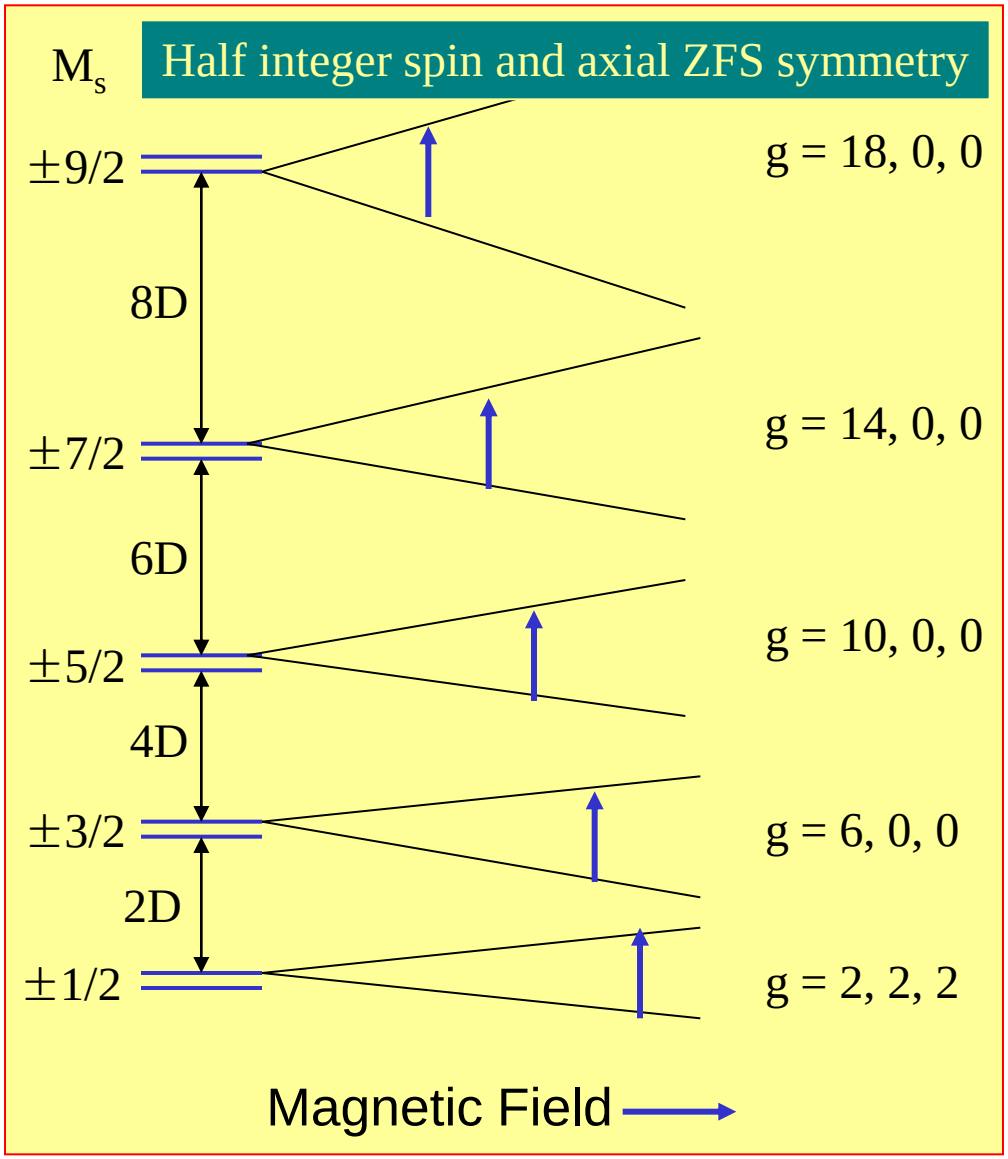

D >> *hν*

S = 9/2

S = 7/2

S = 5/2

S = 3/2

g = 2, 4, 4

g = 2, 6, 6

g = 2, 8, 8

g = 2, 10, 10

The magnitude of the ZFS can be determined by EPR. The populations of each of the doublet has a ***Boltzmann distribution****. By lowering the temperature to the same energy range as the ZFS and by measuring the EPR amplitude of each doublet, a value of the ZFS can be obtained.*

Or we can measure $\Delta Ms = \pm 1$ transitions, such as $+5/2 \leftrightarrow +3/2$, at ***higher fields****.*

EPR of Fe(III) ($S = 5/2$, d^5)

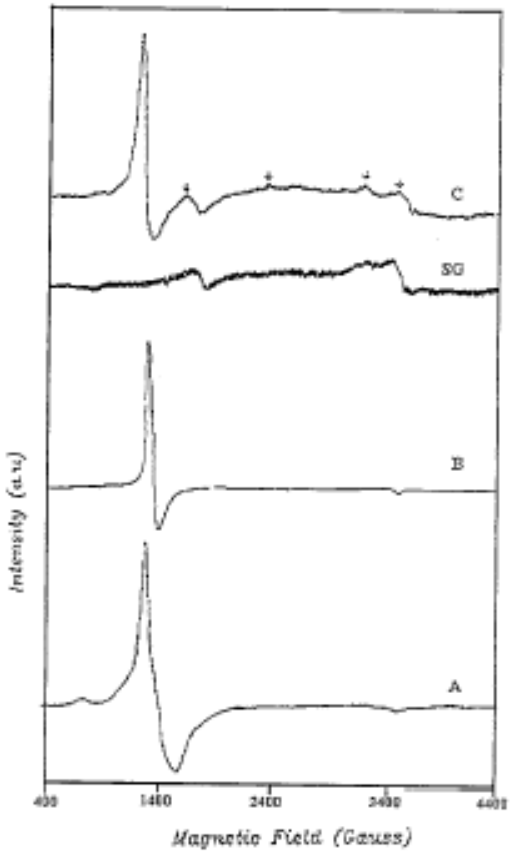

Fig. 4. EPR spectra of (A) Fe(TDCPP)Cl (100 mL, 8.6×10^{-4} mol L^{-1}) in DCE, gain = 8.0×10^{2}; (B) (A) after the addition of 2.1×10^{-6} mol TBAOH, gain = 2.5×10^{2}; (C) 0.0759 g of Fe(TDCPP)SG containing 1.1×10^{-8} mol $Fe(TDCPP)^{+}$/g SG, gain = 1.6×10^{4} (↓ extraneous peaks from the support); (SG) pure SG, gain = 1.6×10^{4}. EPR spectrometer conditions: T = 4.5–5.5 K, microwave frequency = 9.240 GHz.

Ironporphyrin			
$Fe(TPP)^{+}$	$R_1 = R_2 = R_3 = R_4 =$	Ph	X= H
$Fe(TDCPP)^{+}$		2,6 diClPh	H
$Fe(TFPP)^{+}$		C_6F_5	H
$Fe(TDCPCl_8P)^{+}$		2,6 diCl Ph	Cl

Fig. 1. Iron(III)porphyrins.

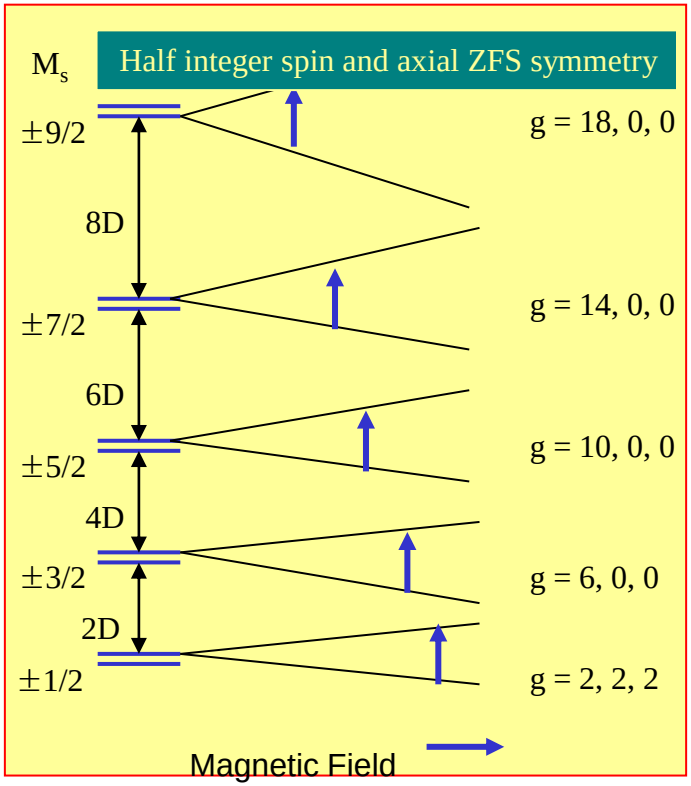

Journal of Molecular Catalysis A : Chemical 116, 405 (1997)

EPR of Fe(III) (S = 5/2, d^5)

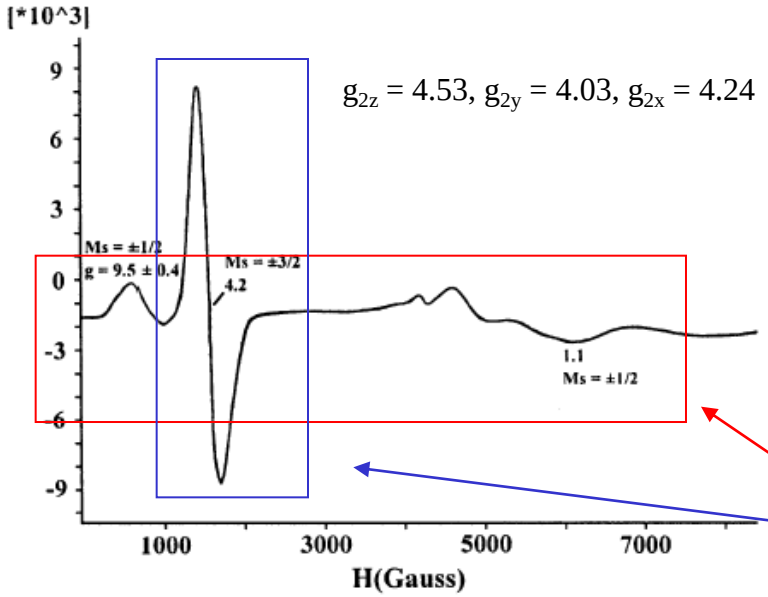

g_{2z} = 4.53, g_{2y} = 4.03, g_{2x} = 4.24

big E/D

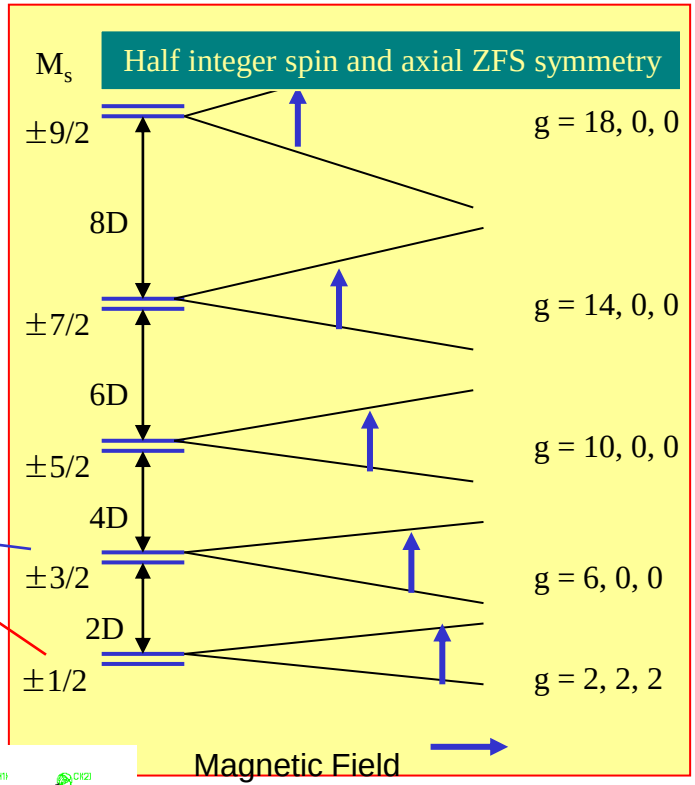

Fig. 5 Solid-state X-band EPR spectrum of a finely powdered sample of **5** at 4 K. EPR conditions: microwave frequency 9.466 GHz; modulation amplitude 1.60 G; modulation frequency 100.00 kHz; microwave power 1.997 mW.

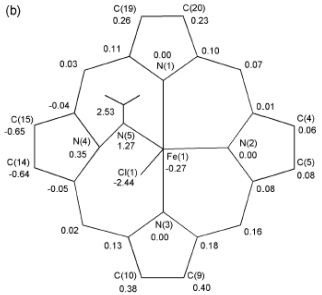

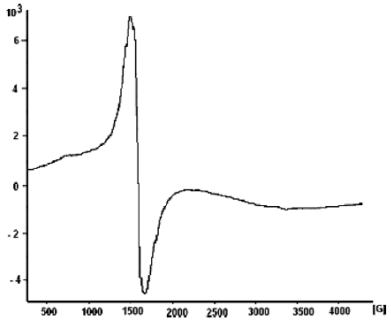

Fig. 5. EPR spectra of [Fe(L^2)(TCC)] (**2**) in CH_2Cl_2 solution at 77 K.

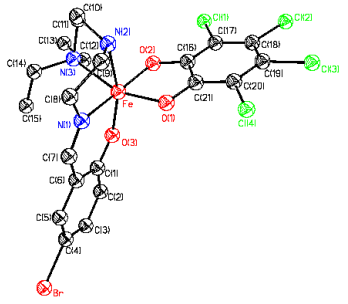

Fig. 2. ORTEP representation (30% thermal ellipsoids) with atom level schemes for **2**.

J. Chem. Soc., Dalton Trans., 3001 (2002)

Inorga. Chim. Acta 360, 2944 (2007)

EPR of Fe(III) ($S = 1/2$, d^5)

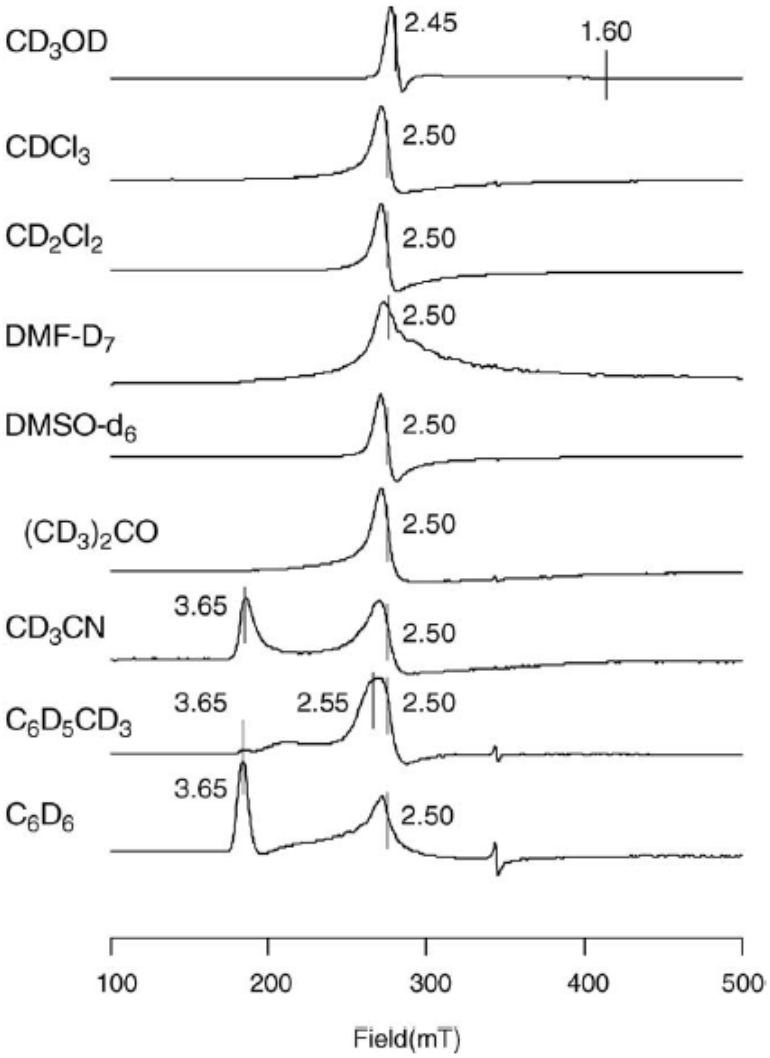

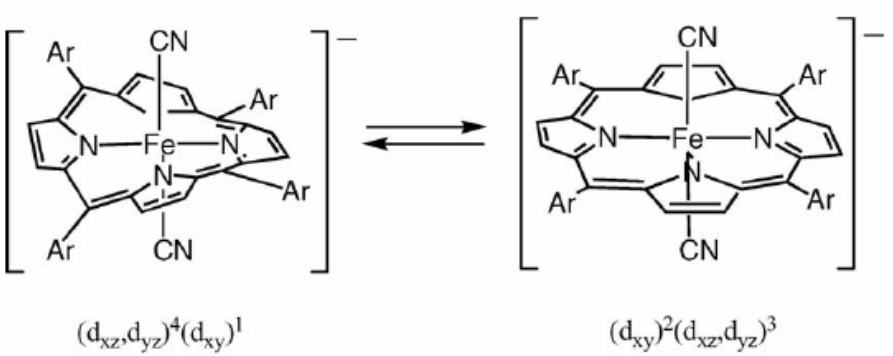

Coordination Chemistry Reviews 250 (2006) 2271–-2294

EPR of Fe(III) ($S = 1/2$, d^5)

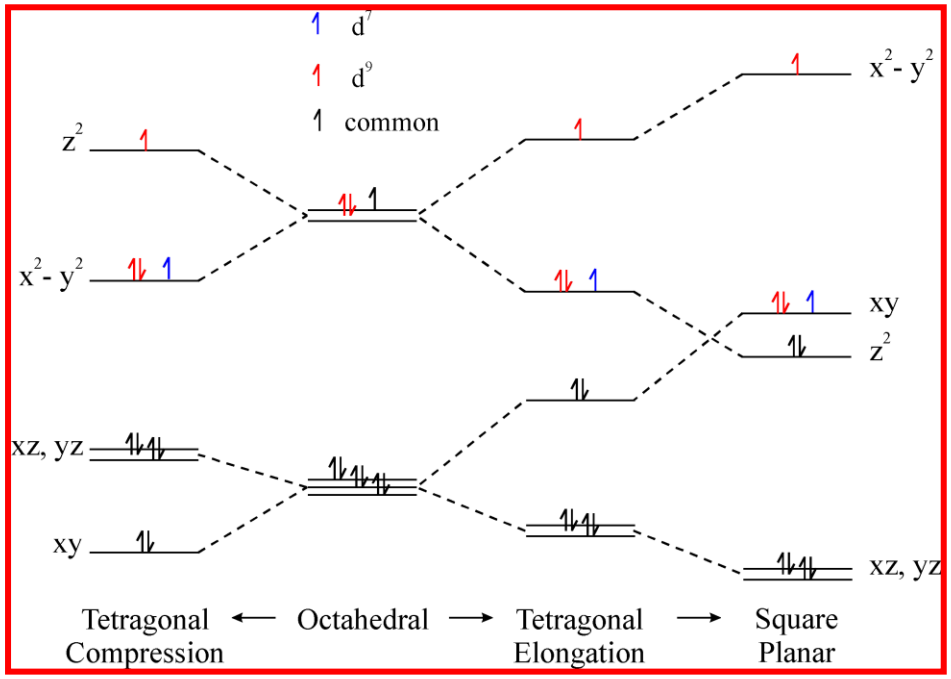

- Magic Pentagon –

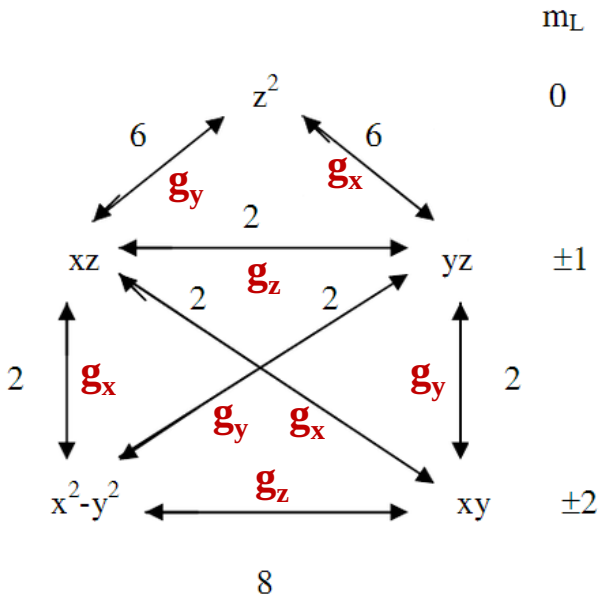

$$g = g_e[1 \pm \frac{n\lambda}{\text{E(ground state)} - \text{E(excited state)}}]$$

$$= g_e[1 + \frac{n\lambda}{\text{E(orbital of unpaired electron in ground state)} - \text{E(orbital of unpaired electron in excited state)}}]$$

for d^5 ($d_{z2}^{\ 1}\, d_{xz,yz}^{\ 4}$ ground)

$g_z \sim g_e = g_\parallel$

$g_{x,y} = g_e\,[1 + 6\lambda / \Delta E_1] = g_\perp$

for d^5 ($d_{xy}^{\ 1}\, d_{xz,yz}^{\ 4}$ ground)

$g_z = g_e\,[1 - 8\,\lambda / \Delta E_1] = g_\parallel$

$g_{x,y} = g_e\,[1 + 2\lambda / \Delta E_2] = g_\perp$

for d^5 ($d_{xy}^{\ 2}\, d_{xz,yz}^{\ 3}$ ground)

$g_z = g_e\,[1 + 8\,\lambda / \Delta E_1] = g_\parallel$

$g_{x,y} = g_e\,[1 - 2\lambda / \Delta E_2] = g_\perp$

EPR of Fe(III) (S = 1/2, d^5)

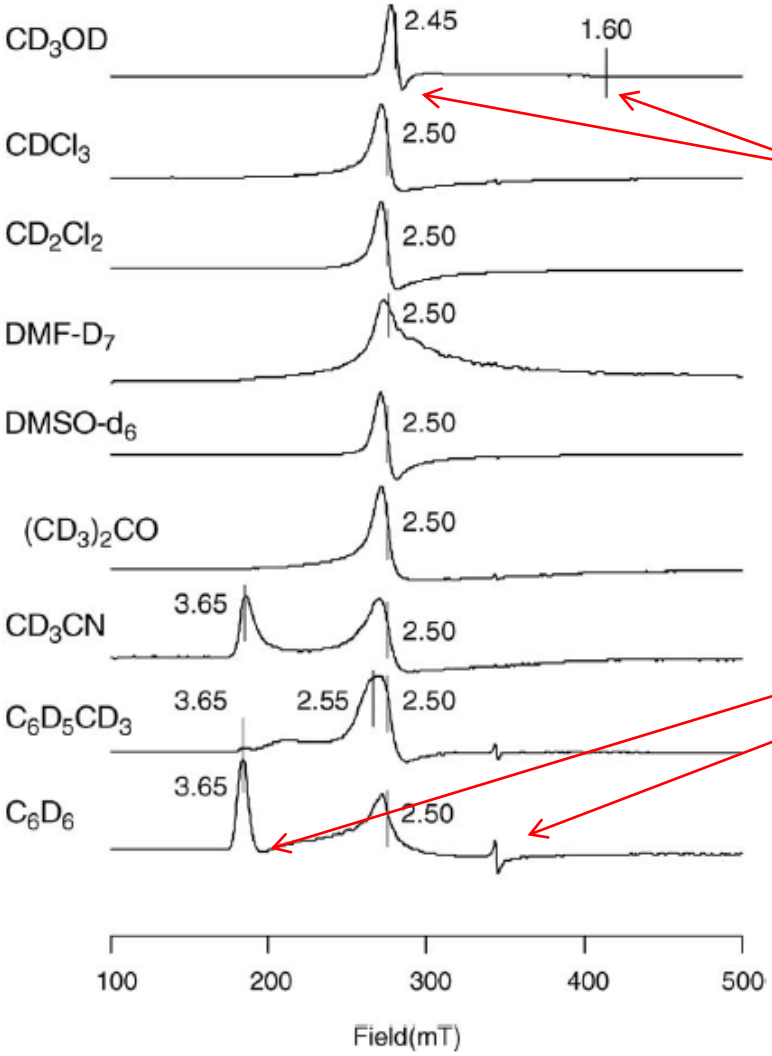

for d^5 ($d_{xy}^1 d_{xz,yz}^4$ ground)

$g_z = g_e [1 - 8\lambda / \Delta E_1] = g_\parallel$

$g_{x,y} = g_e [1 + 2\lambda / \Delta E_2] = g_\perp$

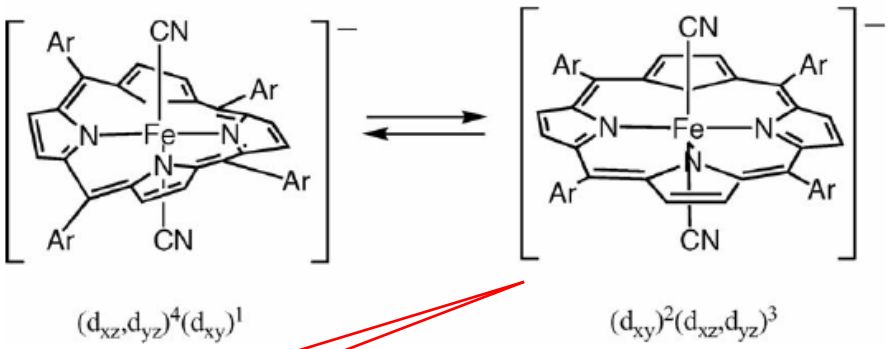

for d^5 ($d_{xy}^2 d_{xz,yz}^3$ ground)

$g_z = g_e [1 + 8\lambda / \Delta E_1] = g_\parallel$

$g_{x,y} = g_e [1 - 2\lambda / \Delta E_2] = g_\perp$

Coordination Chemistry Reviews 250 (2006) 2271–-2294

EPR of Fe(III) (S = 1/2, d^5)

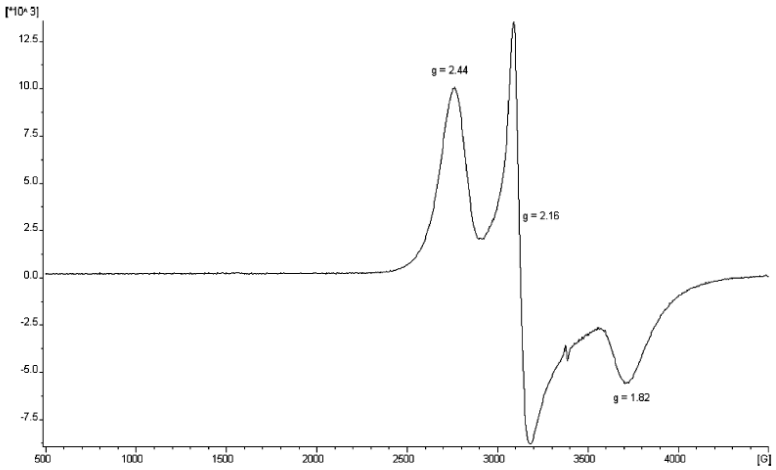

Fig. 6. EPR spectrum of $[Fe(TPC)(PPh(OMe)_2)_2]CF_3SO_3$ (**1**) as a CH_2Cl_2 glass, recorded at 4 K.

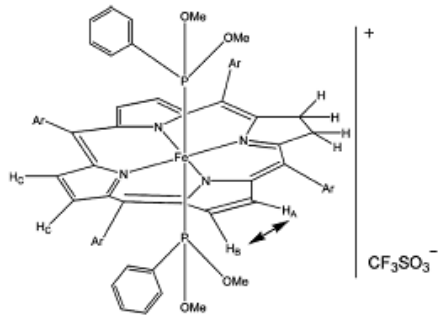

for d^5 ($d_{xy}^{\ 1}\ d_{xz,yz}^{\ 4}$ ground)

$g_z = g_e [1 - 8\lambda / \Delta E_1] = g_\parallel$

$g_{x,y} = g_e [1 + 2\lambda / \Delta E_2] = g_\perp$

Inorganica Chimica Acta 343, 18 (2003)

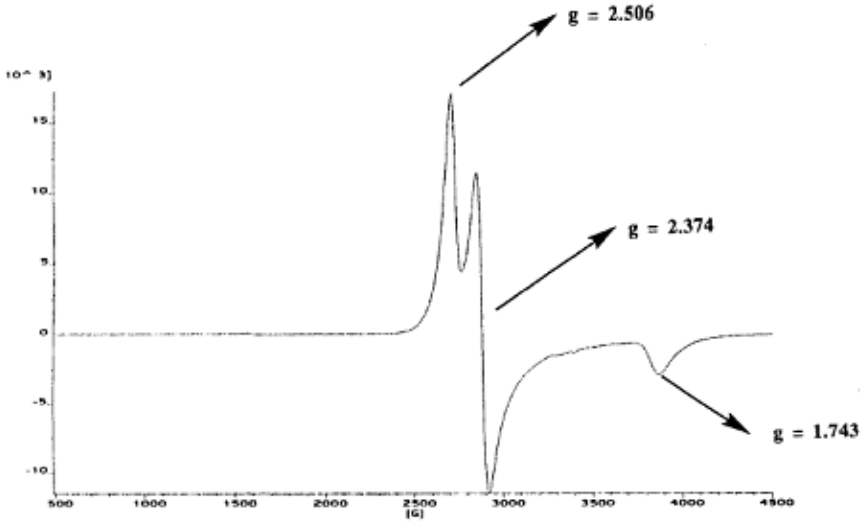

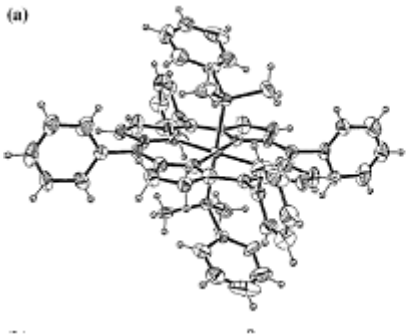

Inorg. Chem. 40, 4494-4499 (2001)

EPR of Mn(II) (S = 5/2, d^5)

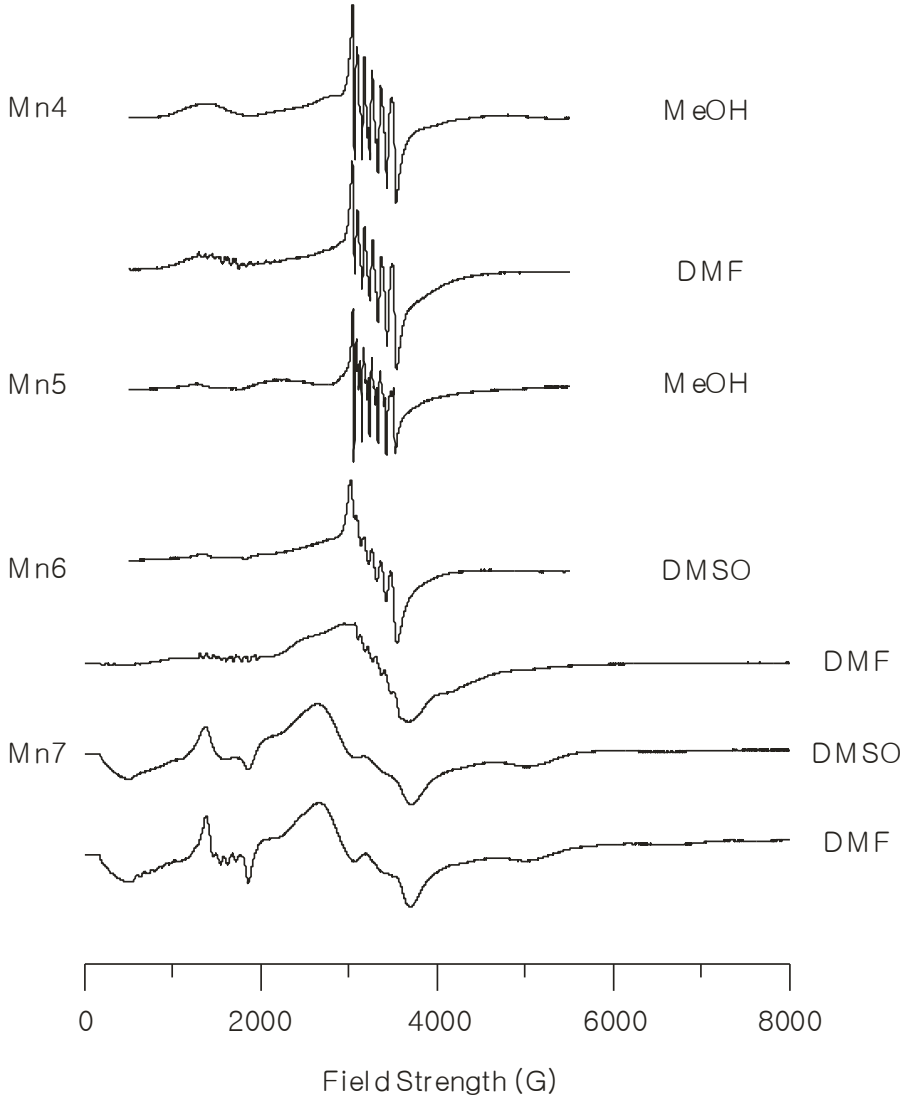

4

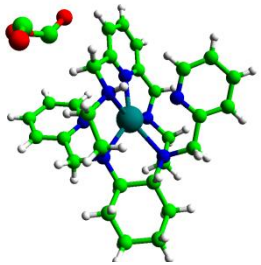

5

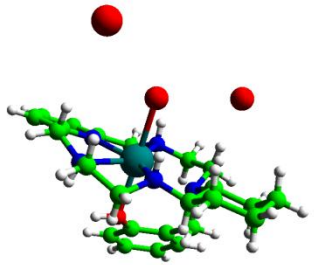

6

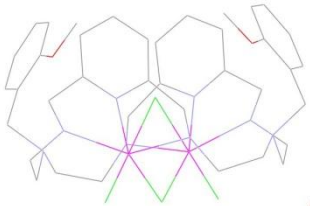

7

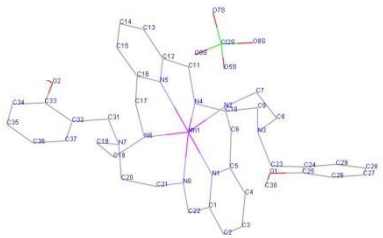

EPR of Mn(II) ($S = 5/2$, d^5)

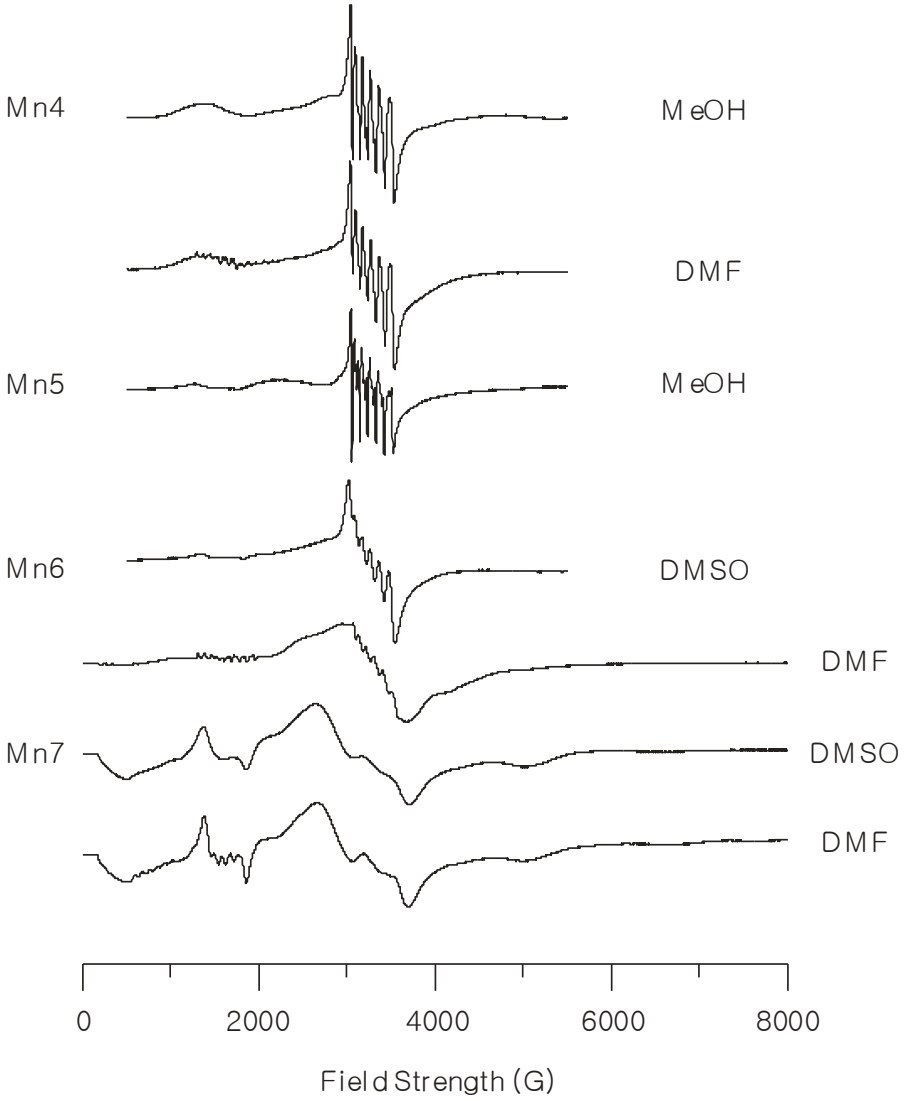

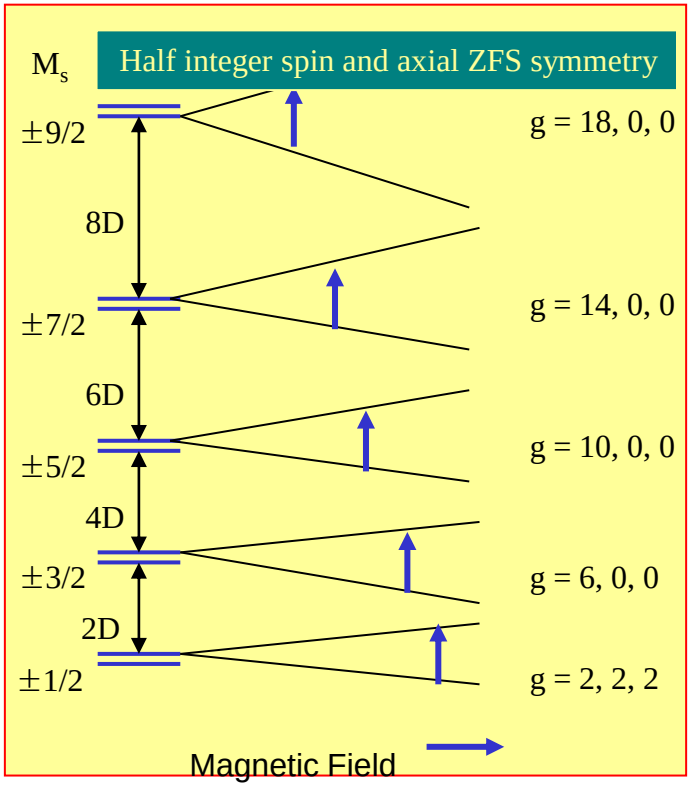

^{55}Mn (100%), I=5/2

EPR of Mn(II) (S = 1/2, d^5)

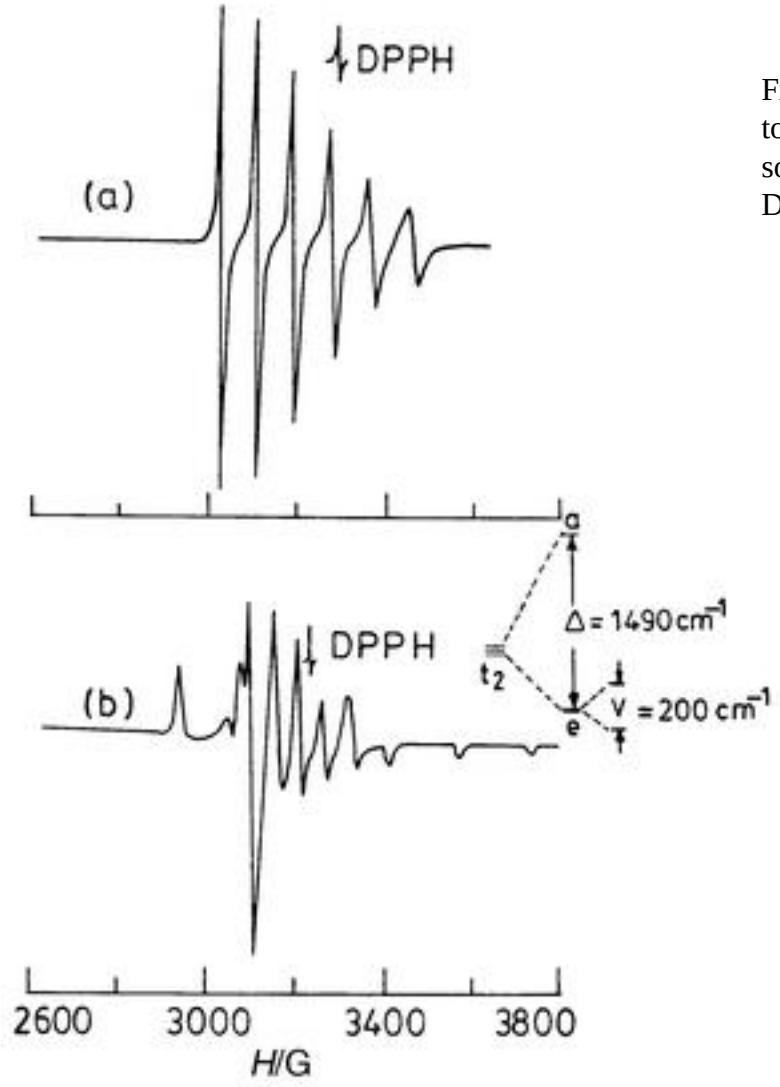

Fig. 1 EPR spectra of [Mn(L1)2] in (a) 11 dichloromethane toluene solution at 300 K, (b) frozen 11 dichloromethane toluene solution at 77 K, showing computed splittings of t2 orbitals. DPPH = Diphenylpicrylhydrazyl.

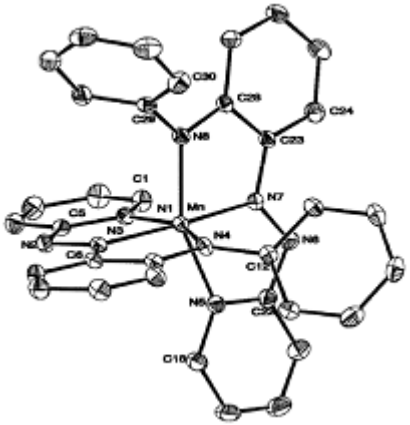

*J. Chem. Soc., Dalton Trans.*1703–1708 (2000)

EPR of V(IV) (S = 1/2, d^1)

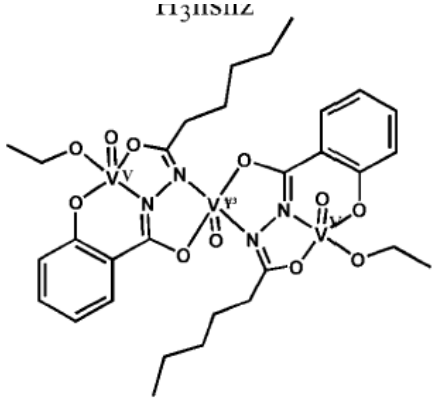

$V_3O_3(hshz)_2(OEt)_2$

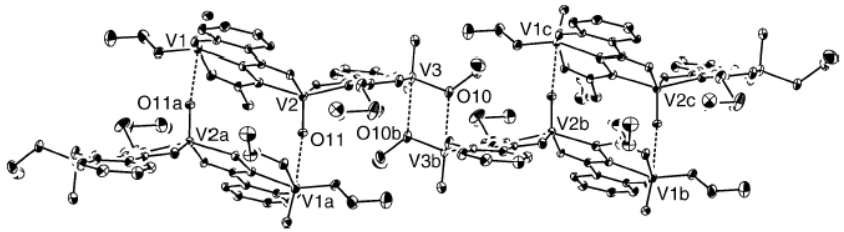

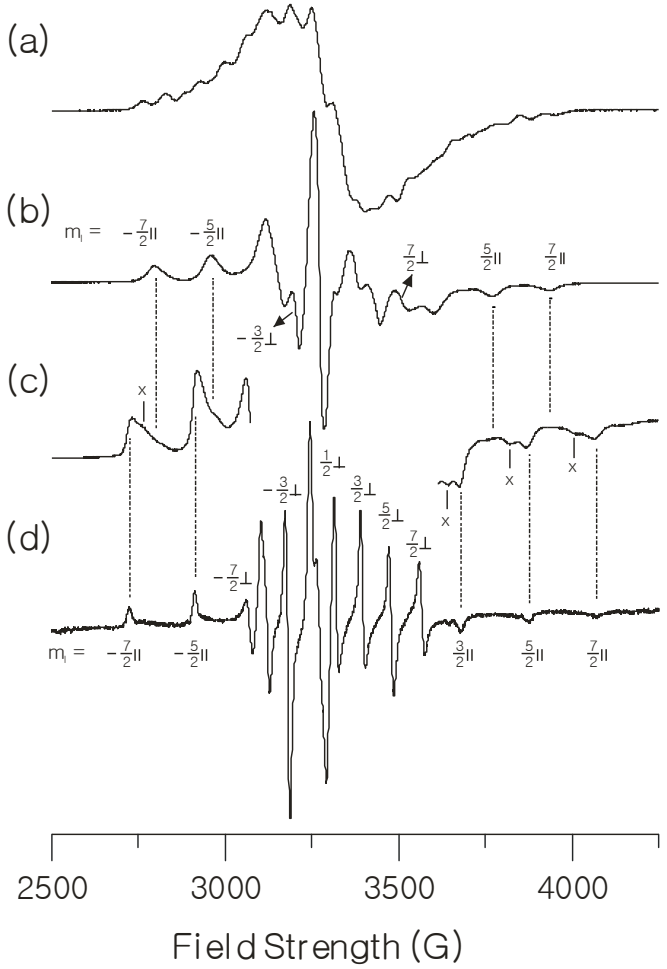

^{51}V (99.8 %), I = 7/2

small g anisotroy, big nuclear hyperfine

Dalton trans. 797-803 (2005)

EPR of FeMo-co ($S = 3/2, 1/2, d^{43}$)

Resting (S=3/2)

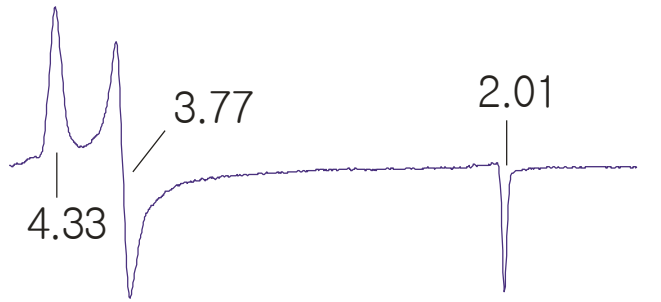

lo-CO (S=1/2)

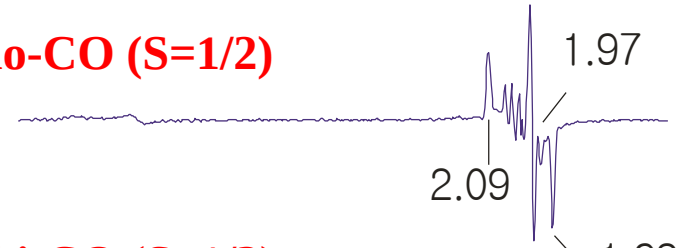

hi-CO (S=1/2)

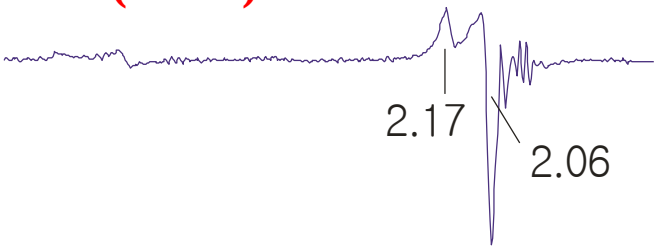

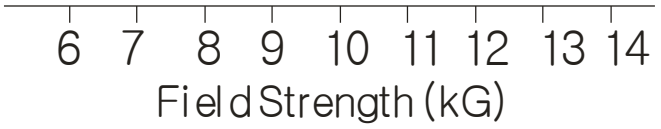

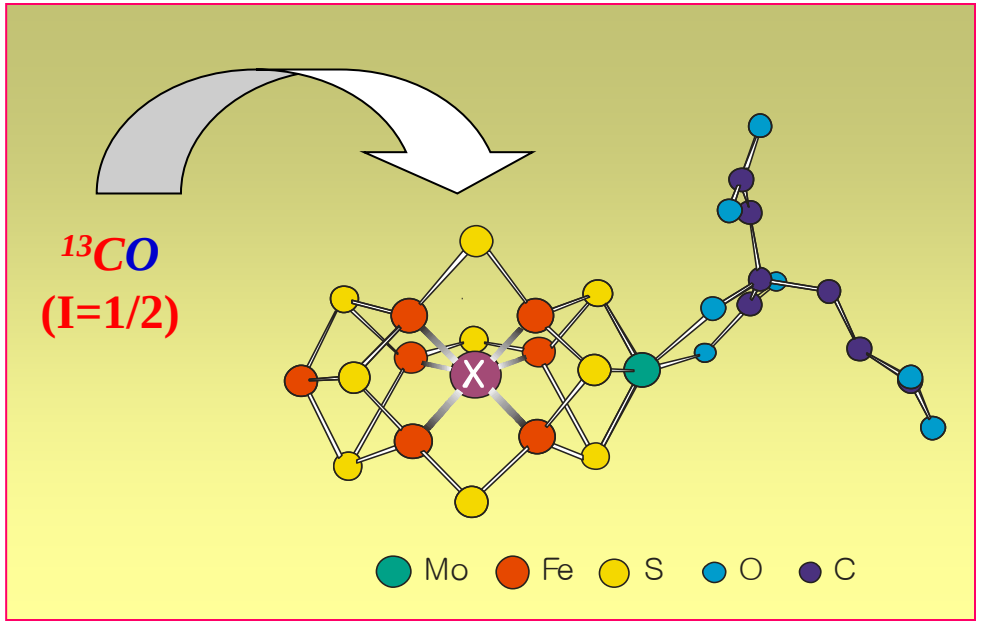

ENDOR/ ESEEM

EPR of FeS-clusters

in J. Am. Chem. Soc., Vol. 120, No. 5, 1998 863

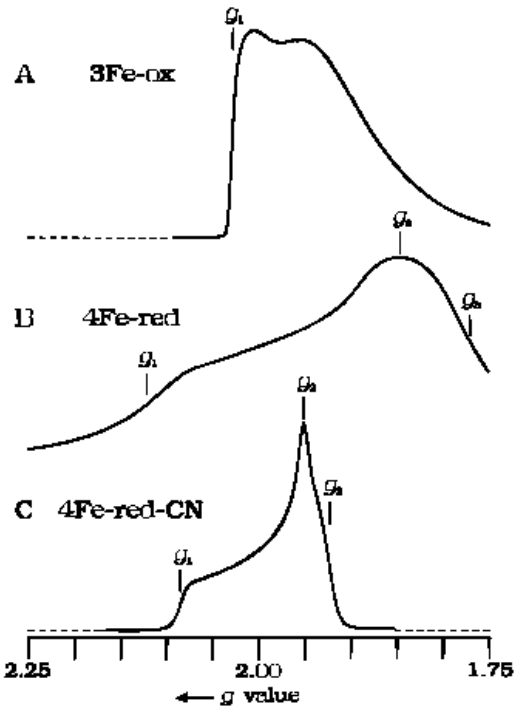

Figure 1. Q-band CW EPR spectra of *Pf*-Fd: (A) *Pf*-Fd 3Fe-ox, (B) *Pf*-Fd 4Fe-red, (C) *Pf*-Fd 4Fe−CN. *Experimental conditions*: (A) temperature, 2 K; microwave frequency, 34.987 GHz; microwave power, 20 μW (40 dBm); 100 kHz field modulation amplitude, 0.13 mT; time constant, 32 ms; (B) as in (A) except: microwave frequency, 35.040 GHz; (C) as in (A) except: microwave frequency, 34.905 GHz; microwave power, 2 μW (50 dBm). The canonical g values are indicated for each spectrum, where determinable.

Interactions measured by EPR

$$H = \beta \mathbf{S}\cdot\mathbf{g}\cdot\mathbf{H} + \mathbf{S}\cdot\mathbf{A}\cdot\mathbf{I} + \mathbf{D}[S_z^2 - 1/3\ S(S+1) + \mathbf{E}/\mathbf{D}(S_x^2 - S_y^2)]$$

Electron Zeeman interaction (interaction of the spin with the applied field)

Spin orbit coupling

Hyperfine and superhyperfine interactions (electron spin-nuclear spin interaction)

Spin-spin interaction

* Nuclear quadrupole interation can also be detacted.

- High sensitivity (<1 μM to 0.1 mM)
- No background
- Definitive and Quantitative

Electron spin – Nuclear spin Interaction

Phenalenyl radical

$a_{H(2)}$= -5,09 MHz (3x)
$a_{C(2)}$= -21.90 MHz (3x)
$a_{H(1)}$= -17,67 MHz (6x)
$a_{C(1)}$= 26.96 MHz (6x)

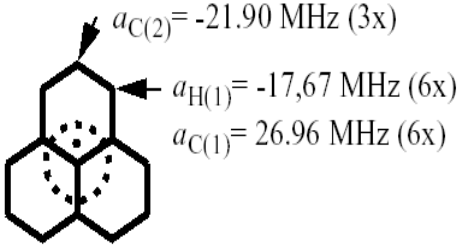

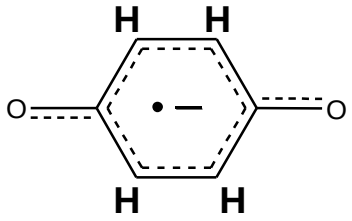

S=½;
I=1/2 x 4
Quintet

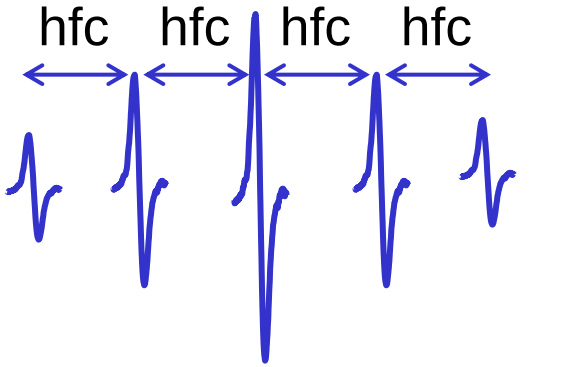

EPR spectrum:

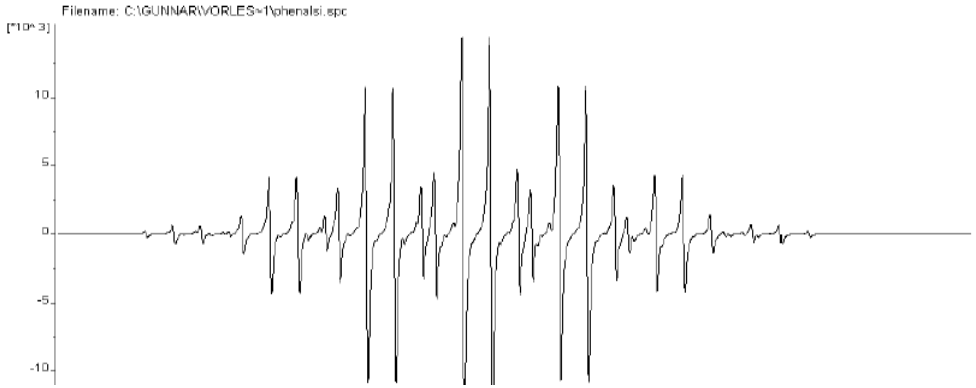

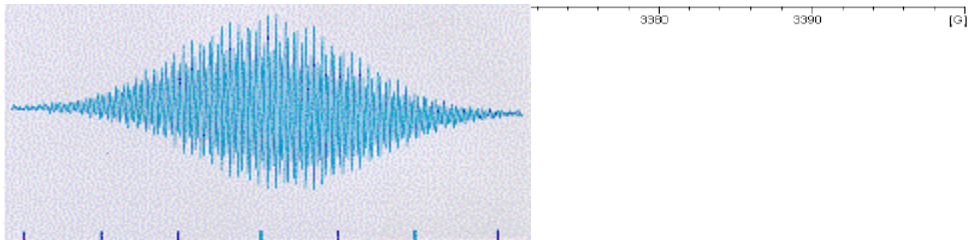

Electron Nuclear Double Resonance (ENDOR)

Phenalenyl radical

$a_{H(2)}$= -5,09 MHz (3x)
$a_{C(2)}$= -21.90 MHz (3x)
$a_{H(1)}$= -17,67 MHz (6x)
$a_{C(1)}$= 26.96 MHz (6x)

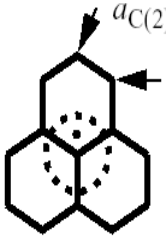

EPR spectrum:

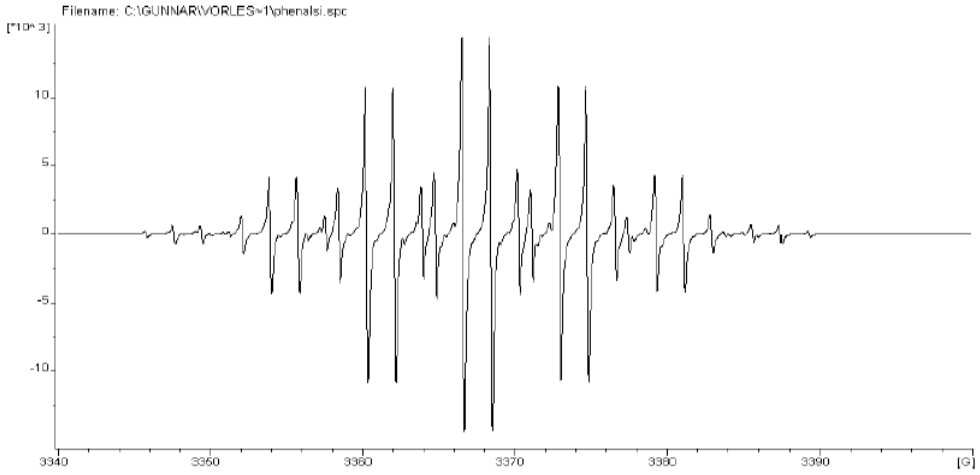

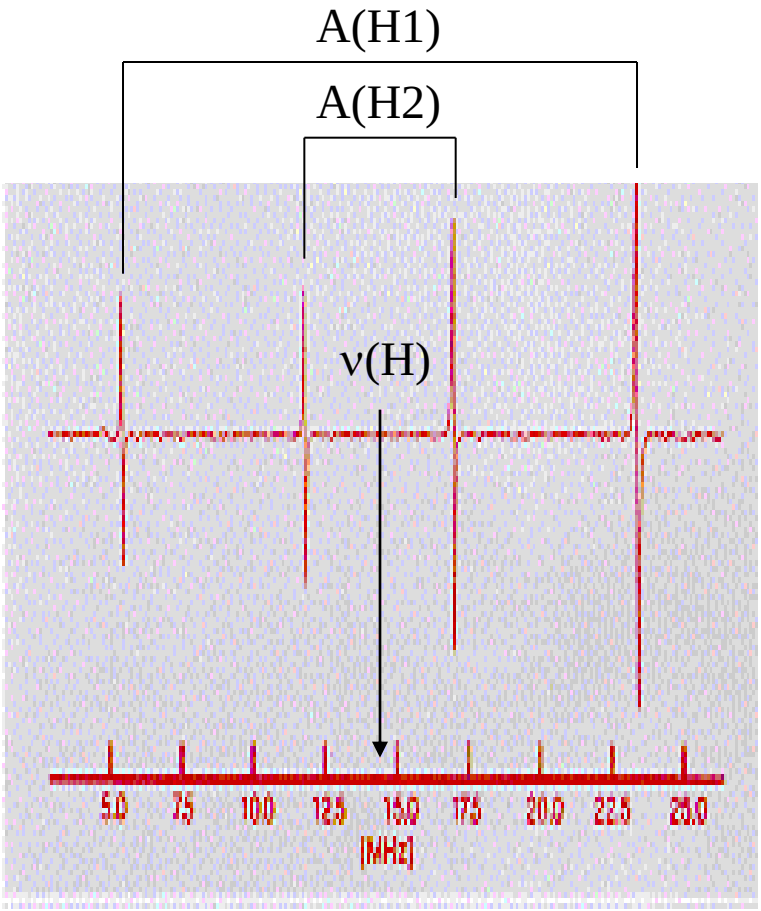

ENDOR Spectrum

$$H = \beta \mathbf{S}\cdot\mathbf{g}\cdot\mathbf{H} + g_n\beta_n\mathbf{I}\cdot\mathbf{H} + \mathbf{S}\cdot\mathbf{A}\cdot\mathbf{I}$$

Electron Nuclear Double Resonance (ENDOR)

ENDOR = EPR-detected NMR

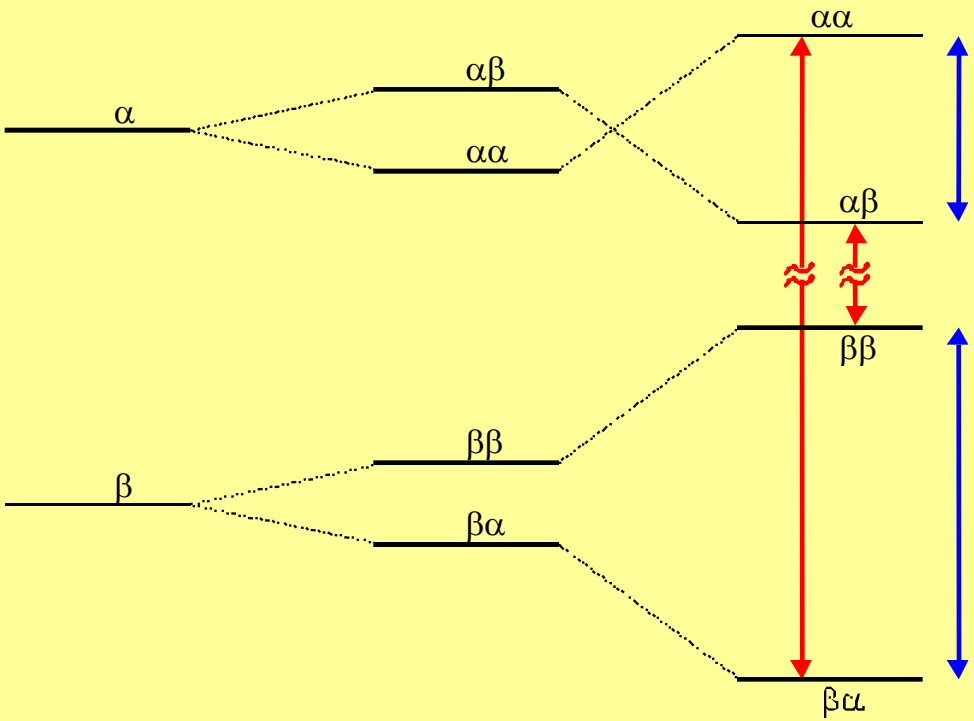

S' = 1/2 I = 1/2

Electronic Zeeman interaction	Nuclear Zeeman interaction	Hyperfine Interaction

$$H = \beta \mathbf{S}\cdot\mathbf{g}\cdot\mathbf{H} + g_n\beta_n\mathbf{I}\cdot\mathbf{H} + \mathbf{S}\cdot\mathbf{A}\cdot\mathbf{I}$$

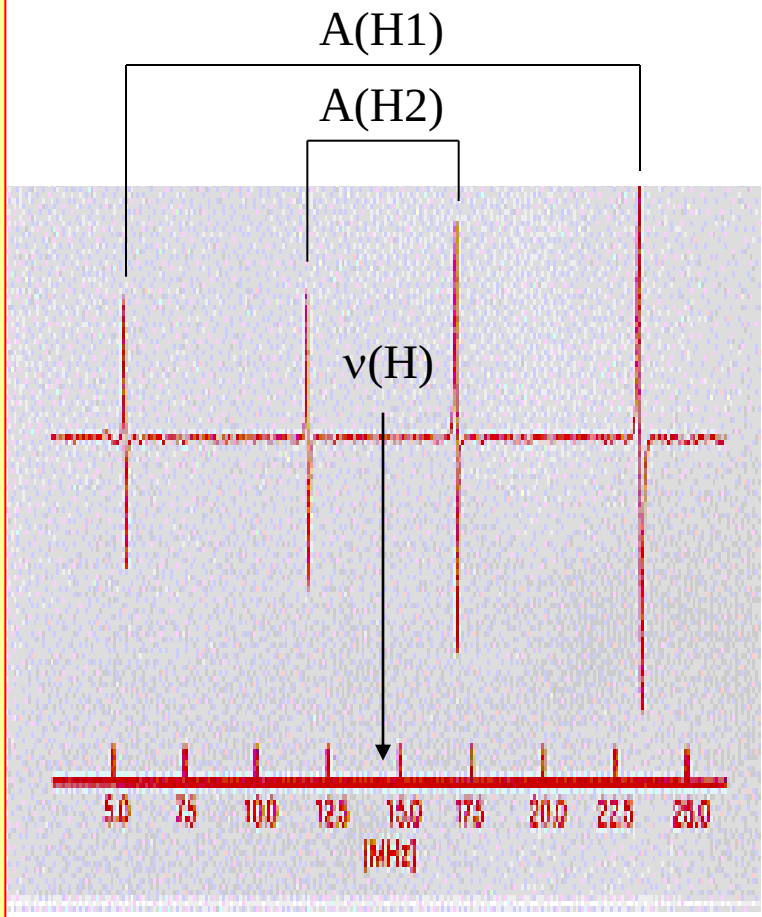

ENDOR Spectrum

Electron Nuclear Double Resonance (ENDOR)

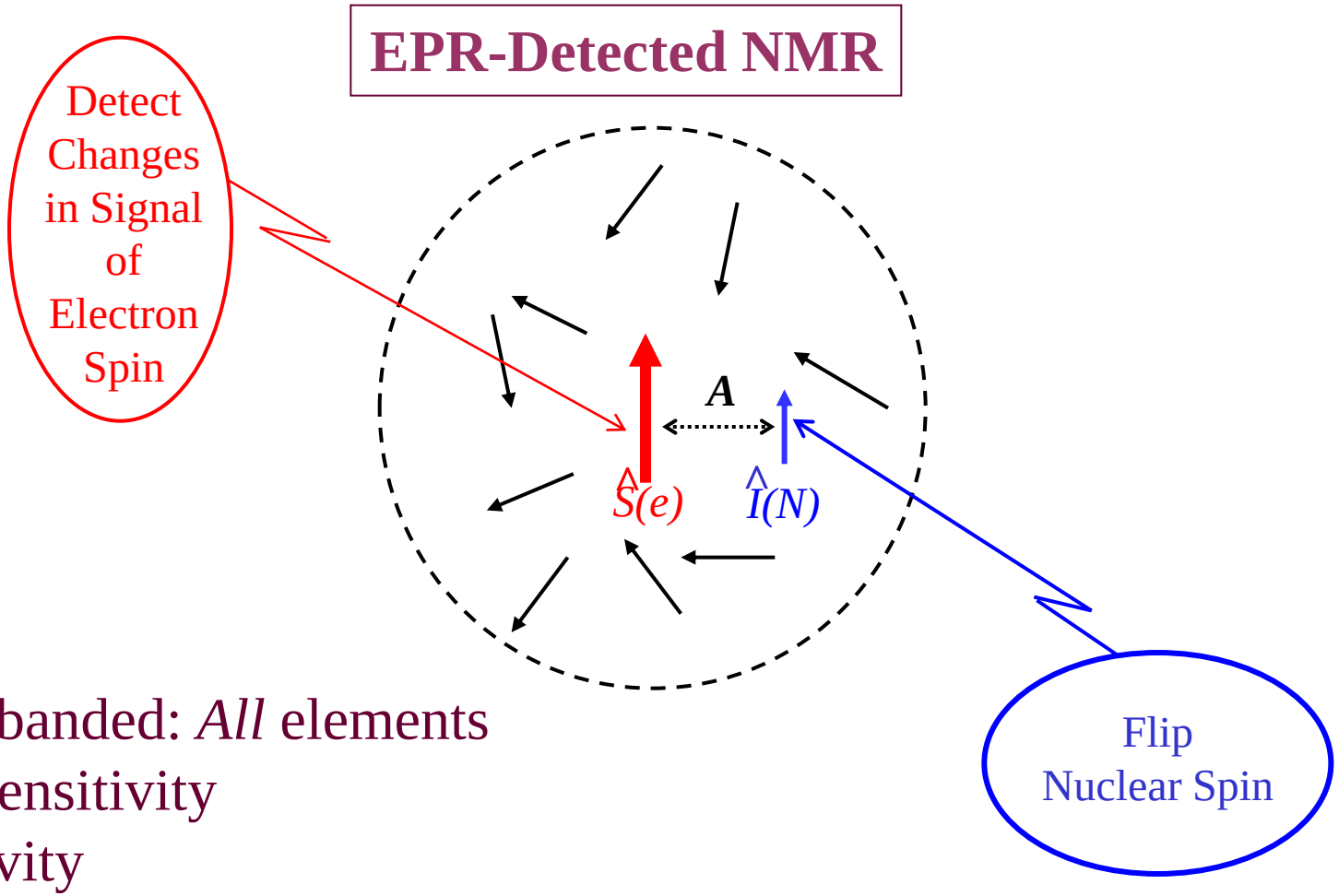

- Broad-banded: *All* elements
- High Sensitivity
- Selectivity

$$H = \beta \mathbf{S}\cdot\mathbf{g}\cdot\mathbf{H} + g_n\beta_n \mathbf{I}\cdot\mathbf{H} + \mathbf{S}\cdot\mathbf{A}\cdot\mathbf{I}$$

Electron Nuclear Double Resonance (ENDOR)

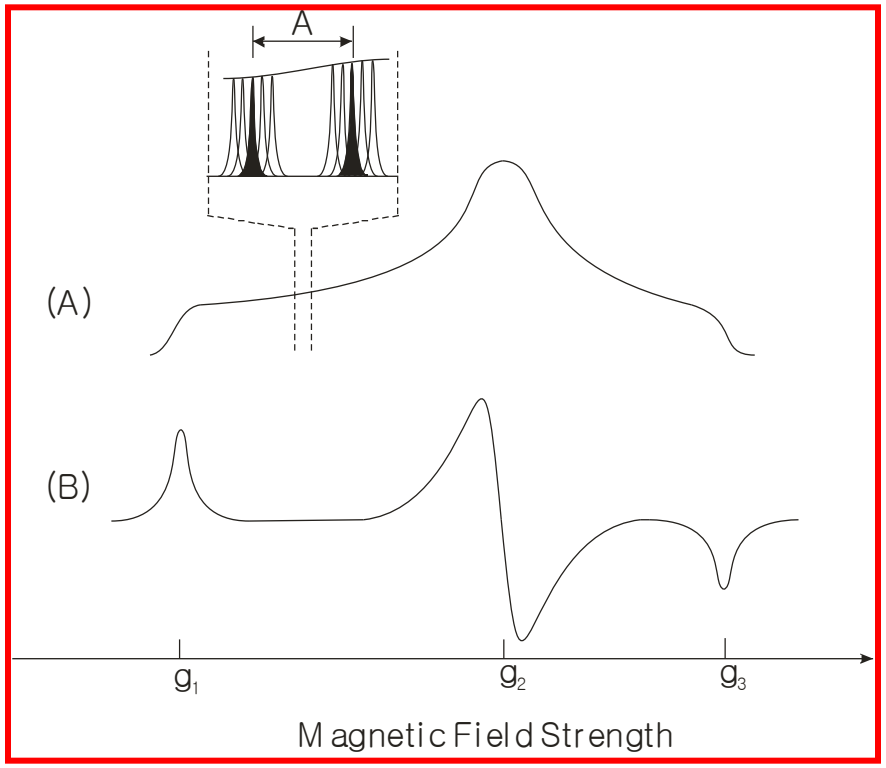

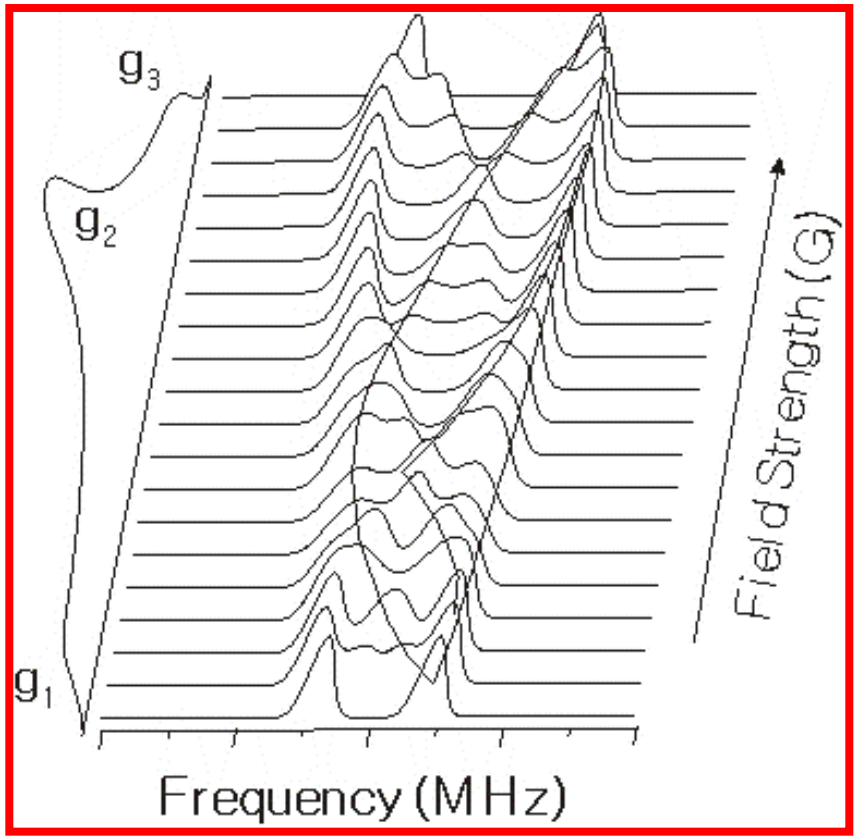

$$H = \beta \mathbf{S}\cdot\mathbf{g}\cdot\mathbf{H} + g_n\beta_n \mathbf{I}\cdot\mathbf{H} + \mathbf{S}\cdot\mathbf{A}\cdot\mathbf{I}$$

Electron Nuclear Double Resonance (ENDOR)

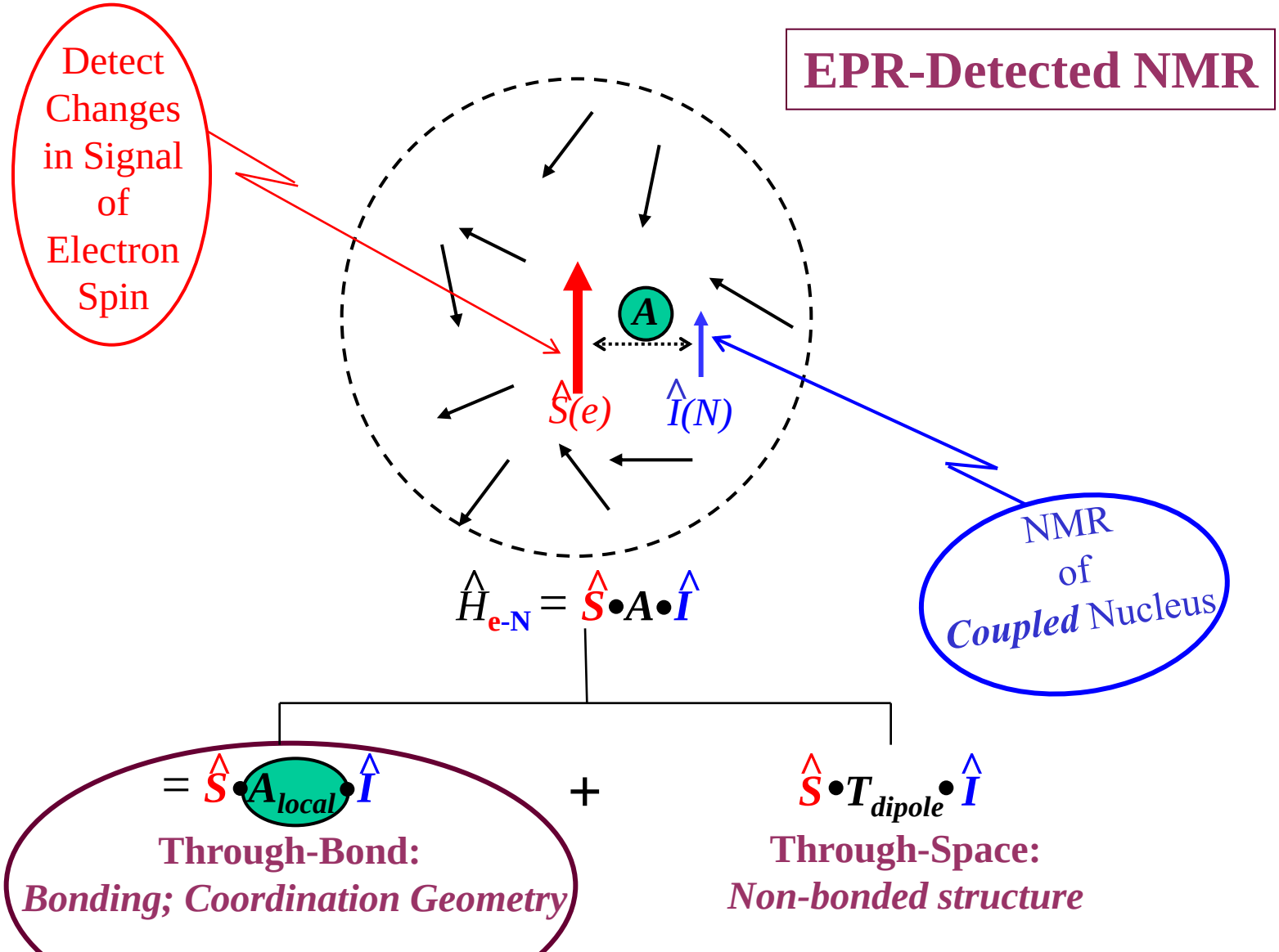

Electron Nuclear Double Resonance (ENDOR)

CW ENDOR

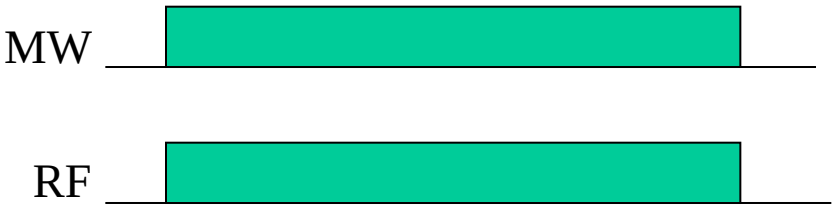

Davise ENDOR (Pulsed ENDOR)

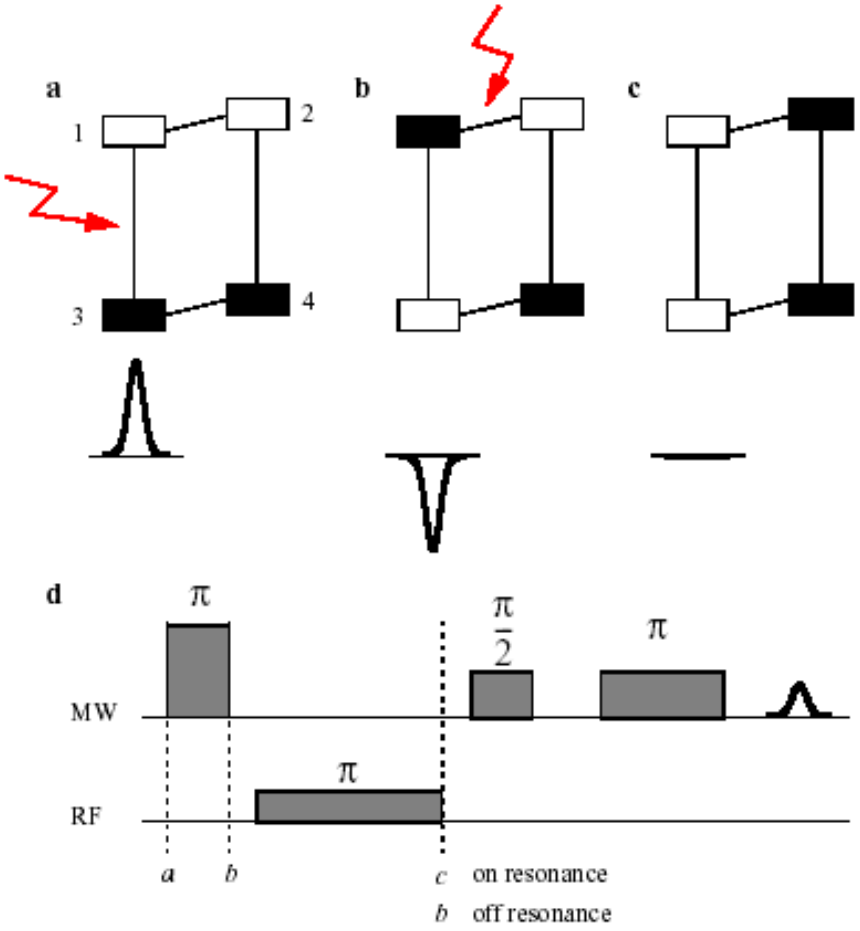

Electron Nuclear Double Resonance (ENDOR)

Mims ENDOR (Pulsed ENDOR)

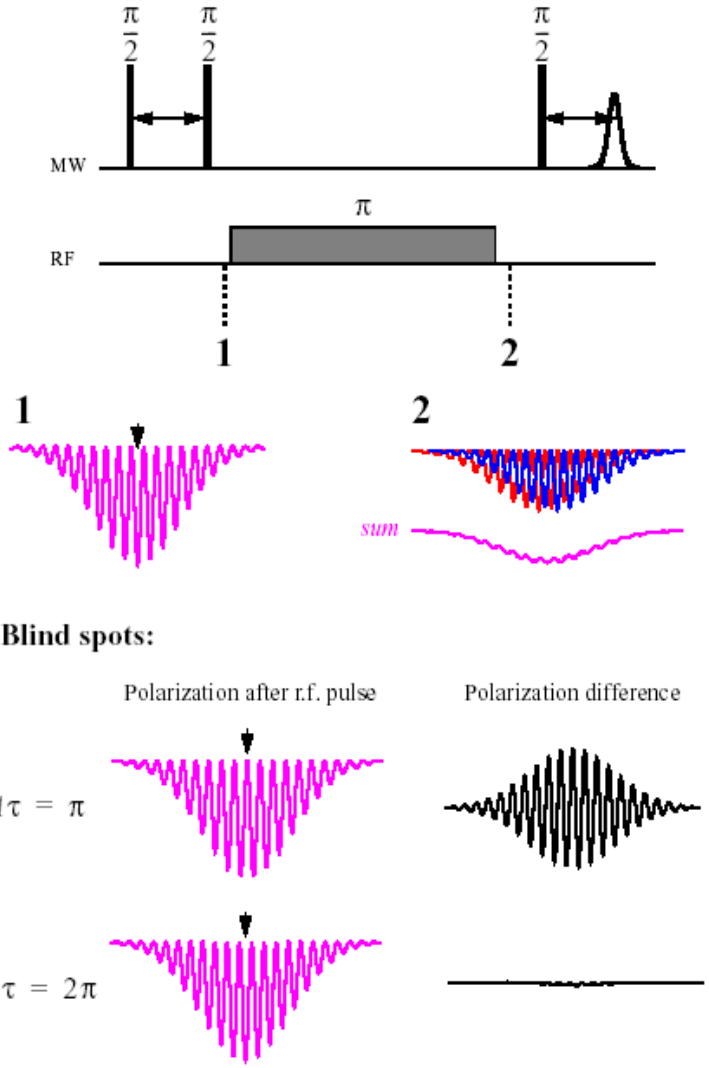

Davise ENDOR (Pulsed ENDOR)

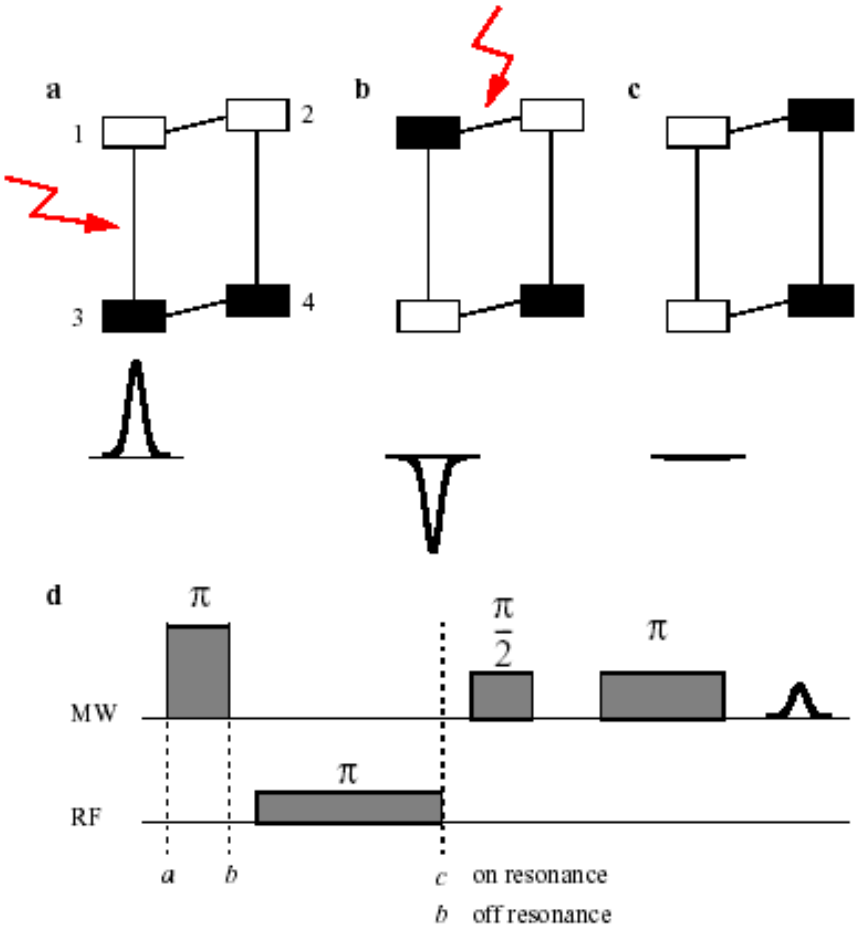

Applications – Metalloenzymes (Ni-SOD)

Ni-SOD

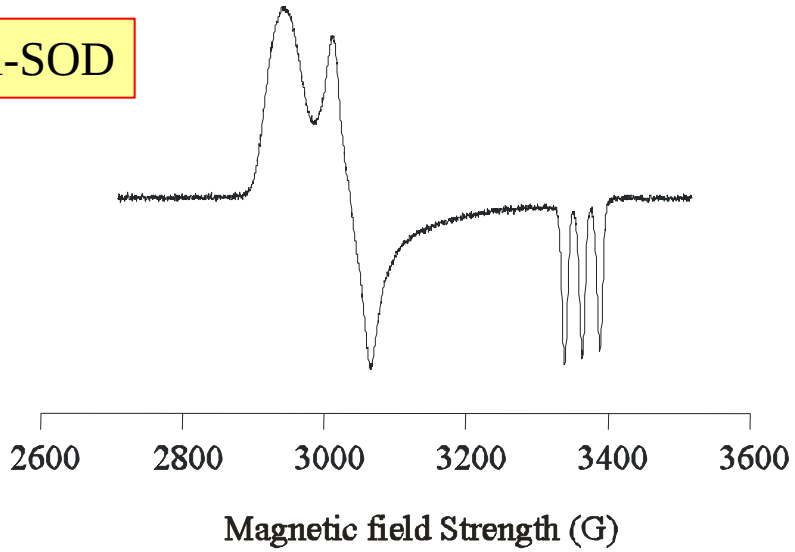

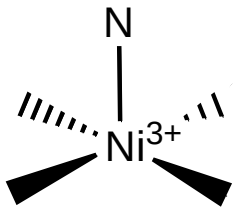

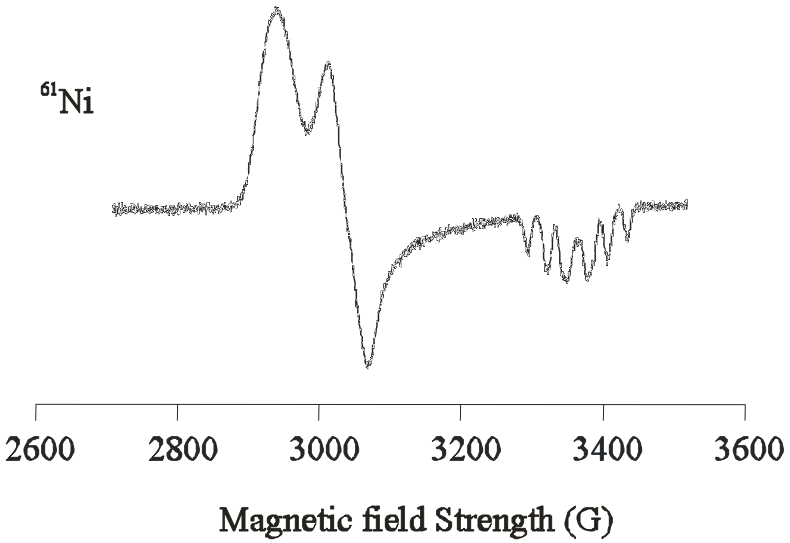

Applications – Metalloenzymes (Ni-SOD)

Ni-SOD

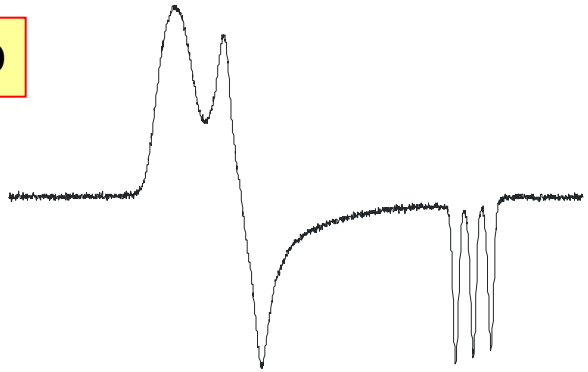

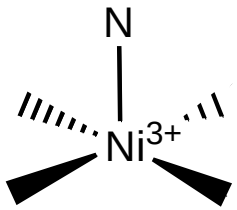

ESEEM:EPR-detected NMR w/o RF

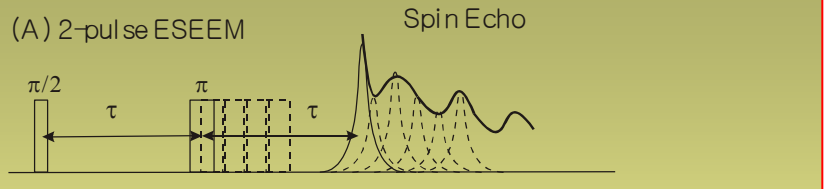

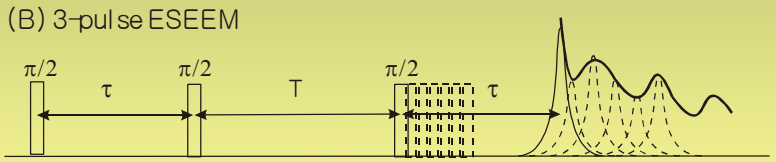

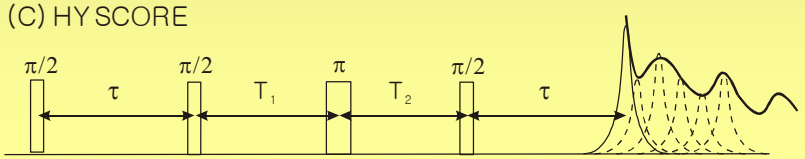

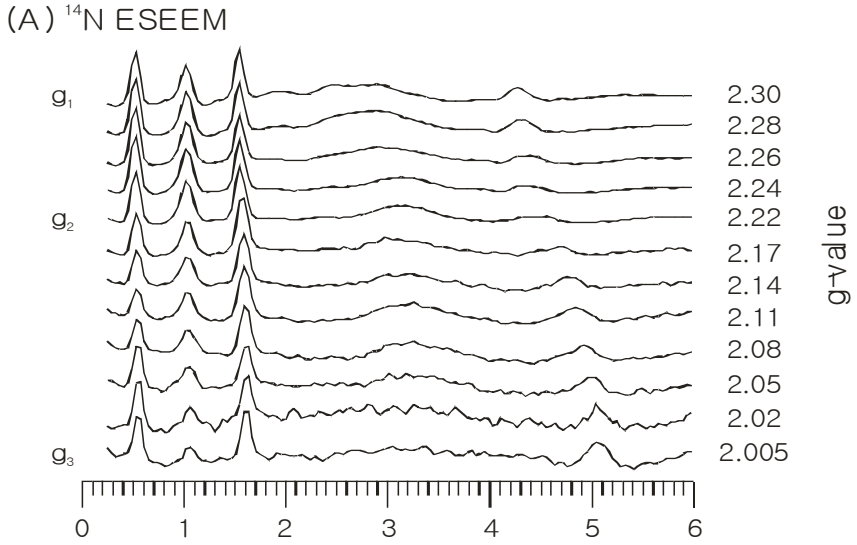

ESEEM (electron spin echo envelope modulation)

Applications – Metalloenzymes (N_2ase)

Nitrogenase

$[Fe_7MoS_9X]$
FeMo-cofactor

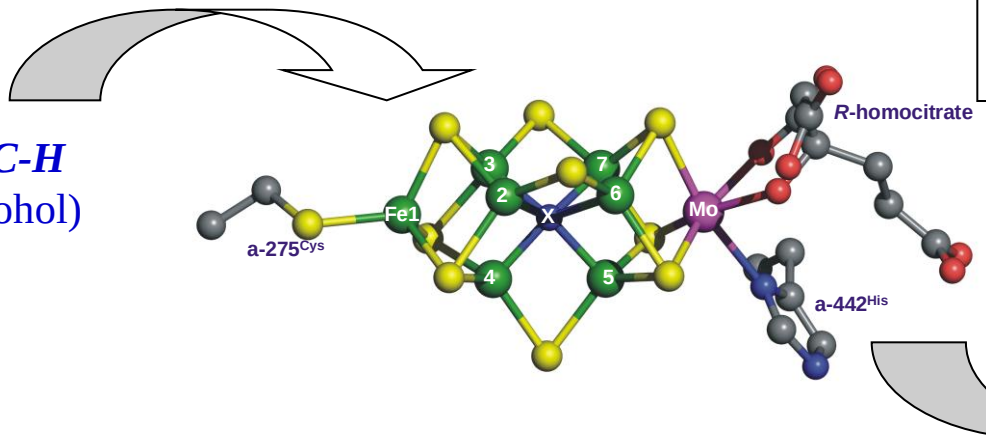

HO-CH$_2$-C≡C-H
(Propargyl Alcohol)

HO-CH$_2$-CH=CH$_2$
(Allyl Alcohol)

2e$^-$ + 2H$^+$

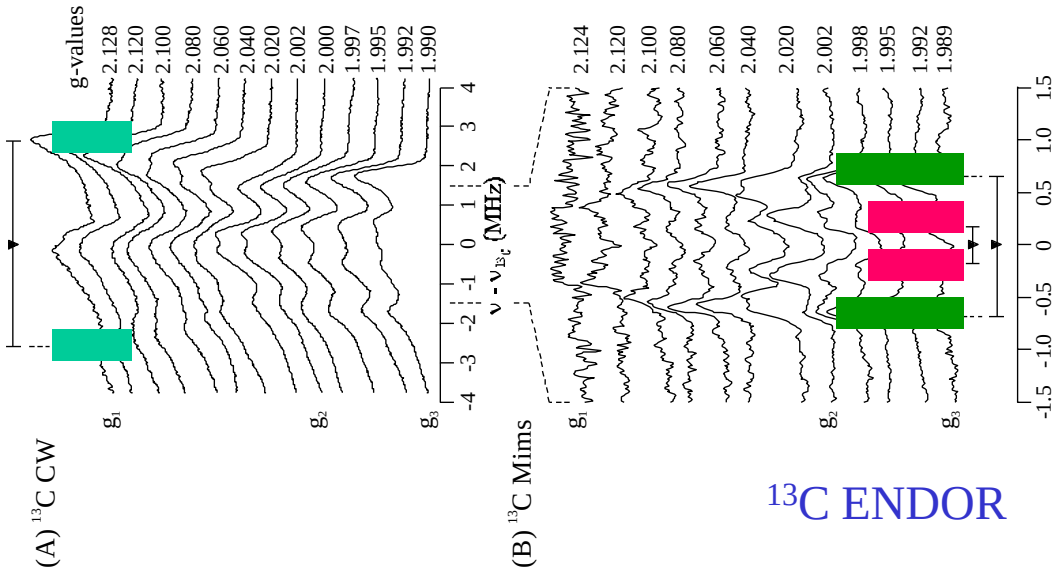

^{13}C ENDOR

Applications – Metalloenzymes (N_2ase)

Nitrogenase

$[Fe_7MoS_9X]$
FeMo-cofactor

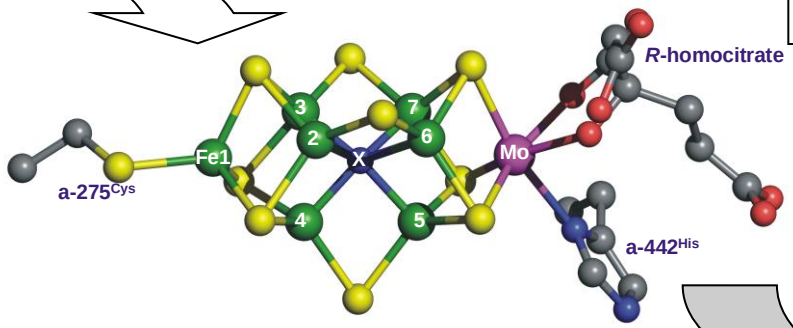

HO-CH$_2$-C≡C-H
(Propargyl Alcohol)

HO-CH$_2$-CH=CH$_2$
(Allyl Alcohol)

2e$^-$ + 2H$^+$

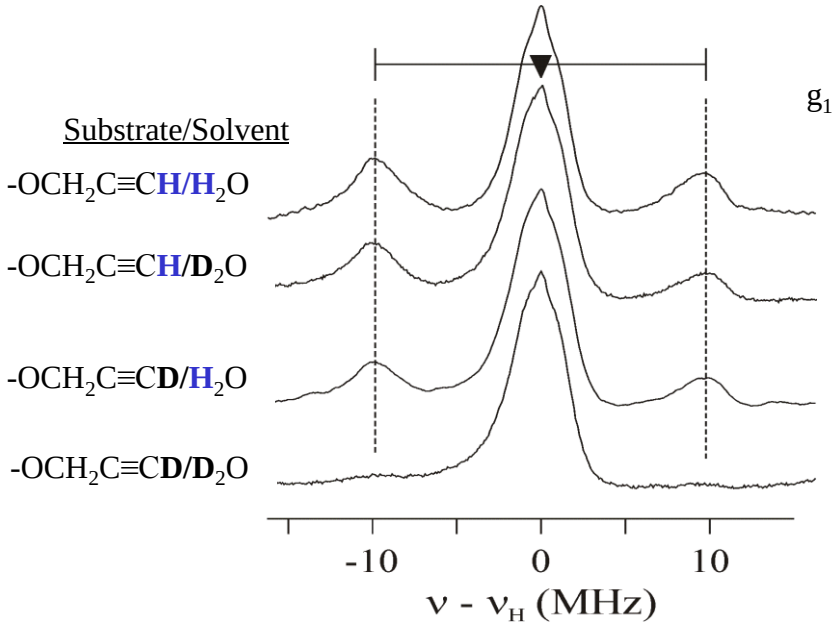

^{1}H ENDOR

Applications – Metalloenzymes (N_2ase)

Nitrogenase

$[Fe_7MoS_9X]$
FeMo-cofactor

HO-CH$_2$-C≡C-H
(Propargyl Alcohol)

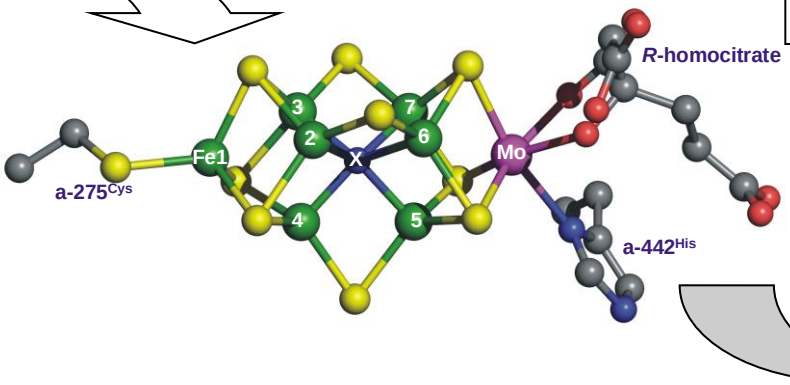

HO-CH$_2$-CH=CH$_2$
(Allyl Alcohol)

2e$^-$ + 2H$^+$

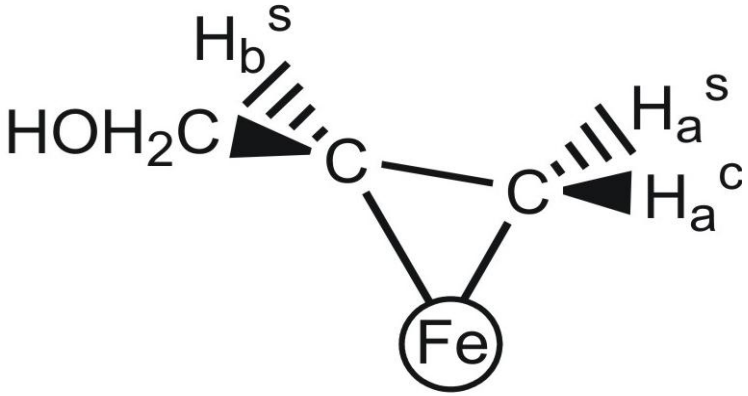

JACS, 126, 2004, 9563-9569

Applications – Metalloenzymes (N_2ase)

Nitrogenase

$[Fe_7MoS_9X]$
FeMo-cofactor

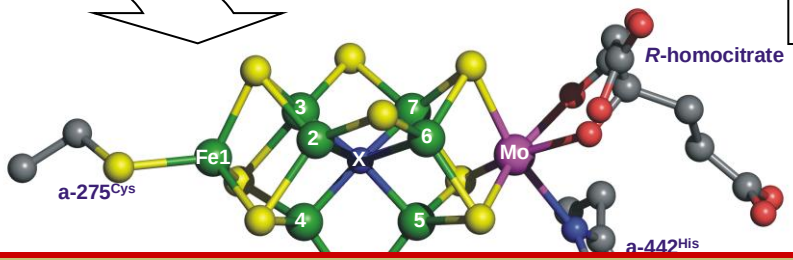

HO-CH$_2$-C≡C-H
(Propargyl Alcohol)

HO-CH$_2$-CH=CH$_2$
(Allyl Alcohol)

+ 2H$^+$

Enzyme mechanism
3D Structure
Metal-ion: coordination Geometry
valence
identification
Protein dynamics
Electronic and magnetic properties

Applications – Metalloenzymes (H_2ase)

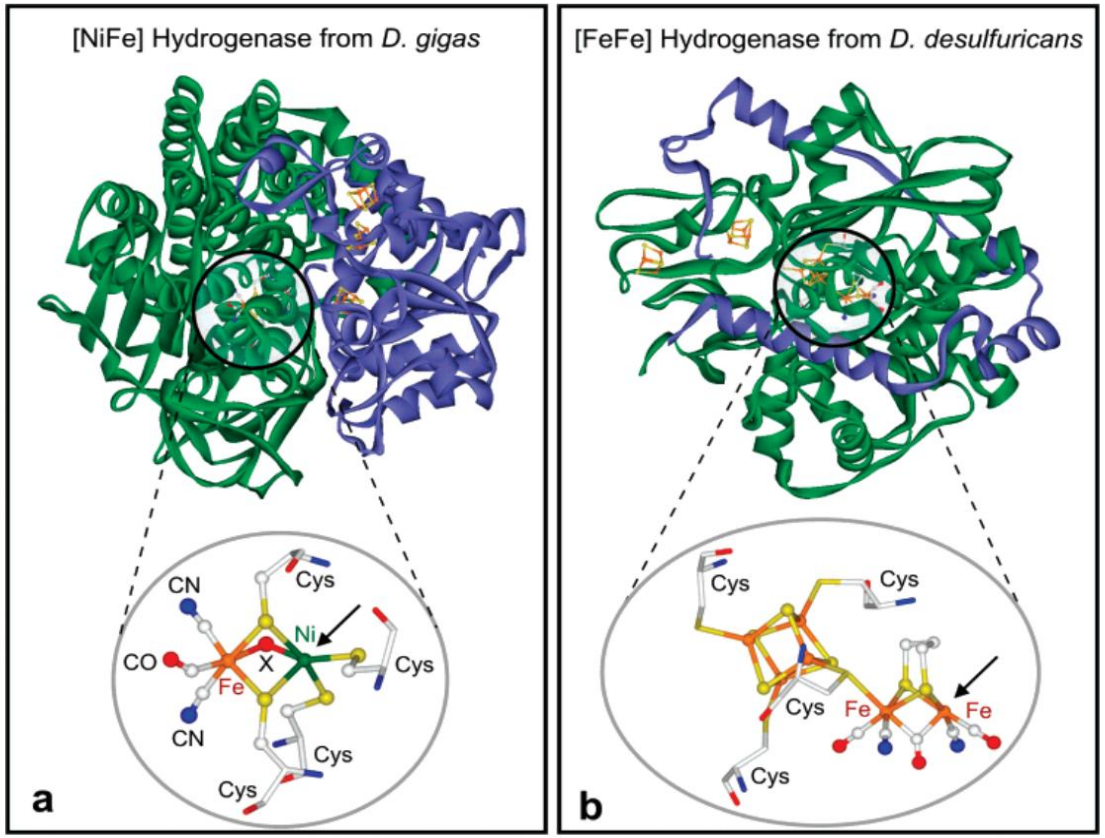

Figure 1. (a) Structure of [NiFe] hydrogenase from *D. gigas* (PDB 1FRV) from ref 63 detailing the two protein subunits (small, blue; large, green), the electron-transfer chain with three Fe−S centers in the small subunit, and the active site in the large subunit. The structure of the active site is shown enlarged at the bottom (see text). The arrow indicates the sixth coordination site at Ni which is found to be unoccupied. The enzyme resided mainly in the unready state. (b) Structure of [FeFe] hydrogenase from *D. desulfuricans* (PDB 1HFE) from ref 61, detailing the two protein subunits (small, blue; large, green). The H-cluster (hydrogen-activating cluster) and the two additional [4Fe−4S] clusters are all located in the large subunit. The molecular structure of the H-cluster with the cubane $[4Fe-4S]_H$ and the dinuclear $[2Fe]_H$ subclusters is shown enlarged at the bottom. The arrow indicates the free coordination site at the distal iron Fe_d found in ref 61.

Applications – Metalloenzymes (H_2ase)

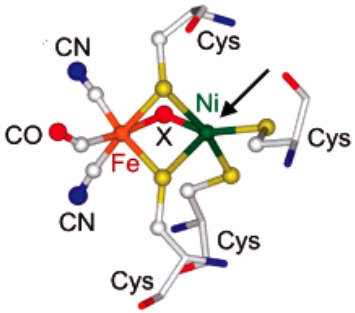

[NiFe]-hydrogenase

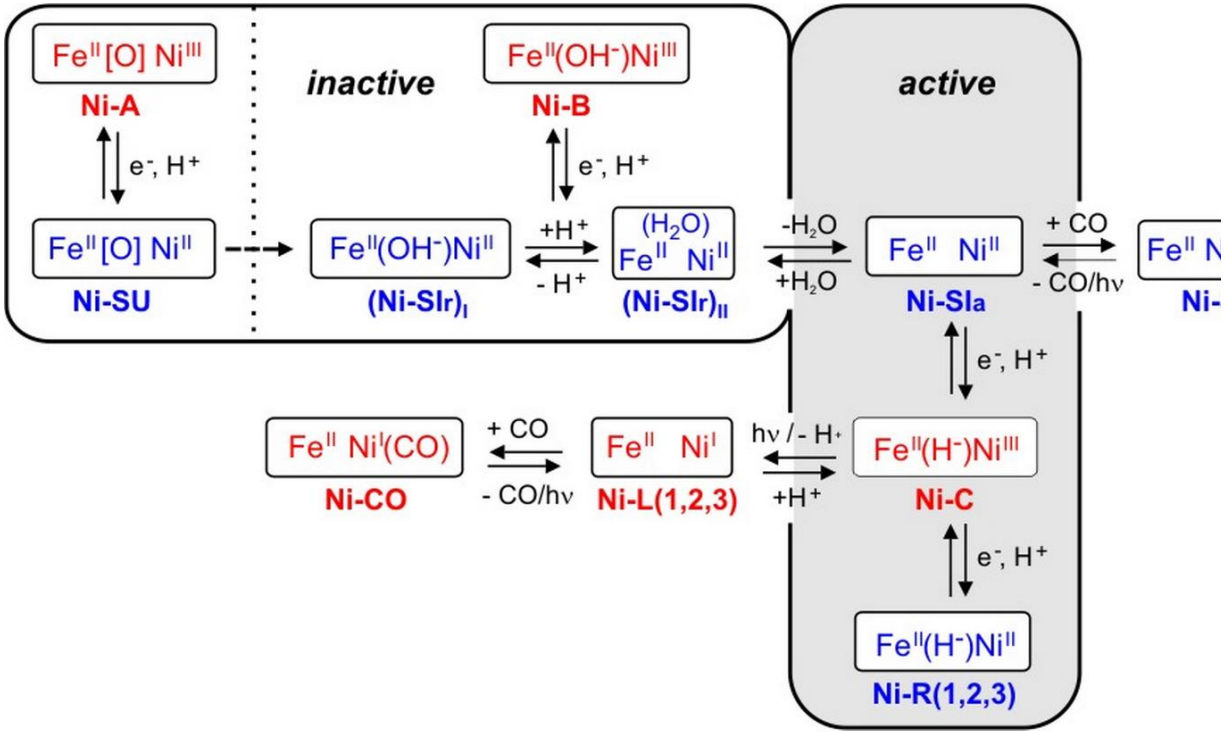

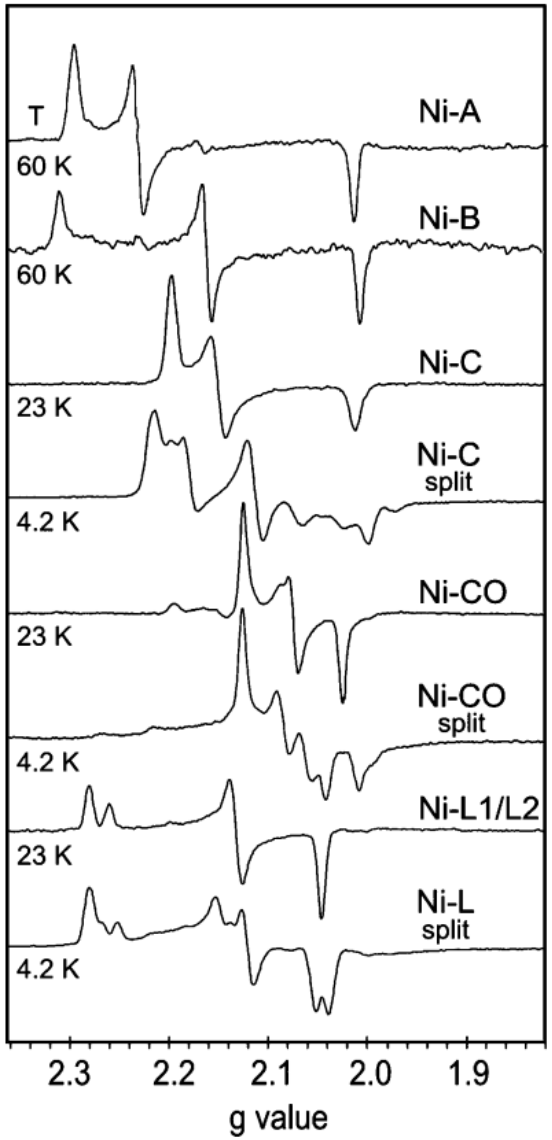

Applications – Metalloenzymes (H_2ase)

[NiFe]-hydrogenase

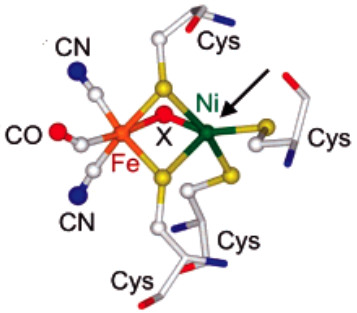

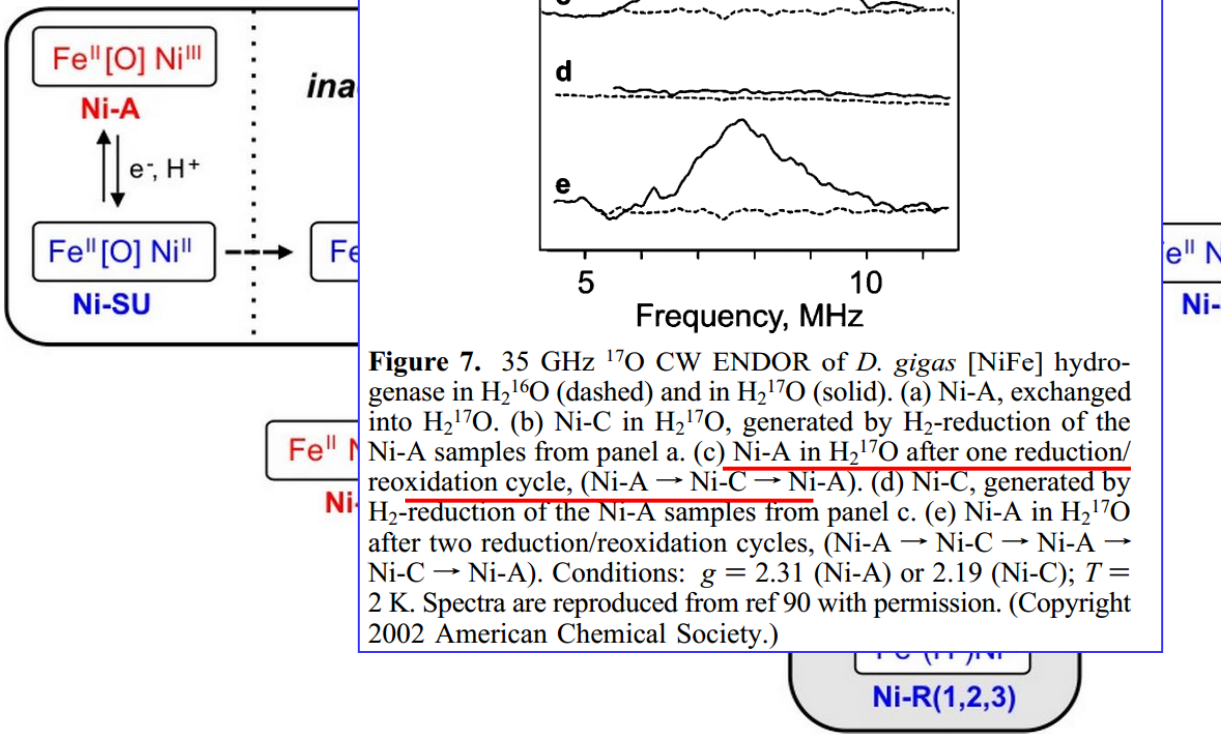

Figure 7. 35 GHz ^{17}O CW ENDOR of *D. gigas* [NiFe] hydrogenase in $H_2{}^{16}O$ (dashed) and in $H_2{}^{17}O$ (solid). (a) Ni-A, exchanged into $H_2{}^{17}O$. (b) Ni-C in $H_2{}^{17}O$, generated by H_2-reduction of the Ni-A samples from panel a. (c) Ni-A in $H_2{}^{17}O$ after one reduction/reoxidation cycle, (Ni-A → Ni-C → Ni-A). (d) Ni-C, generated by H_2-reduction of the Ni-A samples from panel c. (e) Ni-A in $H_2{}^{17}O$ after two reduction/reoxidation cycles, (Ni-A → Ni-C → Ni-A → Ni-C → Ni-A). Conditions: $g = 2.31$ (Ni-A) or 2.19 (Ni-C); $T =$ 2 K. Spectra are reproduced from ref 90 with permission. (Copyright 2002 American Chemical Society.)

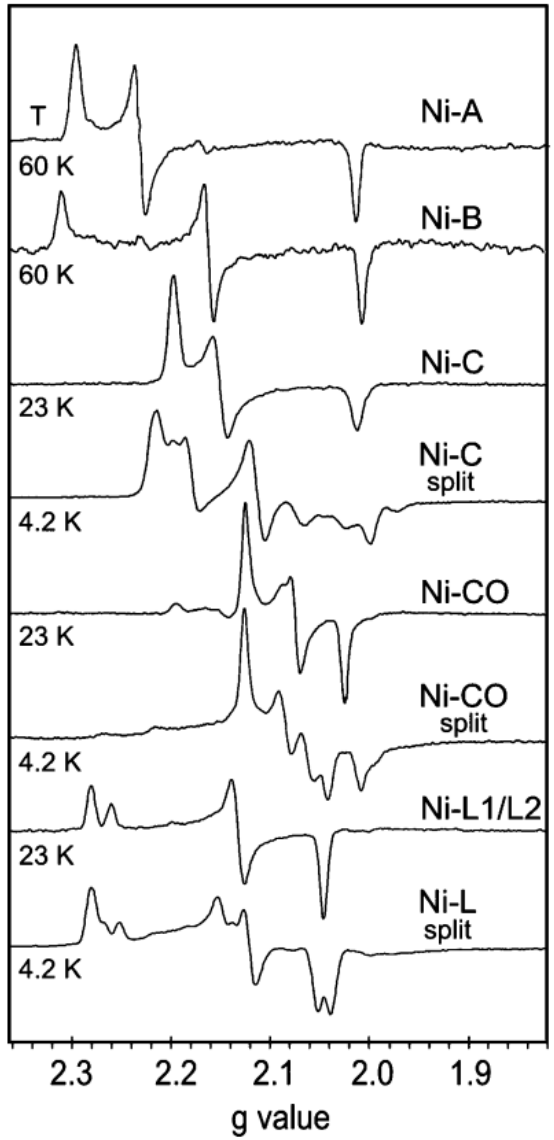

Applications – Metalloenzymes (H_2ase)

[NiFe]-hydrogenase

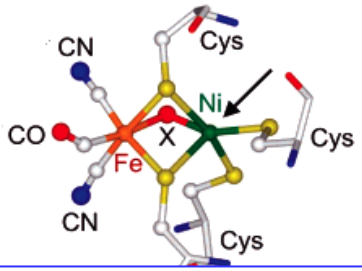

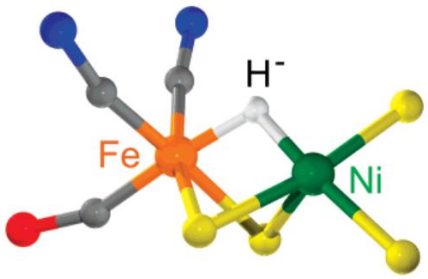

r_{FeH} = 1.72 Å r_{NiH} = 1.61 Å

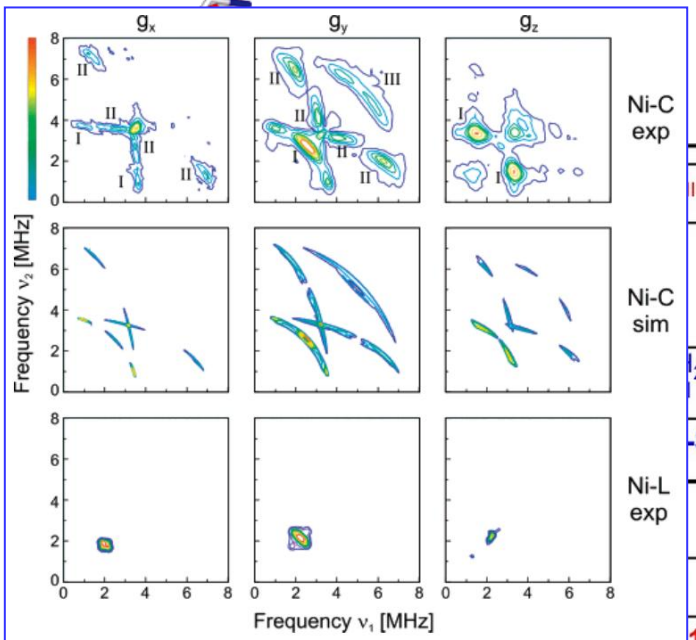

Figure 8. Top: orientation selected HYSCORE spectra at X-band recorded at the three canonical orientations (g_x, g_y, g_z) for the Ni-C state in the regulatory hydrogenase of *R. eutropha* in ^2H_2O activated with $^2H_2$. All observed ridges in the spectrum stem from the hydride bridging ligand ($^2H^-$), located in the *xy* plane of the square pyramid (cf. Scheme 3). Middle: simulations of the experimental spectra. Bottom: HYSCORE spectra of the Ni-L1 state. As is seen in the spectra, the strong couplings have disappeared, indicating a photodissociation of the hydride bridge upon illumination. Data are adapted from ref 93.

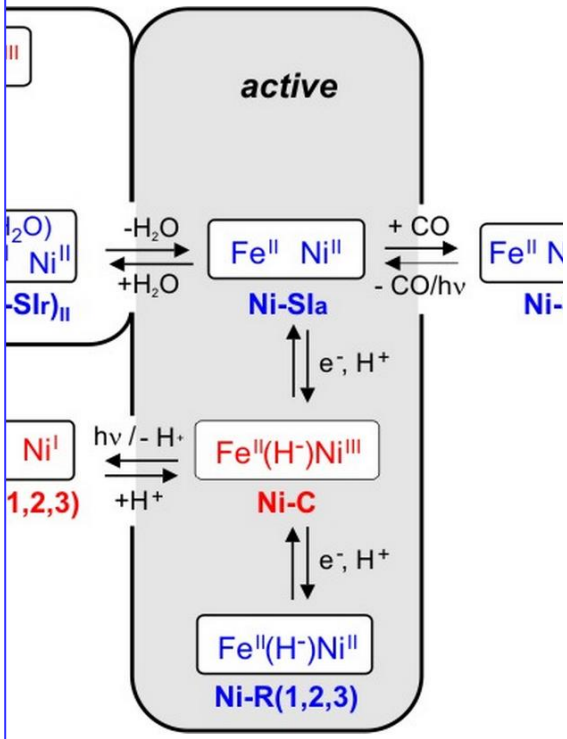

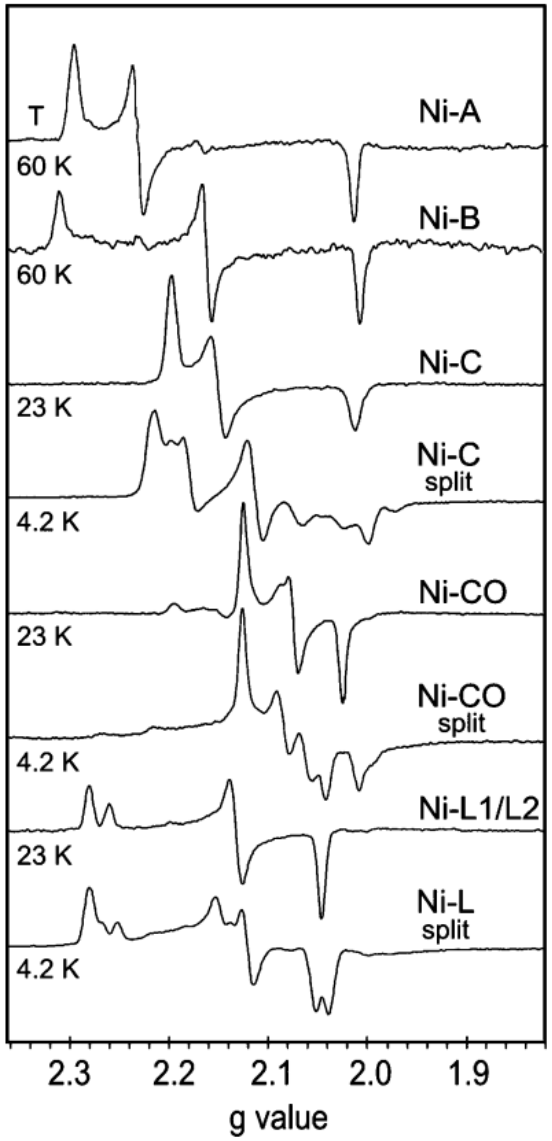

Applications – Metalloenzymes (H_2ase)

Formate dehydrogenase

W–FDH

Mo(V)–FDH

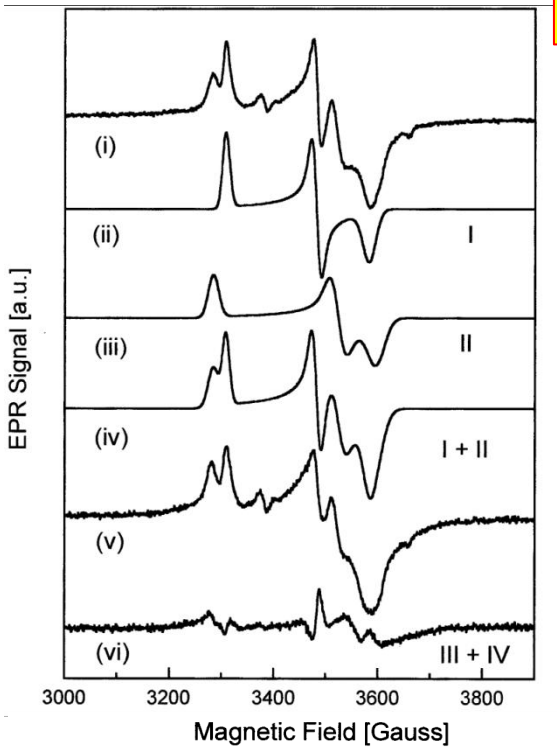

Fig. 3 EPR spectra of a partially formate-reduced state of *D. gigas* FDH at 20 K (*i*) and at 10 K (*v*), together with the spectral simulation of signal I (*ii*), signal II (*iii*), and the sum of signals I and II in a ratio 1:1 (*iv*). Also shown is the difference spectrum between 20 K and 10 K (*vi*). Experimental conditions were: (*i*) temperature, 20 K; microwave power, 0.2 mW; modulation amplitude, 4 G_{pp}; microwave frequency, 9.49 GHz; (*ii*) as in (*i*) except temperature, 10 K; and microwave power, 0.2 mW. Simulations were performed with the parameters: [g_1=1.892 (30), g_2=1.947 (15), g_3=2.049 (14)] (*ii*), and [g_1=1.885 (32), g_2=1.924 (26), g_3=2.064 (20)] (*iii*) (line width between parentheses). Signal (*i*) was scaled to the experimental conditions of signal (*v*) in order to obtain signal (*vi*)

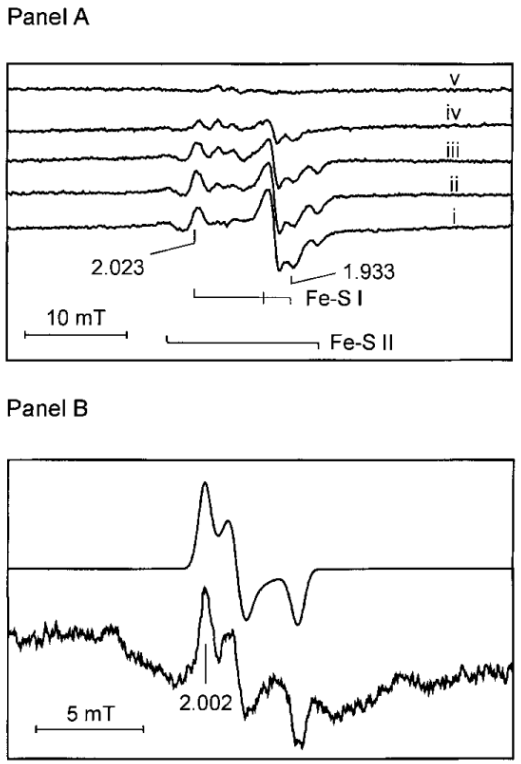

FIG. 2. EPR spectra of *Methylobacterium* sp. RXM FDH. Panel A - X-Band EPR spectra of the FDH dithionite reduced. Temperature dependence of the spectra i)10K, ii)15K, iii)25K, iv)45K and v)100K. Panel B - Detail of the X-band EPR spectrum of Mo(V) species at 100K. A simulation of the spectral data is included (g-values (linewidth, mT):2.002 (1.14), 1.987 (1.32), 1.959 (1.22)). Experimental conditions: Modulation Amplitude, 1.0 mT; Microwave frequency, 9.49 GHz; Microwave Power, 2.35 mW.

Applications – Trapping Free Radicals

Spin-trapping

Species: superoxide, hydroxyl, alkyl, NO

Spin-trapping agents: DMPO, PBN, DEPMPO, Fe-DTCs

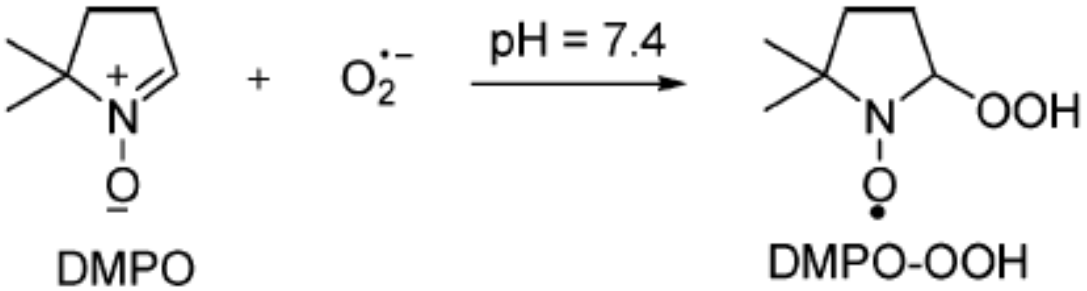

DMPO DMPO-OOH

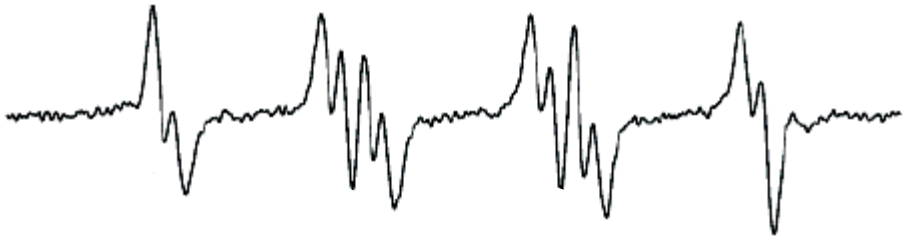

Oxidative stress
Cell signaling
Photoreaction
:
:

A_N = 1.42 mT, A_H^{β}, = 1.134 mT, and A_H^{γ} = 0.125 mT.

Effect of Hydrated Electron (e_{aq}^-)

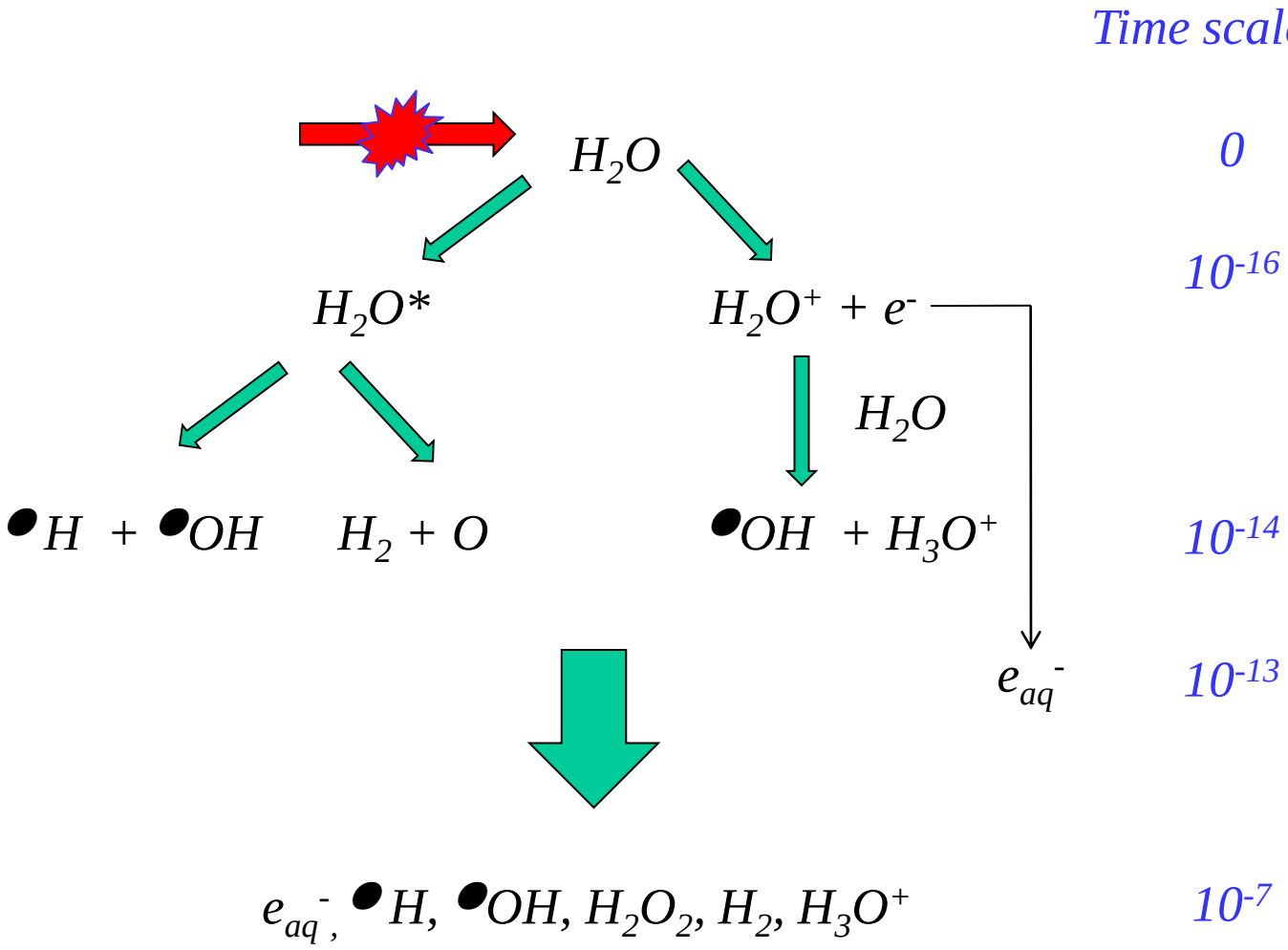

Spin Trapping

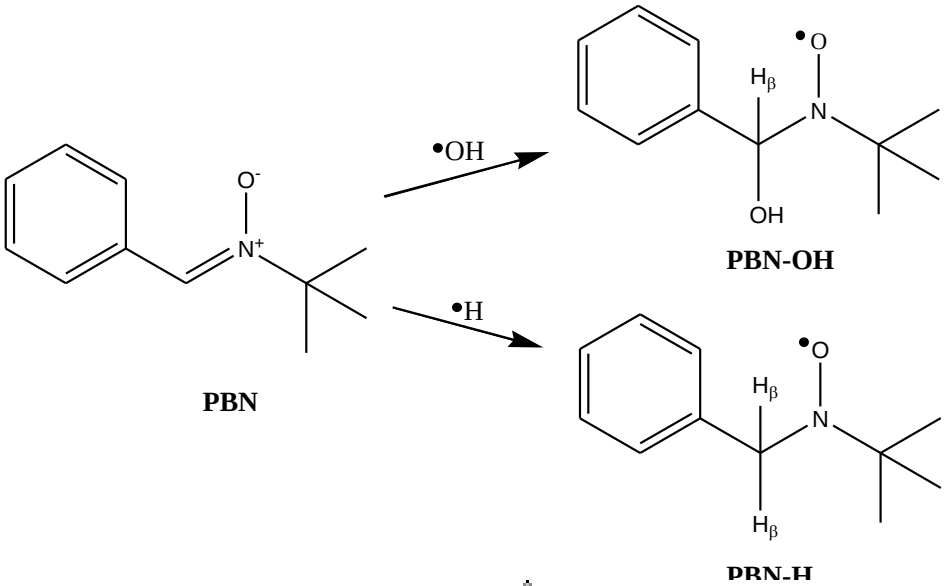

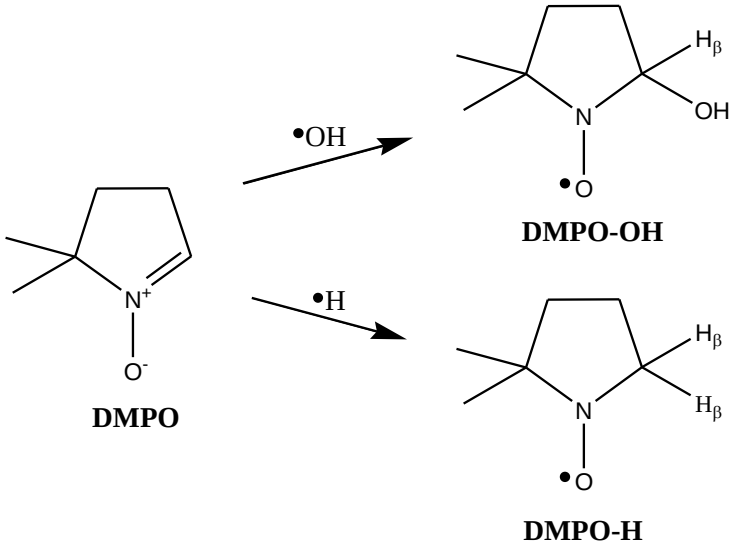

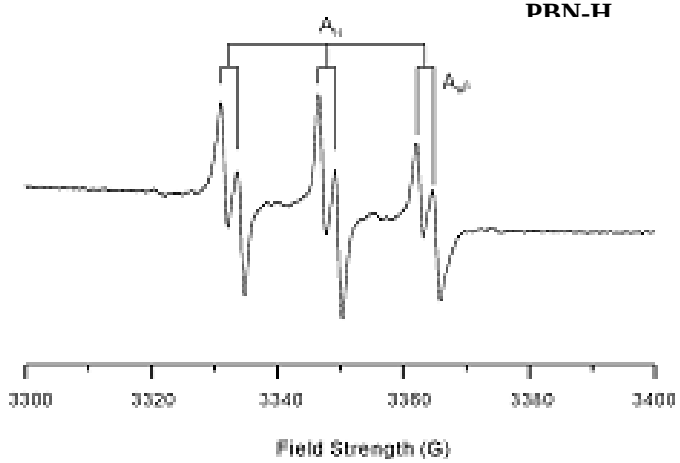

EPR of PBN-OH

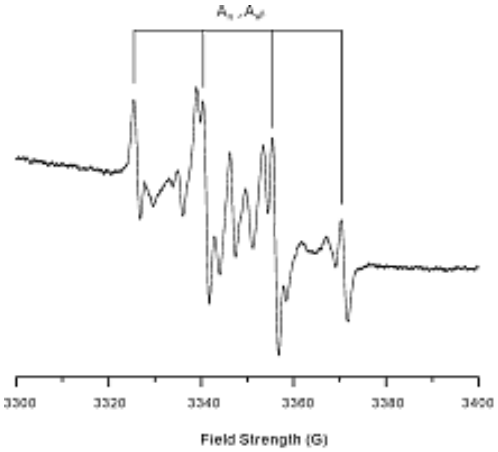

EPR of DMPO-OH

Spin Trapping

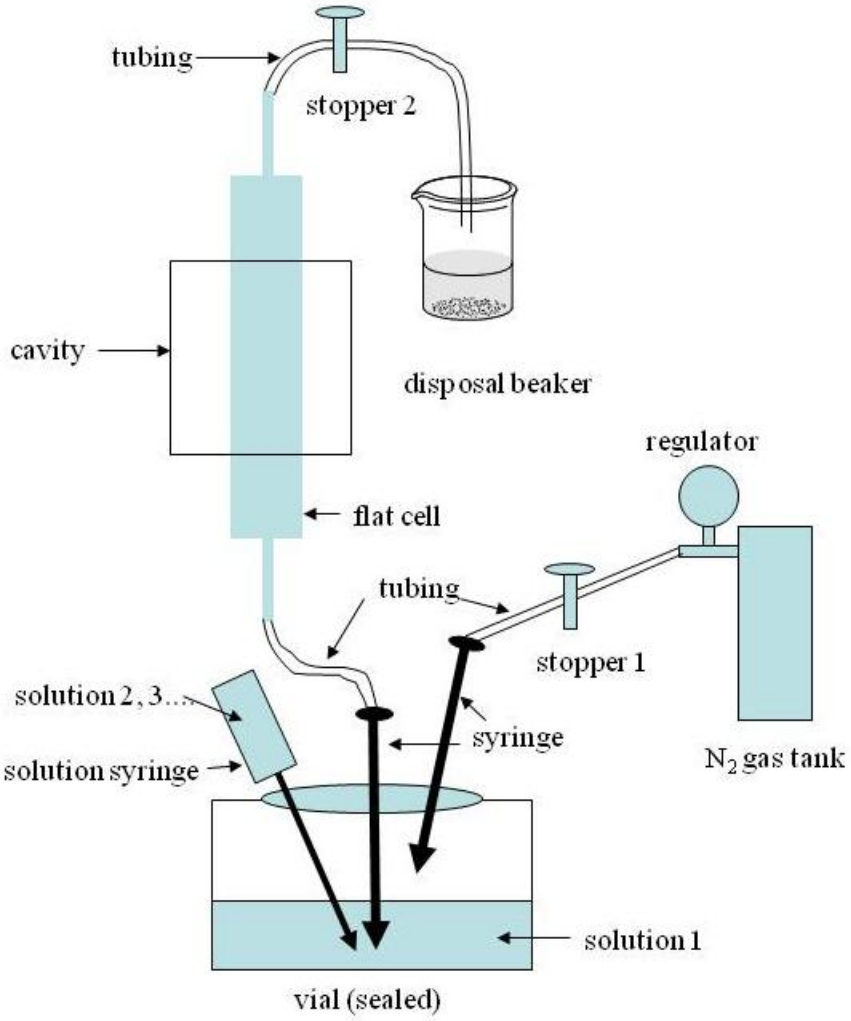

Detection of `H Generated by e-Beam

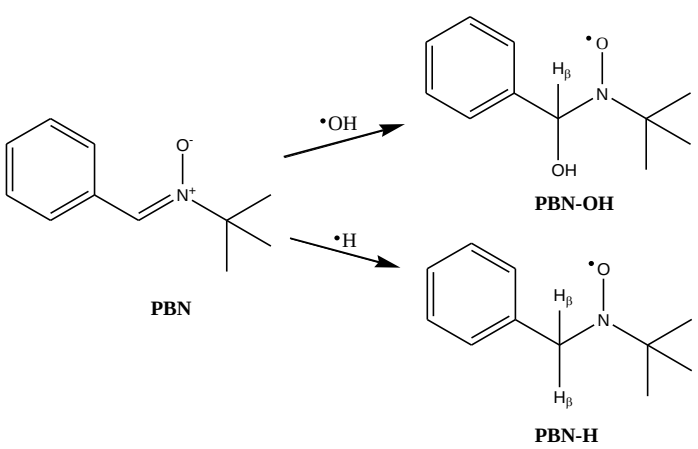

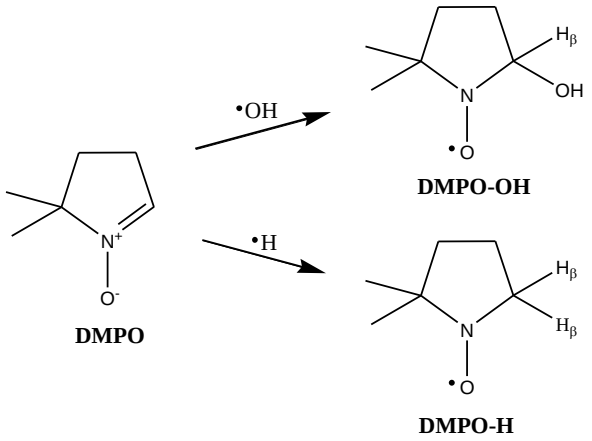

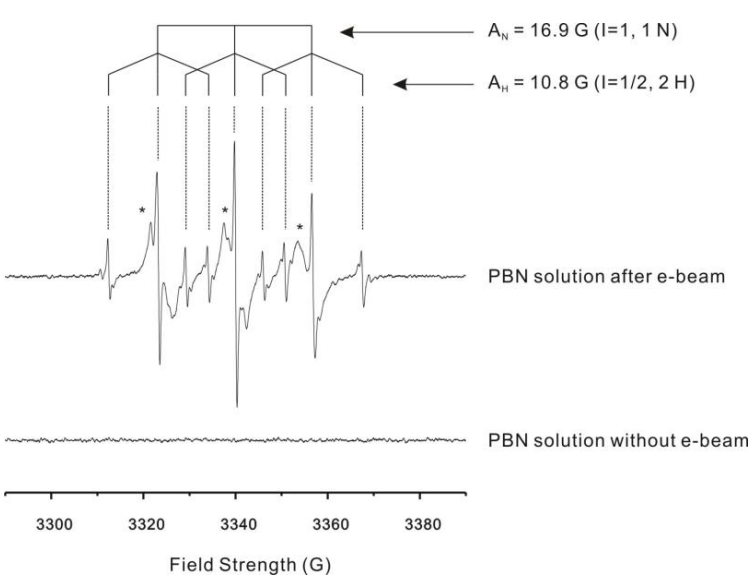

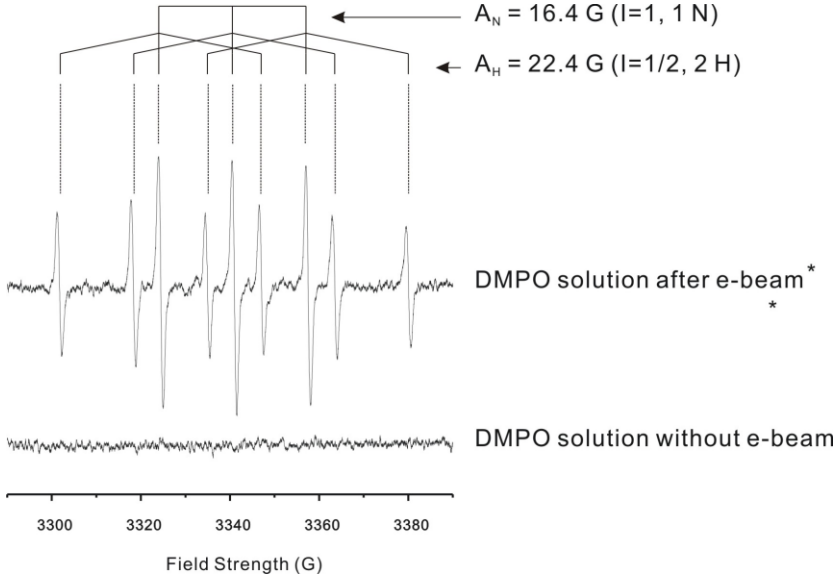

Applications – Distance measurement

Spin-labelling

Species: TEMPO….

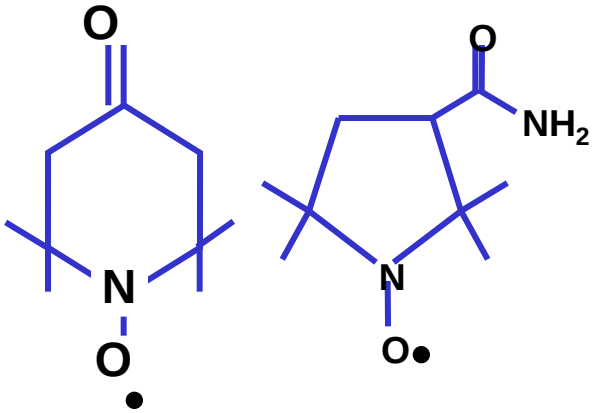

Membrane protein
::

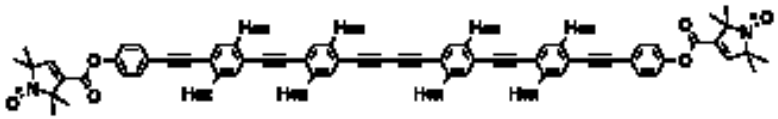

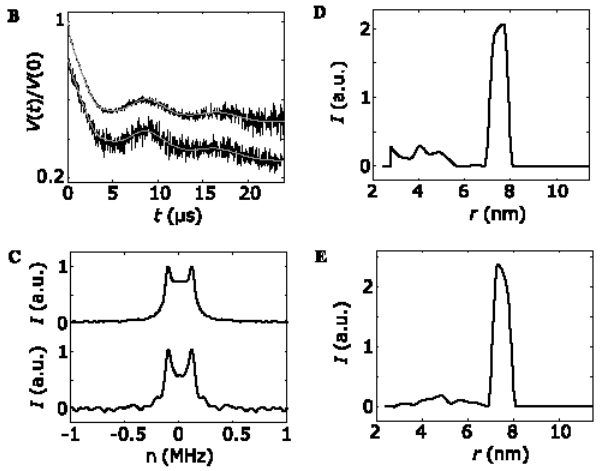

JMR, 169, 2004, 1-12

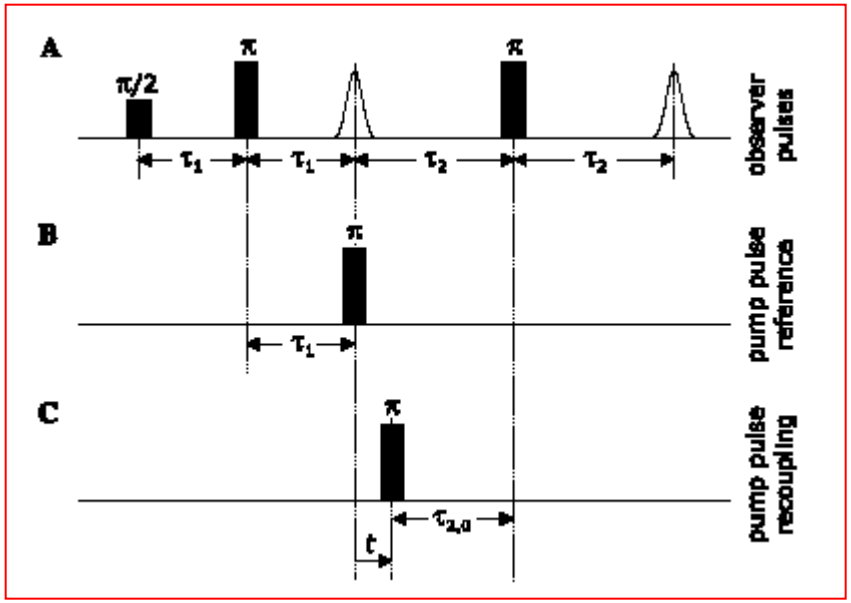

DEER (Double electron electron resonance)

Applications – Radiation Dosimetry

Alanine dosimetry

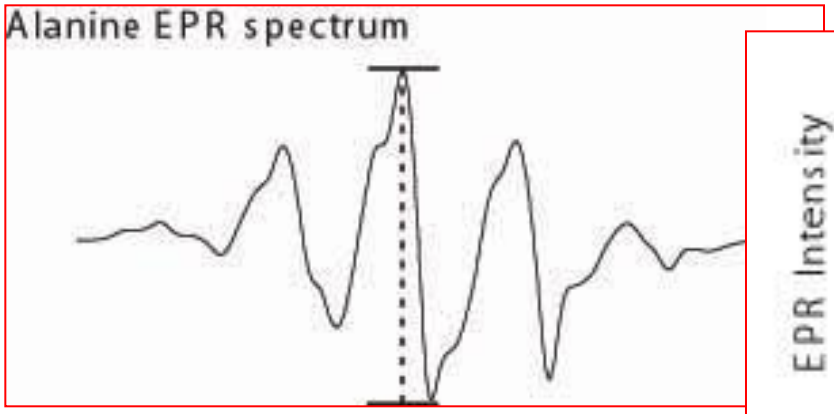

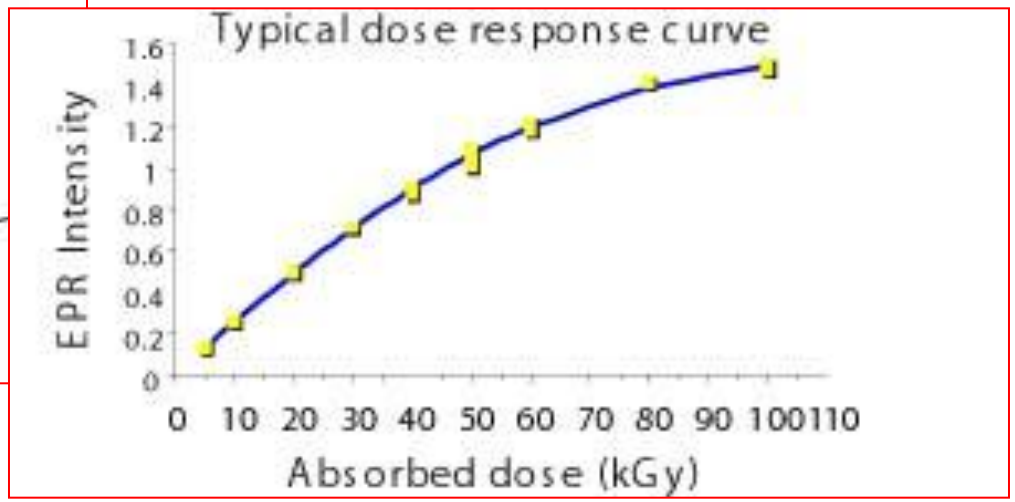

Alanine forms a very stable free radical when subjected to ionizing radiation, such as gamma-ray, e-beam, and X-ray.

Applications – EPR Imaging

Oximetry

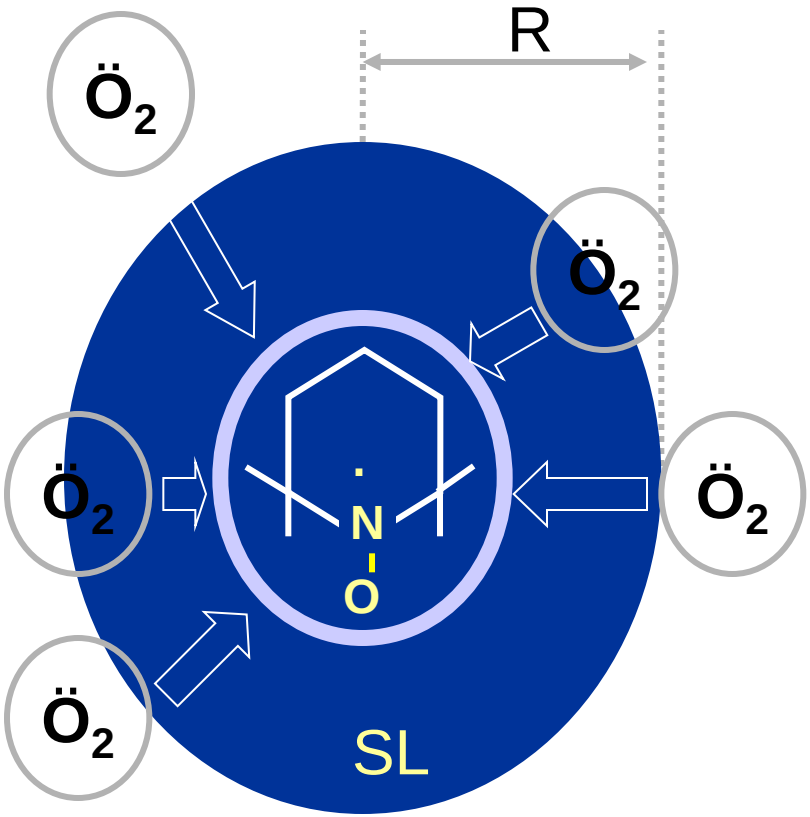

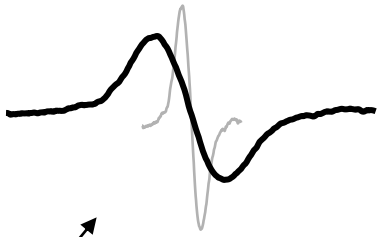

Line-broadening

Bimolecular collision between SL and oxygen leads to Heisenberg spin exchange

* Direct EPR detection of paramagnetic O_2 in fluid is not possible.

Applications – EPR Imaging

Oximetry

Mapping of arterio-venous oxygenation in a rat tail, *in vivo*

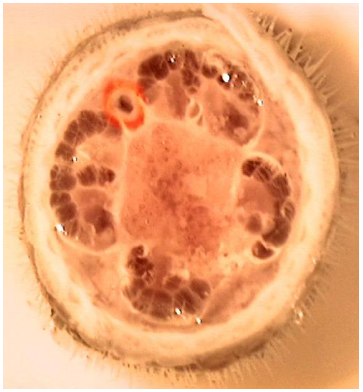

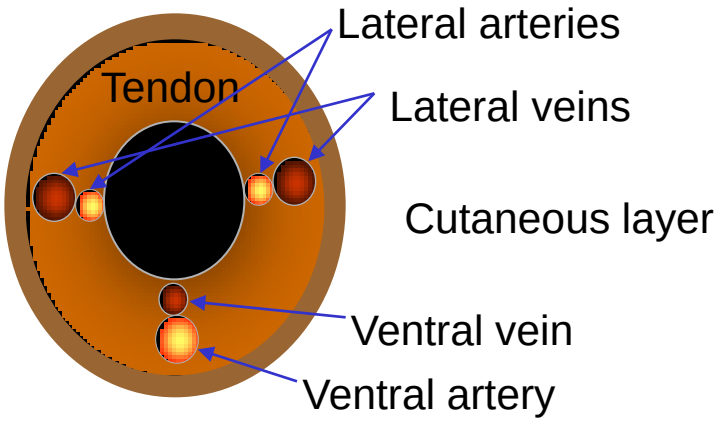

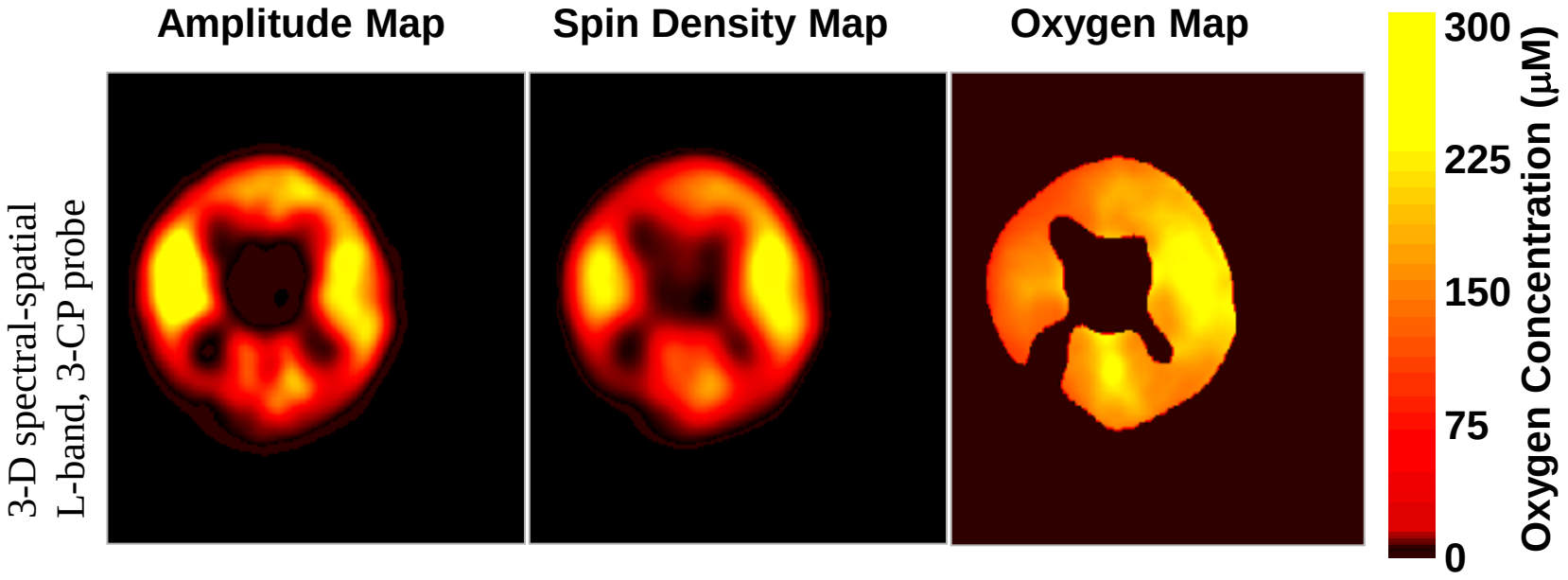

Sendhil Velan, S., Spencer, R.G.S., Zweier, J. L. & Kuppusamy P. Magn. Reson. Med. 43, 804-809 (2000)

Applications – Minerals

Available online at www.sciencedirect.com
SCIENCE DIRECT
ELSEVIER
Spectrochimica Acta Part A 60 (2

EPR, optical, infrared and Raman spe

N.O. Gopal, K.V. Naras
Department of Physics, Sri Venkateswara

Received 3 October 2003; accept

1. Introduction

Natural minerals have been
sorption spectroscopic investiga
chemical compositions. Genera
sition ions such as Fe^{3+}, Cr^{3+} a
natural minerals. Electron para
optical absorption, infrared an
minerals provide useful inform
istry of transition metal ions
erals [1–6]. For most transitio
that are present only in small a
site), EPR is the most powerful
ous information about the vale
EPR studies have been perfor
[7–12].

5. Conclusions

1. The preliminary chemical analysis of the Actinolite mineral reveals the presence of iron, manganese, cobalt, nickel and chromium.
2. The EPR spectrum exhibits two resonance signals at $g = 2.0$ and 4.3. The well resolved hyperfine pattern at $g = 2.0$ is attributed to Mn^{2+} ions, whereas the resonance signal at $g = 4.3$ is attributed to Fe^{3+} ions.
3. The magnitude of hyperfine splitting constant A indicates that the bonding between Mn^{2+} and its surrounding ligands is moderately ionic.
4. The temperature variation EPR studies reveal that the variation of number of spins with temperature is in accordance with Boltzmann law. The activation energy has been calculated from $\log N$ versus $1/T$ graph and is found to be 0.0082 eV.
5. The variation of susceptibility with temperature is in accordance with the Curie's law. Form the $1/\chi$ versus temperature graph, the Curie constant and the Curie temperature have been evaluated and are found to be 0.175 emu/mol and 77 K, respectively.
6. The optical absorption spectrum reveals the presence of iron both in trivalent and divalent states and also an intervalence charge transfer band ($Fe^{2+}-Fe^{3+}$).
7. The optical band gap energy has been calculated from the ultraviolet absorption edge of the optical absorption spectrum and is found to be 3.14 eV.
8. The infrared spectrum reveals the presence of metal ion hydroxyl vibrations. The Raman spectrum exhibits bands characteristic of the Si–O–Si stretching and Mg–OH translation modes.

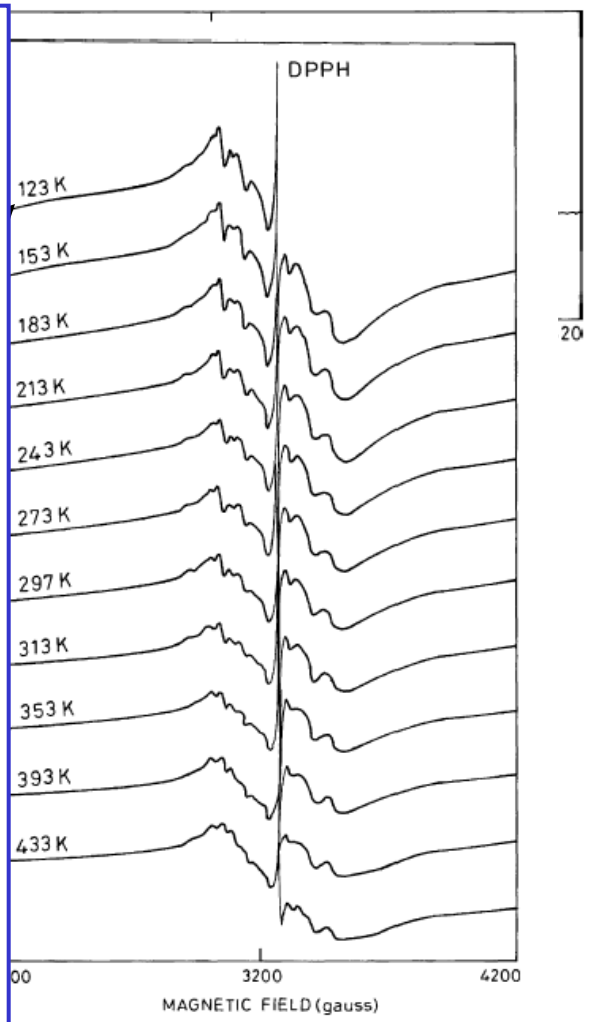

The EPR spectra of polycrystalline Actinolite mineral observed at temperatures for the resonance signal at $g = 2.0$.

Applications – Minerals

Radiation Effects & Defects in Solids
March 2004, Vol. 159, pp. 141–147

Taylor & Francis

OPTICAL AND EPR INVESTIGATIONS ON SMITHSONITE MINERALS

B. J. REDDY[a], J. YAMAUCHI[b], R. V. S. S. N. RAVIKUMAR[c,*]
A. V. CHANDRASEKHAR[d] and M. VENKATARAMANAIAH[e]

[a]*Department of Physics, S.V. University, Tirupati 517 502, India;* [b]*Graduate School of Human and Environmental Studies, Kyoto University, Nihonmatsu, Yoshida, Kyoto 606-8501, Japan;* [c]*Department of Advanced Materials Sciences and Engineering, Yamaguchi University, Tokiwadai, Ube 755-8611, Japan;* [d]*Department of Physics, S.P.W. Junior College, Tirupati 517 502, India;* [e]*Department of Physics, S.V. Degree College, Cuddapah 516 003, India*

(Received 1 September 2003; In final form 20 January 2004)

1 INTRODUCTION

The mineral smithsonite has the chemical formula $ZnCO_3$. It belongs to the trigonal crystal system with the $D_{3d}^6 - R\bar{3}c$ group. It is isostructural with the calcite type with the unit cell parameters $a = 0.466$ nm, $c = 1.498$ nm, $\alpha = 1.625$, $\gamma = 1.850$ and $Z = 6$ [1]. The Zn(II) ions are accordingly in the octahedral coordination of oxygen ions, belonging to the apexes of the triangular anions $[CO_3]^{2-}$ as in the analogous crystals [2]. Transition metal ions such as Cu(II), Mn(II), Fe(II), Co(II) may easily substitute Zn(II). Smithsonite is used as bio-mineral, because it is very effective to eliminate toxins from the body [3] and it is also used as flotation mineral [4]. It has wide applications in the field of microwaves [5]. The present investigations are aimed at having a comprehensive view of the effect of transition metal impurities in the mineral by optical absorption and EPR studies. Two samples of the naturally occurring mineral smithsonite, one from Graphic Mines, Kelly, New Mexico, USA (Sample No. BM 81038) and another from the Westernhope Mine, Weardale, Durham County, UK (Sample No. RV 5/1080) are chosen for the study.

5 CONCLUSIONS

From the optical absorption spectra, the main impurity present in the two samples is attributed to a Cu(II) ion in the tetragonally distorted octahedral site suggesting the isomorphous replacement of Cu(II) for Zn(II) in smithsonite. EPR spectra of Cu(II) in these samples support the same conclusion. Further EPR spectra of the samples indicate the presence of Mn(II) in traces. However, the concentration of Mn(II) is too small to exhibit any optical absorption bands.

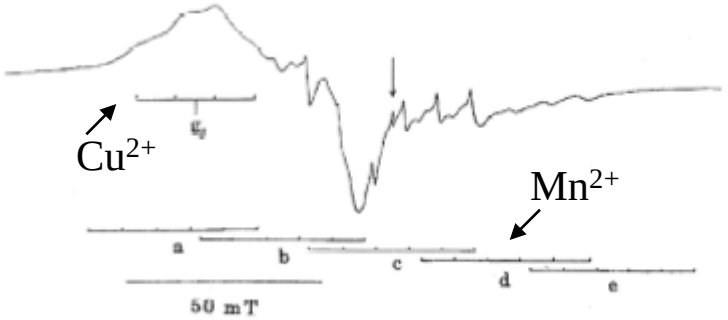

FIGURE 3 EPR spectrum of the USA sample at room temperature. The arrow indicates DPPH signal as a standard. The multiple transitions are designated by a–e.

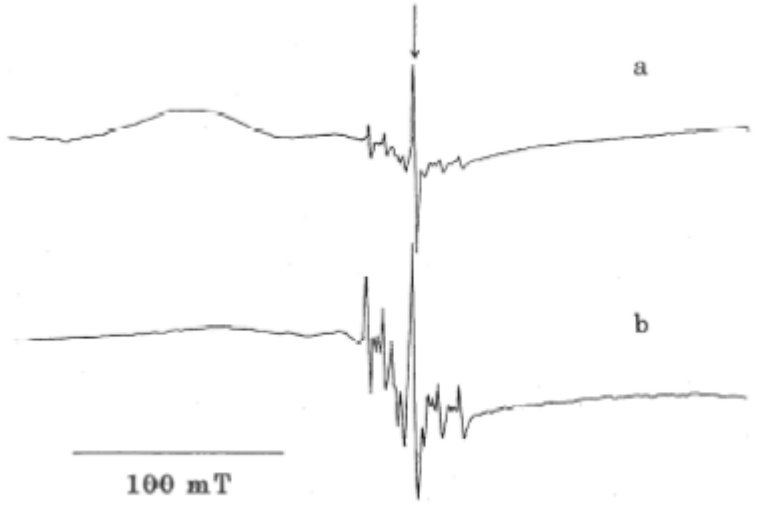

FIGURE 4 EPR spectra of the UK sample at room temperature (a) and 77K (b). The arrow indicates the DPPH signal as a standard.

Applications – Minerals

Electron Paramagnetic Resonance of Rhyolite and γ-Irradiated Trona Minerals

F. Köksal, R. Köseoğlu[a], and E. Başaran[b]

Physics Department, Faculty of Arts and Sciences, Ondokuz Mayıs University, Samsun, Turkey
[a] Physics Department, Faculty of Arts and Sciences, Niğde University, Niğde, Turkey
[b] Physics Department, Faculty of Arts and Sciences, Gebze HighTechnology Institute, İstanbul, Turkey

Reprint requests to Prof. F. K.; Fax: +90-362-457 6081; E-mail: koksalf@omu.edu.tr

Z. Naturforsch. **58a**, 293 – 298 (2003); received January 2, 2003

1. Introduction

Various kinds of stones, geothermal samples and lava systems have been investigated by electron paramagnetic resonance (EPR) [1, 2]. The samples studied were either natural state or in their γ-irradiated [3 – 14]. These studies revealed the presence of various kinds of sulphur oxy and carboxy radicals in these substances. Around the Erciyes mountain in inner Anatolia, and its neighbouring province Nevşehir, the mostly encountered remnants are various kinds of stones or tuffs. One of these stones is rhyolite, locally named Yellow Stone of Nevşehir. It was investigated in this study. We expected to detect paramagnetic centers in rhyolite due to the thermal effects of the close mountain Erciyes, which was active earlier. Due to it is use in house constraction, this stone is important in that region. To our knowledge there exists no investigation of this mineral with EPR. Also trona, which is widely used in soda and glass production, seemed interesting to study with EPR. Rhyolite and trona were first studied in their natural states, and then their γ-irradiated states were considered. Before γ-irradiation the results indicated the

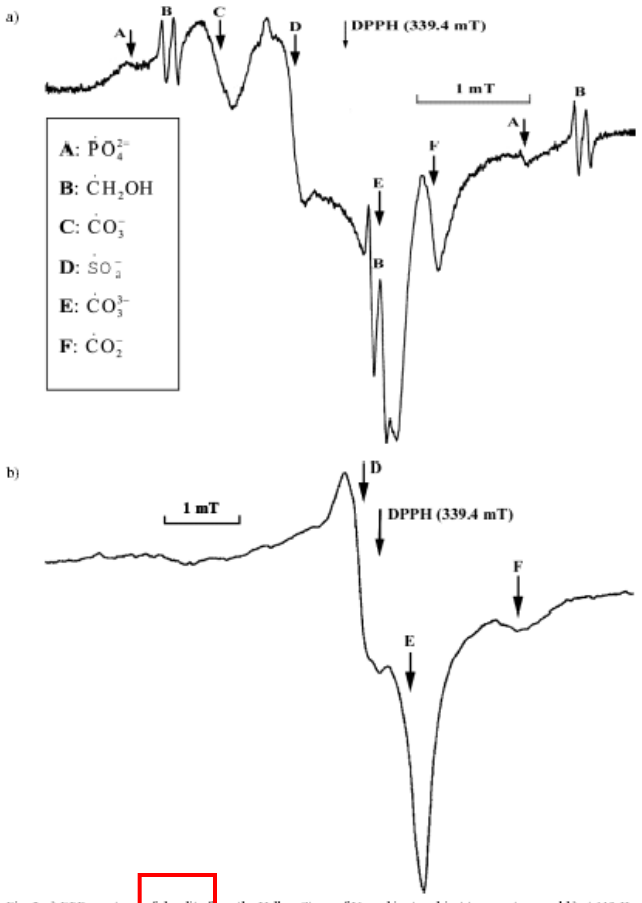

Fig. 2. a) EPR spectrum of rhyolite from the Yellow Stone of Nevşehir at ambient temperature, and b) at 113 K.

Applications – Minerals

Electron Paramagnetic Resonance of Rhyolite and γ-Irradiated Trona Minerals

F. Köksal, R. Köseoğlu[a], and E. Başaran[b]

Physics Department, Faculty of Arts and Sciences, Ondokuz Mayıs University, Samsun, Turkey
[a] Physics Department, Faculty of Arts and Sciences, Niğde University, Niğde, Turkey
[b] Physics Department, Faculty of Arts and Sciences, Gebze HighTechnology Institute, İstanbul, Turkey

Reprint requests to Prof. F. K.; Fax: +90-362-457 6081; E-mail: koksalf@omu.edu.tr

Z. Naturforsch. **58a**, 293 – 298 (2003); received January 2, 2003

1. Introduction

Various kinds of stones, geothermal samples and lava systems have been investigated by electron paramagnetic resonance (EPR) [1, 2]. The samples studied were either natural state or in their γ-irradiated [3 – 14]. These studies revealed the presence of various kinds of sulphur oxy and carboxy radicals in these substances. Around the Erciyes mountain in inner Anatolia, and its neighbouring province Nevşehir, the mostly encountered remnants are various kinds of stones or tuffs. One of these stones is rhyolite, locally named Yellow Stone of Nevşehir. It was investigated in this study. We expected to detect paramagnetic centers in rhyolite due to the thermal effects of the close mountain Erciyes, which was active earlier. Due to it is use in house constraction, this stone is important in that region. To our knowledge there exists no investigation of this mineral with EPR. Also trona, which is widely used in soda and glass production, seemed interesting to study with EPR. Rhyolite and trona were first studied in their natural states, and then their γ-irradiated states were considered. Before γ-irradiation the results indicated the

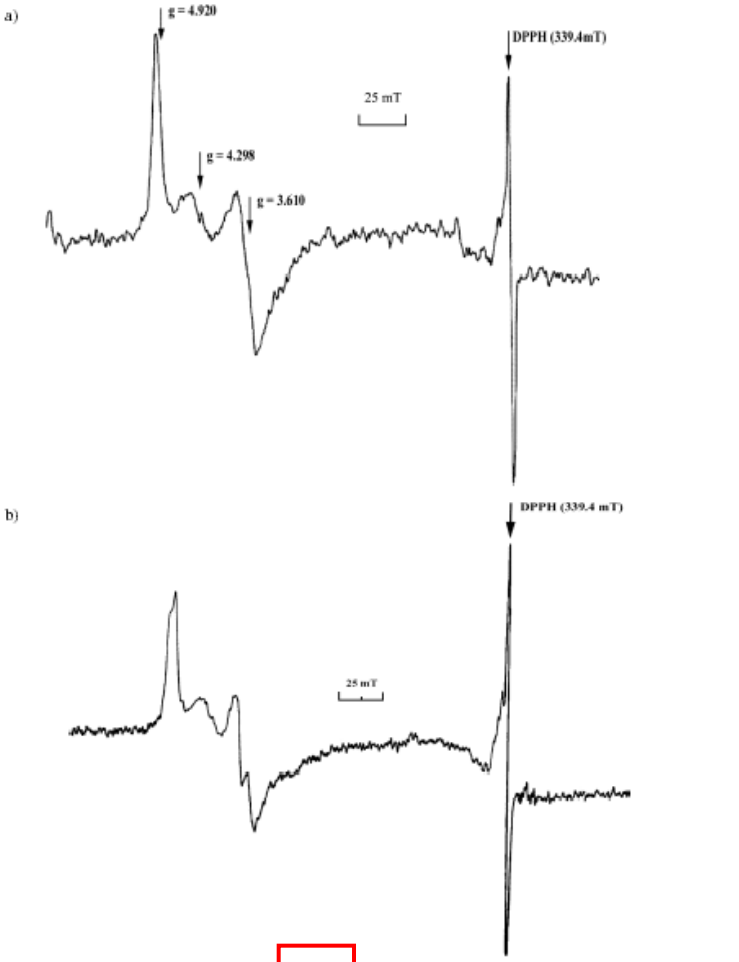

Fig. 3. a) Low field part of the EPR spectrum of rhyolite from the "Yellow Stone" at ambient temperature, and b) at 113 K.

Applications – Minerals

Electron Paramagnetic Resonance of Rhyolite and γ-Irradiated Trona Minerals

F. Köksal, R. Köseoğlu[a], and E. Başaran[b]

Physics Department, Faculty of Arts and Sciences, Ondokuz Mayıs University, Samsun, Turkey
[a] Physics Department, Faculty of Arts and Sciences, Niğde University, Niğde, Turkey
[b] Physics Department, Faculty of Arts and Sciences, Gebze HighTechnology Institute, İstanbul, Turkey

Reprint requests to Prof. F. K.; Fax: +90-362-457 6081; E-mail: koksalf@omu.edu.tr

Z. Naturforsch. **58a**, 293 – 298 (2003); received January 2, 2003

Rhyolite from the "Yellow Stone of Nevşehir" and γ-irradiated trona from the Ankara Mine have been investigated by electron paramagnetic resonance at ambient temperature and at 113 K. Rhyolite was examined by X-ray powder diffraction and found to consist mainly of SiO_2. Before γ-irradiation, the existing paramagnetic species in rhyolite were identified as $\dot{P}O_4^{2-}$, $\dot{C}H_2OH$, $\dot{C}O_3^-$, $\dot{S}O_2^-$, $\dot{C}O_3^{3-}$, and $\dot{C}O_2^-$ free radicals and Fe^{3+} at ambient temperature. At 113 K $\dot{S}O_2^-$, $\dot{C}O_3^{3-}$, and $\dot{C}O_2^-$ radicals and Fe^{3+} were observed. The γ-irradiation produced neither new species nor detectable effects on these free radicals. The disappearance of some of the radicals at 113 K is attributed to the freezing of their motions. Before γ-irradiation, the trona mineral shows only Mn^{2+} lines, but after γ-irradiation it indicated the inducement of $\dot{C}O_3^{3-}$ and $\dot{C}O_2^-$ radicals at ambient temperature, 113 K, in addition to the Mn^{2+} lines. The *g* and *a* values of the species were determined.

1. Introduction

Var
lava s
magn
were e
These
sulphu
Aroun
neigh
tered r
of thes
of Ne
pected
to the
which
straction, this stone is important in that region. To our knowledge there exists no investigation of this mineral with EPR. Also trona, which is widely used in soda and glass production, seemed interesting to study with EPR. Rhyolite and trona were first studied in their natural states, and then their γ-irradiated states were considered. Before γ-irradiation the results indicated the

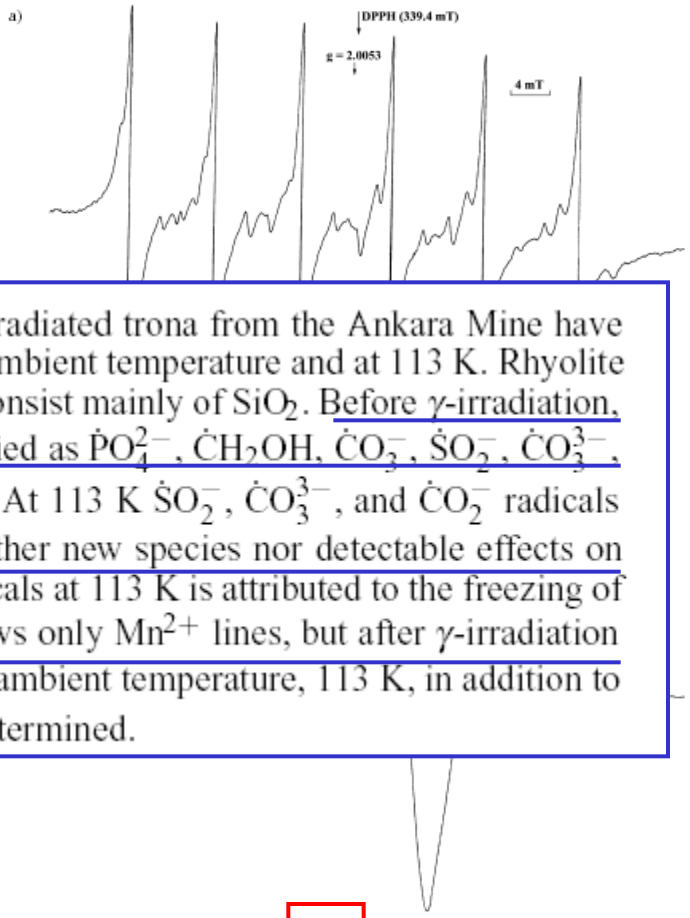

Fig. 4. a) EPR spectrum of trona from the "Ankara Trona Mine" at ambient temperature before the γ-irradiation, and b) after the γ-irradiation.

EPR in Semiconductors

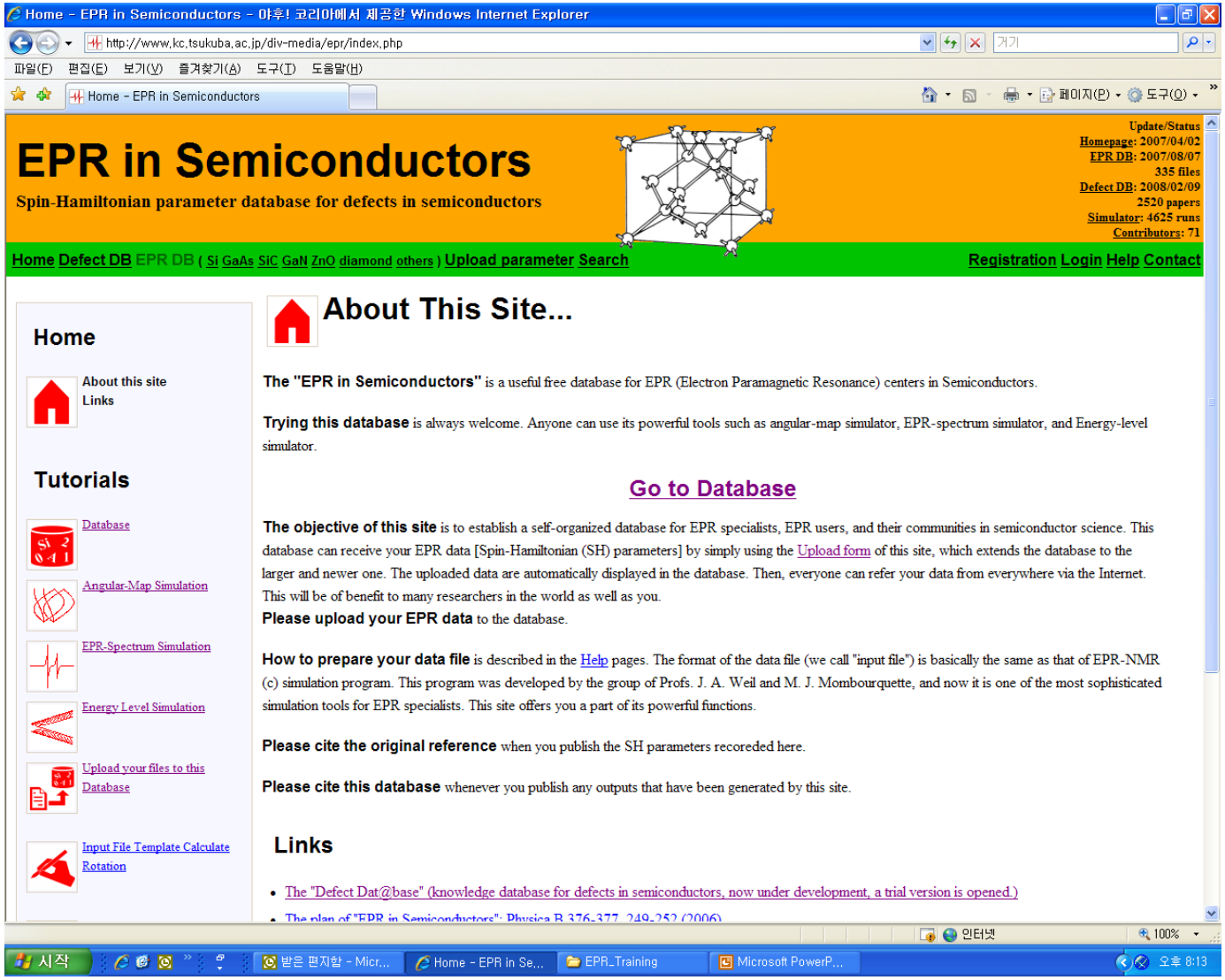

Paramagnetic Centers in Si

Defects (radiation damages, vacancies, dangling bonds), impurities, and small aggregates cause paramagnetic centers.

Triclinic system. (a) Atomic model boron-vacancy complex in silicon, pointgroup 1. (b) Principal axes of the triclinic **g**-tensor. (c) Rotation pattern spectrum Si-G10, $\boldsymbol{B}$ in the $(0\,\bar{1}\,1)$-plane.

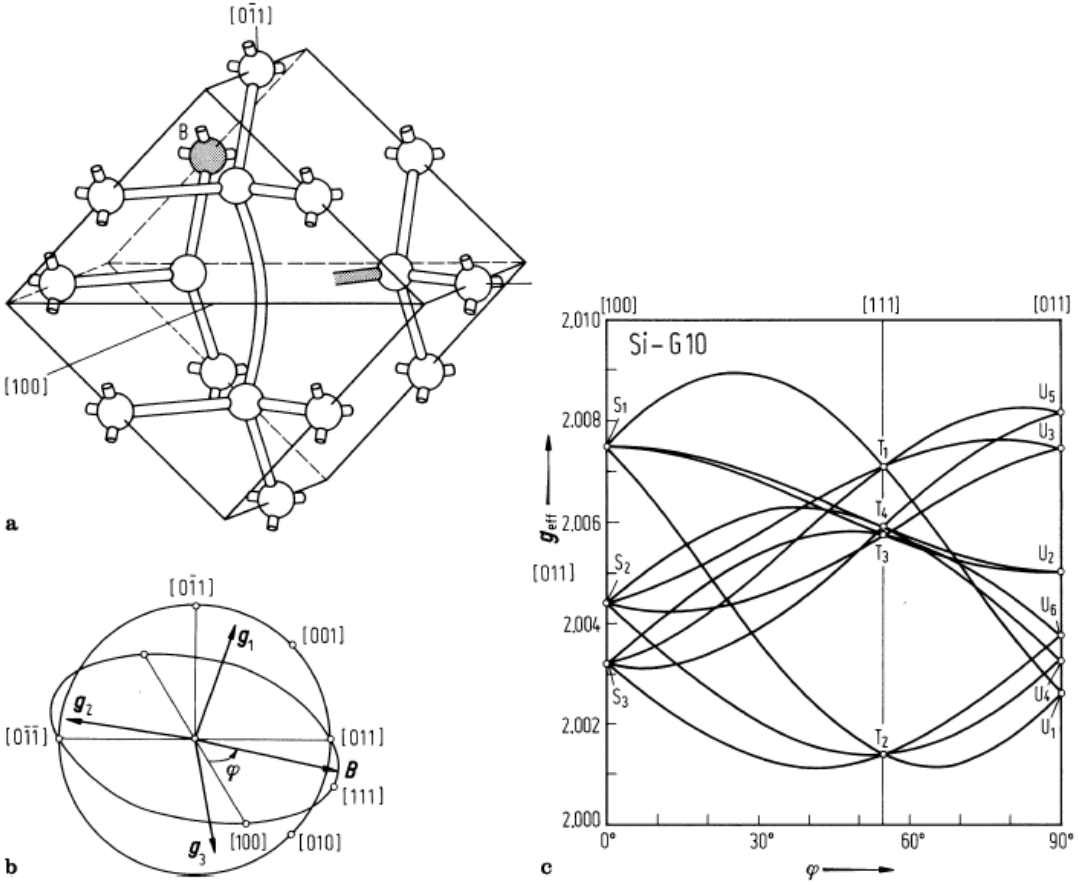

Paramagnetic Centers in Si

Defects (radiation damages, vacancies, dangling bonds), impurities, and small aggregates cause paramagnetic centers.

Monoclinic-I system. (a) Atomic model divacancy in silicon.

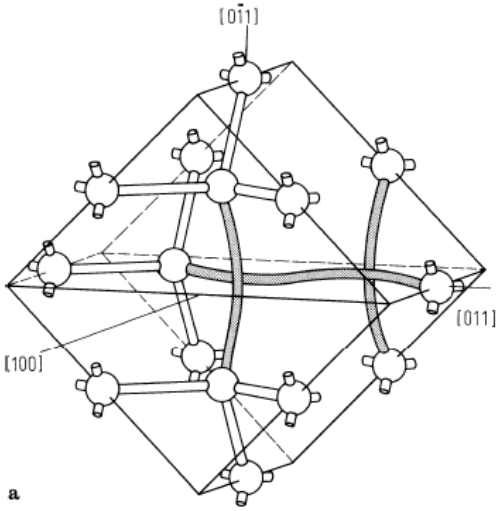

Orthorhombic-I system. (a) Atomic model oxygen-vacancy complex in silicon.

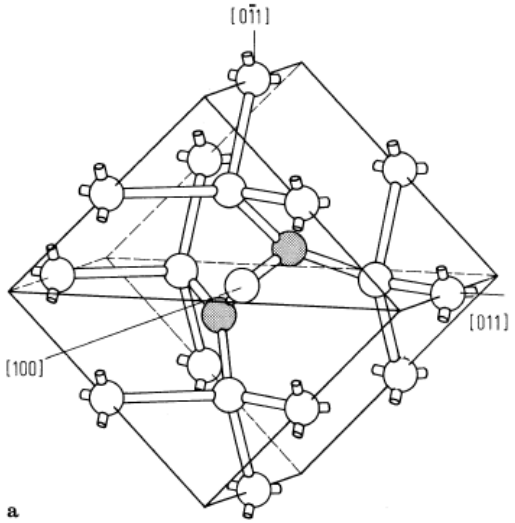

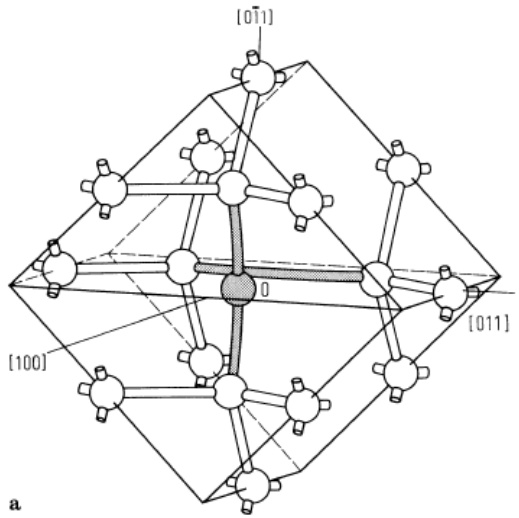

Monoclinic-II system. (a) Atomic model di-interstitial in silicon.

Paramagnetic Centers in Si

Defects (radiation damages, vacancies, dangling bonds), impurities, and small aggregates cause paramagnetic centers.

Orthorhombic-II system. (a) Atomic model diinterstitial in silicon.

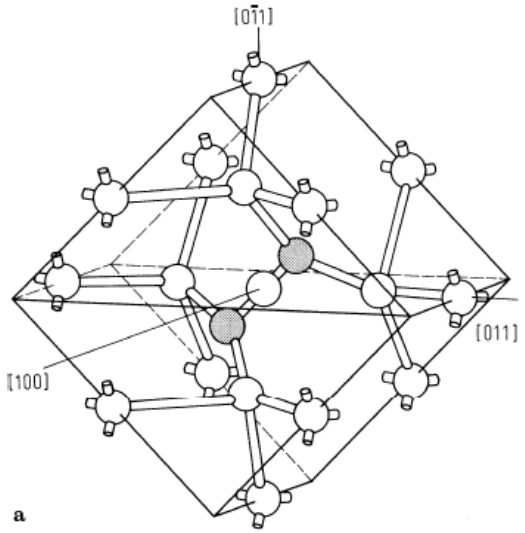

Trigonal system. (a) Atomic model nitrogen in silicon.

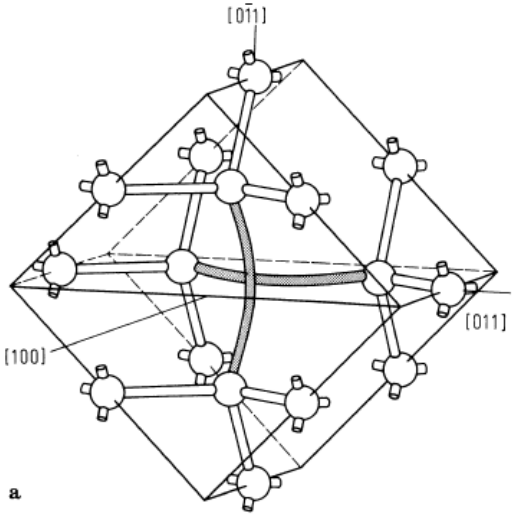

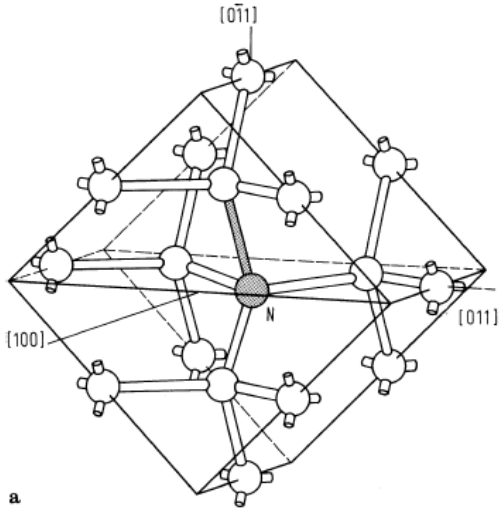

Tetragonal system (a) Atomic model positive vacancy in silicon.

More than 410 paramagnetic centers in Si have been reported.

Dangling Bond in a-Si and a-Si:H

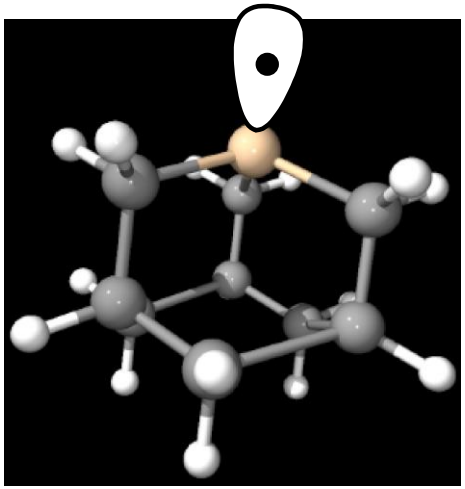

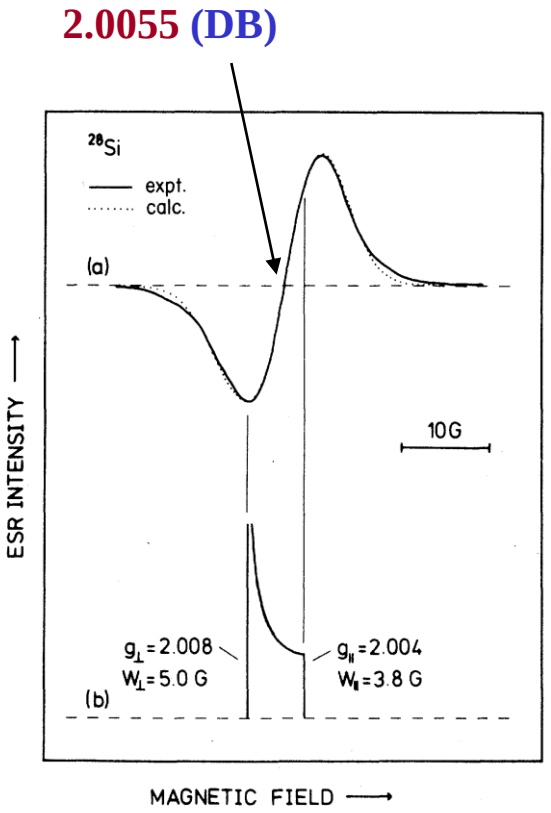

PHYSICAL REVIEW B VOLUME 40, NUMBER 14 15 NOVEMBER 1989-I

Microscopic nature of coordination defects in amorphous silicon

Martin Stutzmann
Max-Planck-Institut für Festkörperforschung, Heisenbergstrasse 1, Postfach 80 06 65, D-7000 Stuttgart 80, Federal Republic of Germany

David K. Biegelsen
Xerox Corporation, Palo Alto Research Center, Palo Alto, California 94304
(Received 9 June 1989)

^{29}Si spectra of the $g=2.0055$ spin resonance in undoped hydrogenated amorphous silicon containing the natural abundance of the ^{29}Si isotope have been measured with a sufficient signal-to-noise ratio to allow a quantitative modeling of the underlying hyperfine and g tensors. These experimental results are used to discuss the microscopic origin of the main deep electronic defect state in *a*-Si.

FIG. 1. Experimental (solid curve) and theoretical (dotted curve) line shape of the $g=2.0055$ spin resonance signal in undoped *a*-Si:H. (b) shows the underlying powder pattern of the g tensor, with principal values $g_\parallel=2.004$ and $g_\perp=2.008$. $W_\parallel$ and $W_\perp$ are the half-widths at half maximum of the Gaussian broadening functions used in the line-shape simulation.

Dangling Bond in a-Si and a-Si:H

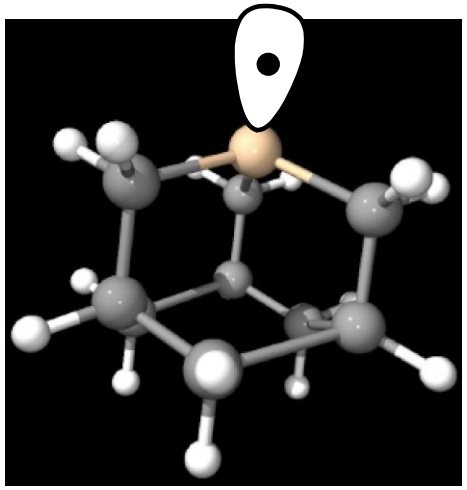

2.0055 (DB)

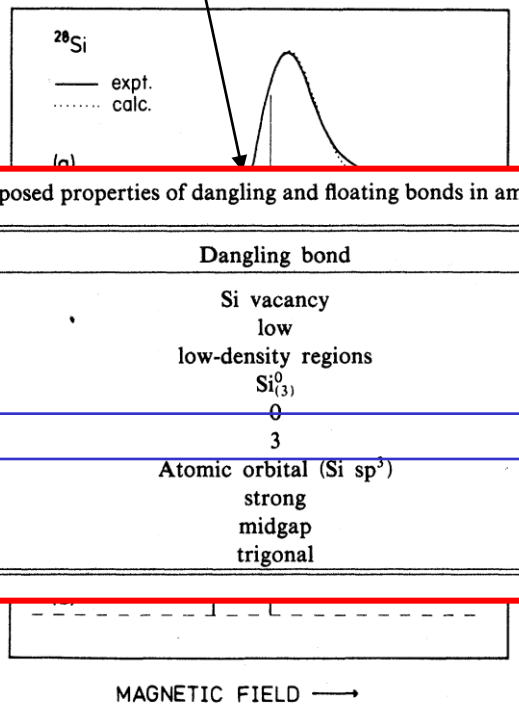

TABLE I. Proposed properties of dangling and floating bonds in amorphous silicon.

	Dangling bond	Floating bond
Crystalline analog	Si vacancy	Si interstitial
Network mobility	low	high
Occurrence in	low-density regions	high-density regions
Chemical notation	$Si^0_{(3)}$	$Si^0_{(5)}$
Charge	0	0
Coordination number	3	5
Orbital type	Atomic orbital (Si sp^3)	Molecular orbital
Localization	strong	weak
Energy level	midgap	midgap
Symmetry	trigonal	?

PHYSICAL REVIEW B VOLUME 40, NUMBER 14 15 NOVEMBER 1989-I

Microscopic nature of coordination defects in amorphous silicon

Martin Stutzmann
Max-Planck-Institut für Festkörperforschung, Heisenbergstrasse 1, Postfach 80 06 65, D-7000 Stuttgart 80, Federal Republic of Germany

David K. Biegelsen
Xerox Corporation, Palo Alto Research Center, Palo Alto, California 94304
(Received 9 June 1989)

^{29}Si spectra of the $g=2.0055$ spin resonance in undoped hydrogenated amorphous silicon containing the natural abundance of the ^{29}Si isotope have been measured with a sufficient signal-to-noise ratio to allow a quantitative modeling of the underlying hyperfine and g tensors. These experimental results are used to discuss the microscopic origin of the main deep electronic defect state in a-Si.

FIG. 1. Experimental (solid curve) and theoretical (dotted curve) line shape of the $g=2.0055$ spin resonance signal in undoped a-Si:H. (b) shows the underlying powder pattern of the g tensor, with principal values $g_{\parallel}=2.004$ and $g_{\perp}=2.008$. $W_{\parallel}$ and $W_{\perp}$ are the half-widths at half maximum of the Gaussian broadening functions used in the line-shape simulation.

Dangling Bond in a-Si and a-Si:H

PHYSICAL REVIEW B VOLUME 59, NUMBER 7 15 FEBRUARY 1999-I

Electron-spin-resonance center of dangling bonds in undoped *a*-Si:H

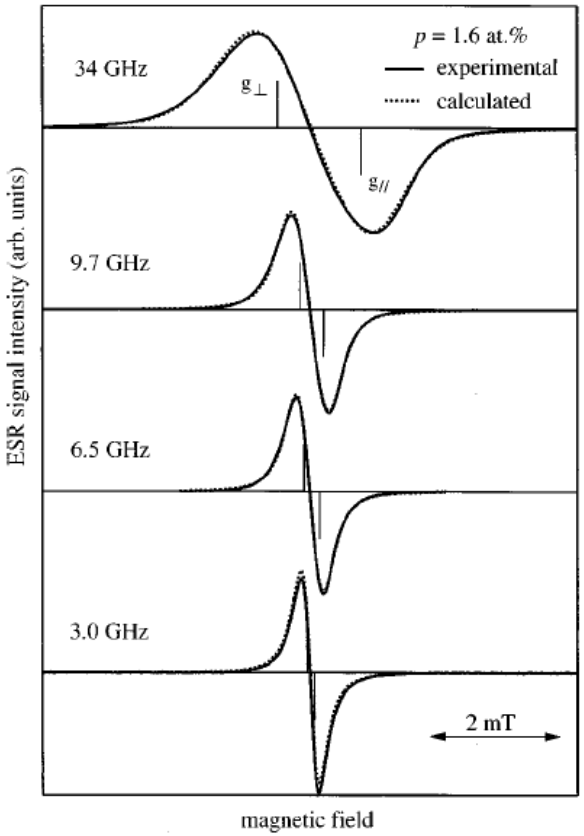

FIG. 3. Cw-ESR spectra of ^{29}Si-diluted undoped *a*-Si:H ($N_s = 9.4\times10^{17}$ cm^{-3}) at various frequencies. Solid and dashed lines indicate experimental and calculated spectra, respectively. The best-fit g parameters are also indicated in the figure.

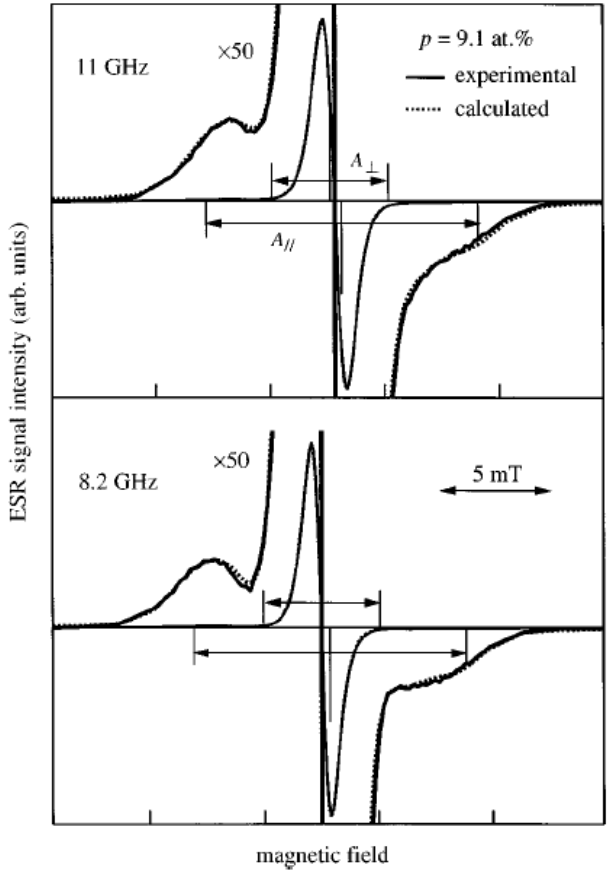

FIG. 5. Echo-detected ESR spectra of ^{29}Si-enriched undoped *a*-Si:H with $N_s = 1.3\times10^{18}$ cm^{-3} at frequencies of 8.2 and 11, GHz (solid lines) and corresponding simulated spectra (dashed lines). The best-fit hf parameters are also indicated in the figure.

Dangling Bond in a-Si and a-Si:H

PHYSICAL REVIEW B

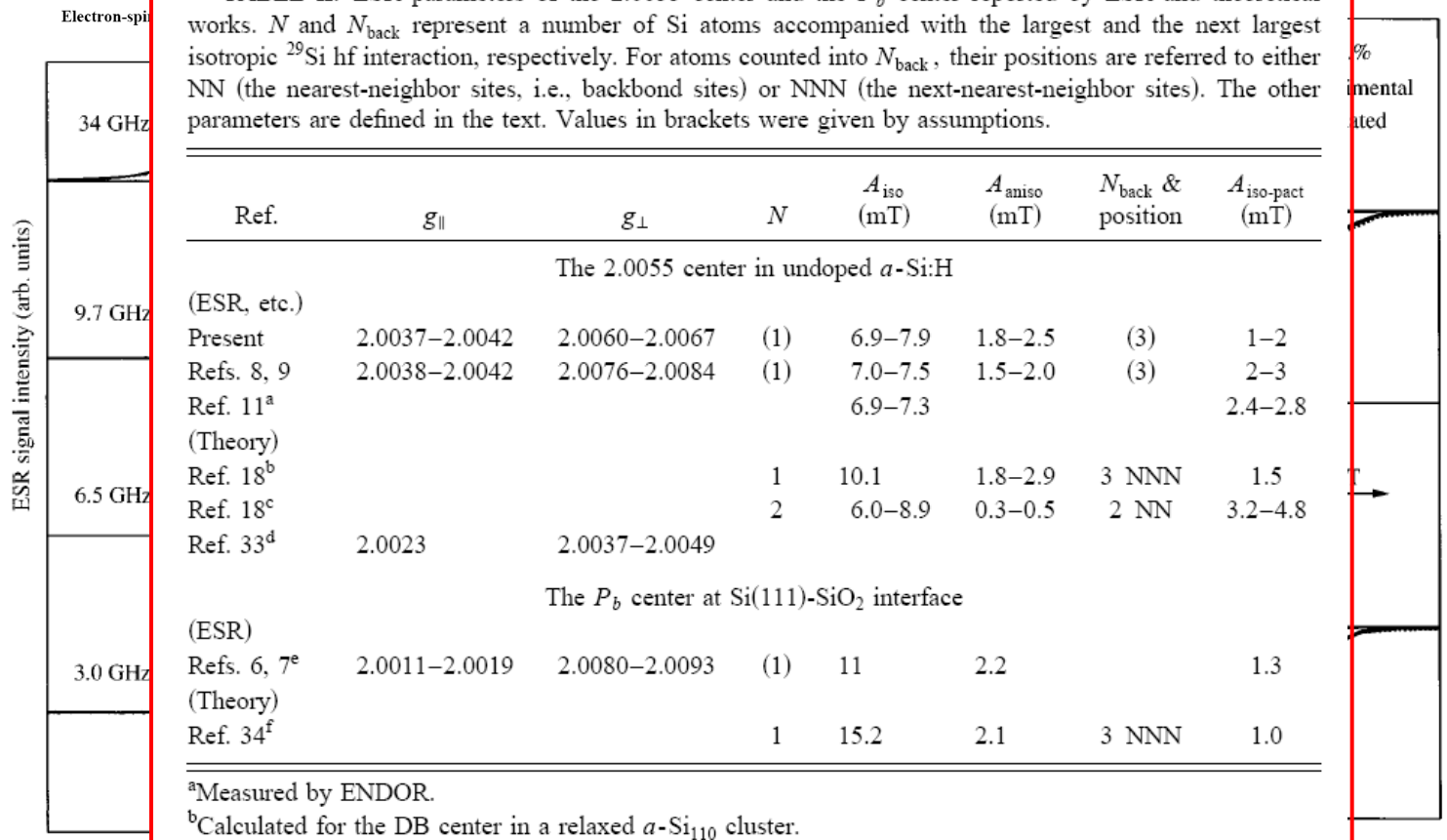

TABLE II. ESR parameters of the 2.0055 center and the P_b center reported by ESR and theoretical works. N and N_{back} represent a number of Si atoms accompanied with the largest and the next largest isotropic ^{29}Si hf interaction, respectively. For atoms counted into N_{back}, their positions are referred to either NN (the nearest-neighbor sites, i.e., backbond sites) or NNN (the next-nearest-neighbor sites). The other parameters are defined in the text. Values in brackets were given by assumptions.

Ref.	$g_{\parallel}$	$g_{\perp}$	N	A_{iso} (mT)	A_{aniso} (mT)	N_{back} & position	$A_{iso\text{-}pact}$ (mT)
			The 2.0055 center in undoped a-Si:H				
(ESR, etc.)							
Present	2.0037–2.0042	2.0060–2.0067	(1)	6.9–7.9	1.8–2.5	(3)	1–2
Refs. 8, 9	2.0038–2.0042	2.0076–2.0084	(1)	7.0–7.5	1.5–2.0	(3)	2–3
Ref. 11[a]				6.9–7.3			2.4–2.8
(Theory)							
Ref. 18[b]			1	10.1	1.8–2.9	3 NNN	1.5
Ref. 18[c]			2	6.0–8.9	0.3–0.5	2 NN	3.2–4.8
Ref. 33[d]	2.0023	2.0037–2.0049					
			The P_b center at Si(111)-SiO_2 interface				
(ESR)							
Refs. 6, 7[e]	2.0011–2.0019	2.0080–2.0093	(1)	11	2.2		1.3
(Theory)							
Ref. 34[f]			1	15.2	2.1	3 NNN	1.0

[a]Measured by ENDOR.
[b]Calculated for the DB center in a relaxed a-Si_{110} cluster.
[c]Calculated for the FB center in relaxed a-Si_{81-86} clusters.
[d]Calculated for the DB center in relaxed a-$Si_{10-22}H_{15-27}$ clusters.
[e]Converted by A_{iso}, A_{aniso} (mT) $= 0.1068 \times A_{iso}$, A_{aniso} (10^{-4} cm^{-1}).
[f]Calculated for the DB center in an unrelaxed $Si_{22}H_{21}/Si_6O_{18}H_6$ cluster with spin polarization.

FIG. 3. Cw-ESR
$= 9.4 \times 10^{17}$ cm^{-3}
indicate experiment
fit g parameters are also indicated in the figure.

hed undoped
and 11, GHz
dashed lines).
The best-fit hf parameters are also indicated in the figure.

Dangling Bond in a-Si and a-Si:H

Appl. Phys. Lett., Vol. 63, No. 12, 20 September 1993

Electron spin resonance study of the dangling bond in amorphous Si and porous Si

T. J. McMahon and Y. Xiao[a)]
National Renewable Energy Laboratory, Golden, Colorado 80401

(Received 1 June 1993; accepted for publication 19 July 1993)

We compare the electron spin resonance (ESR) signal of the dangling bond in porous silicon (PS) layers, produced by electrochemical etching, to the ESR signal from hydrogenated amorphous Si(*a*-Si:H) films. The anisotropy of the ESR signal from PS showed *g* values varying as for the P_b Si/SiO_2 interface dangling bond. The *g* value varies from $g_{\parallel}=2.0020$ to $g_{\perp}=2.0080$ with an inhomogeneously broadened line width increasing from 1.8 to 3.8 G. An ESR powder line, with superhyperfine and strain broadening intrinsic to PS, has more anisotropy in $g_{\parallel}-g_{\perp}$ and less inhomogeneous broadening than does the dangling bond line in *a*-Si:H. No evidence was seen for light-induced metastability on a H-passivated PS film.

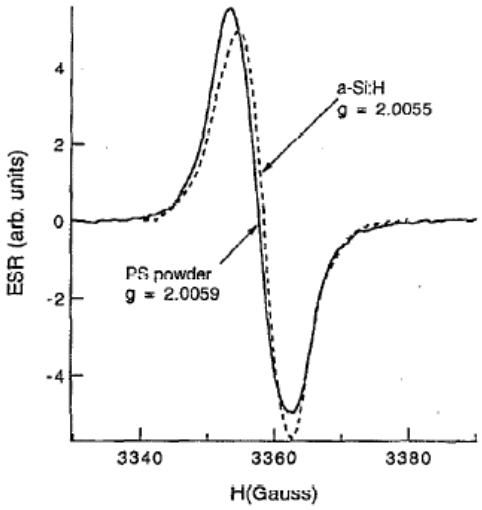

FIG. 4. ESR derivative spectra for a PS powder and *a*-Si:H from Stutzmann and Biegelson (Ref. 6).

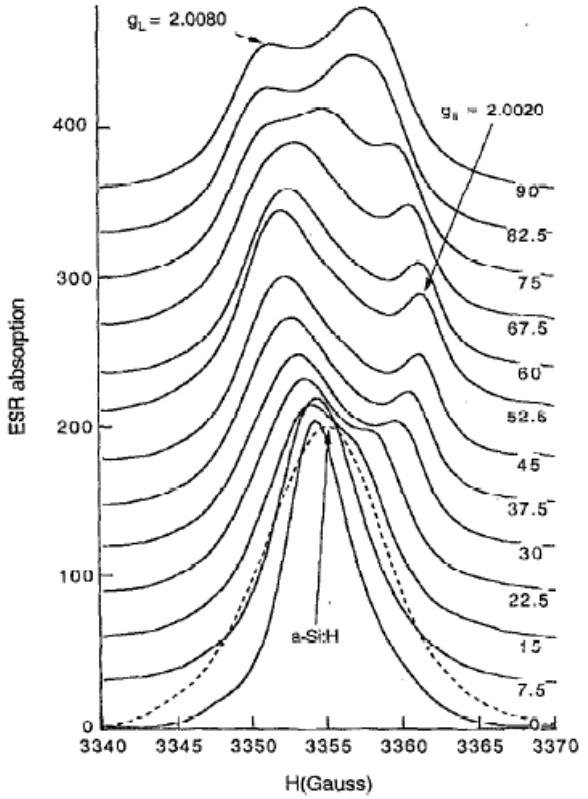

FIG. 2. ESR absorption data of a PS film on a substrate rotated by 7.5° angle increments about the (110) axis, starting at (100).

e^- in CBT and h^+ in VBT

PHYSICAL REVIEW B VOLUME 38, NUMBER 4 1 AUGUST 1988

Nature of paramagnetic centers in *a*-Si and *a*-Si:H

Y. Wu and A. Stesmans
Departement Natuurkunde, Katholieke Universiteit Leuven, B-3030 Leuven, Belgium
(Received 18 March 1987; revised manuscript received 23 December 1987)

A comparative ESR study has been undertaken of various kinds of *a*-Si and *a*-Si:H. Experiments on sputtered samples reveal that the local configuration of the usual dangling-bond (DB) centers ($g \approx 2.0055$) depends on the details of deposition. The g value may gradually be reduced to values as low as 2.0041 as a result of local-structure change. Regarding the $g = 2.004$ signal originated from conduction-band-tail (CBT) states, it is shown that the effective correlation energy (U_{eff}) is large and the temperature dependence of its spin density is due to the presence of donor levels—not due to a small-U_{eff} effect as has previously been concluded. Related to this, ample evidence is provided, indicating that the $g = 2.004$ signal in P-doped *a*-Si:H and the $g = 2.005$ DB line are in fact variants of the same kind of defect. Systematic analysis identifies the $g = 2.004$ CBT states signal with $T_3^- - T_3^+ + e^-$ defect centers thus showing that a great deal of the CBT states are defect states rather than disorder-induced localized states. Regarding the $g = 2.013$ signal in *a*-Si:H, evidence is provided showing that this cannot be associated with valence-band-tail states. Rather it concerns defects positioned at ≈ 0.6 eV above the valence-band mobility edge, whose nature is as yet to be determined. Their presence relates directly or indirectly to H incorporation.

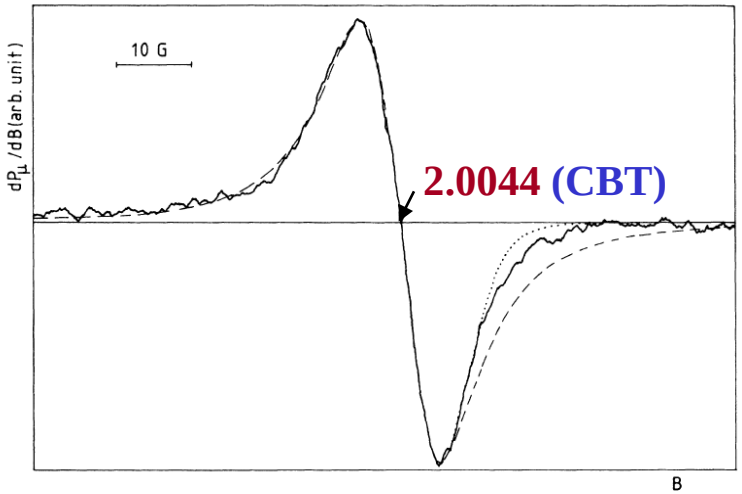

FIG. 1. *K*-band (20.9 GHz) absorption-derivative ESR spectrum (solid line) measured at 77 K with $P_\mu = -2.4$ dBm on P-doped *a*-Si:H glow-discharge deposited in a PH_3 (1 vol %)/SiH_4 (99 vol %) ambient. The dashed and dotted lines represent computer-calculated Lorentzian and Gaussian line shapes, respectively, scaled to the experimental curve at the peak positions.

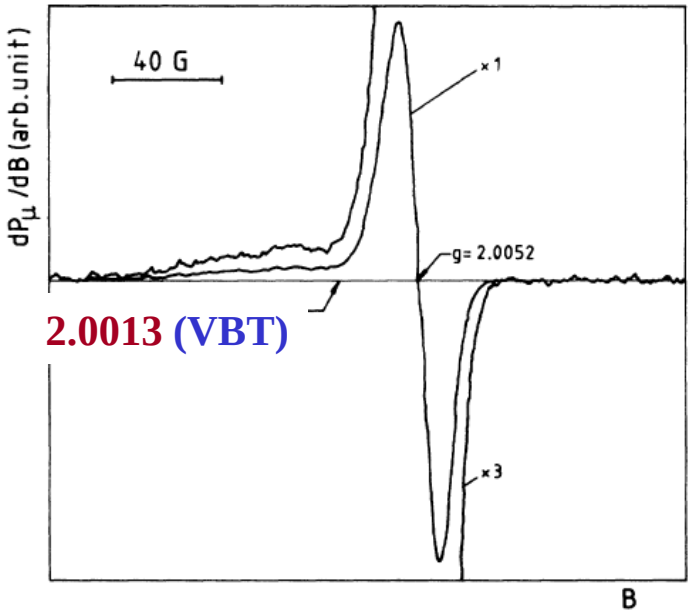

FIG. 3. *K* band absorption-derivative ESR spectrum measured at 295 K with $P_\mu = 0$ dBm on slightly B-doped *a*-Si:H ($E_a = 0.87$ eV). From the three-times-expanded curve, the presence of the broad $g = 2.013$ signal is clearly recognized. This signal may be computer simulated by a symmetric linewidth $l = 1.8$.

Analyses of Si by EPR

5045 J. Appl. Phys. 64 (10), 15 November 1988

Surface and bulk defects in hydrogenated amorphous silicon and silicon-based alloy films

Tatsuo Shimizu, Xixiang Xu,[a] Hideo Kidoh, Akiharu Morimoto, and Minoru Kumeda
Department of Electronics, Faculty of Technology, Kanazawa University, Kanazawa 920, Japan

(Received 24 February 1988; accepted for publication 28 July 1988)

The surface and bulk defects in *a*-Si:H, *a*-$Si_{1-x}C_x$:H, and *a*-$Si_{1-x}N_x$:H films were investigated by electron spin resonance (ESR) and constant photocurrent method. The thickness of the surface defective layer in *a*-Si:H films was determined for the first time by ESR. Applying various surface treatments, the free-surface layer proved to be much more defective than the interface layer. Both surface and bulk defect densities in *a*-$Si_{1-x}C_x$:H and *a*-$Si_{1-x}N_x$:H alloy films were also determined by ESR. The origin of the surface states is discussed, and the experimental results are explained by a simplified model of the distribution of surface defects.

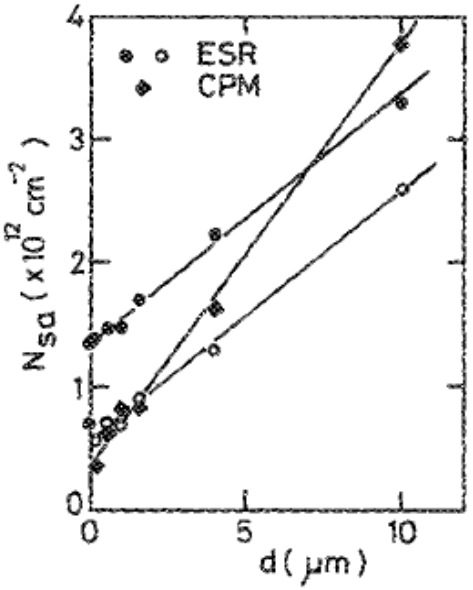

FIG. 1. Thickness dependence of spin densities per area N_{sa}: The circles represent N_{sa} determined by ESR, open ones signify those measured after HF etching, and the diamonds represent those deduced by CPM.

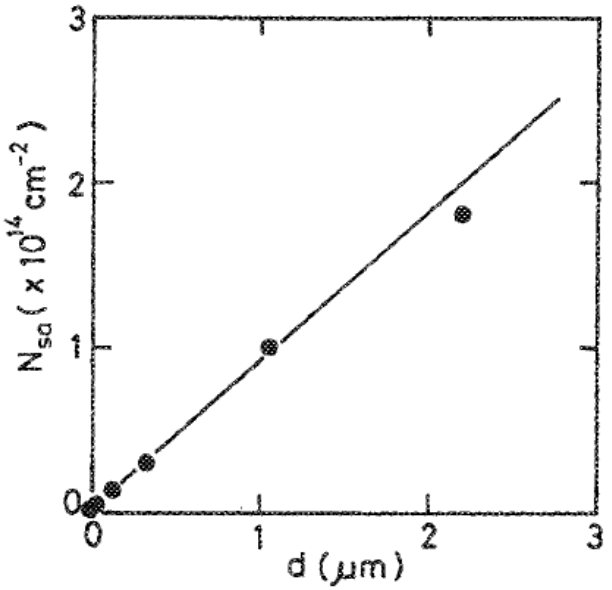

FIG. 3. Spin densities per area N_{sa} measured by ESR for *a*-$Si_{0.82}C_{0.18}$:H alloy films vs thicknesses. The straight line is a visual guide.

Analyses of Si by EPR

PHYSICAL REVIEW B VOLUME 35, NUMBER 18 15 JUNE 1987-II

Thermally and optically induced metastabilities in doped hydrogenated amorphous silicon: ESR studies

M. Stutzmann*
Xerox Corporation, Palo Alto Research Center, Palo Alto, California 94304
(Received 23 October 1986)

Equilibrium and light-induced electron-spin resonance (ESR and LESR) are used to investig the effects of rapid thermal quenching and light soaking on the electronic density of states in do hydrogenated amorphous silicon. Thermal quenching is found to lead to a strong, metastable crease in the density of shallow states. Light soaking of phosphorus-doped *a*-Si:H causes a reve ble increase of occupied neutral-donor levels together with a decrease of electrons in conducti band-tail states. In contrast, *n*-type material doped with arsenic does not show any light-soaking fect. Possible microscopic mechanisms for the observed metastable changes are discussed, and difference between phosphorus- and arsenic-doped *a*-Si:H is explained by changes in the elect trapping behavior deduced from LESR experiments.

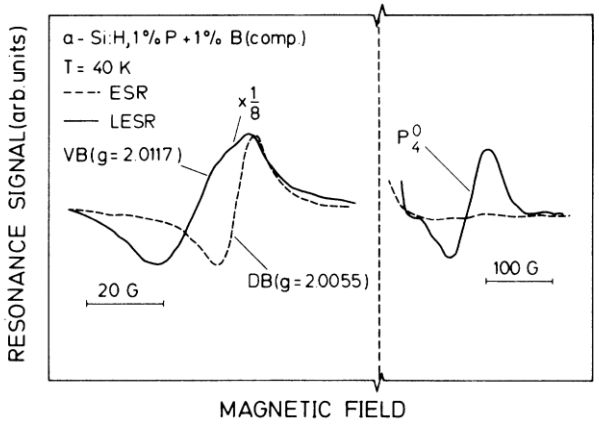

FIG. 7. ESR (dashed curves) and LESR spectra (solid curves) in compensated *a*-Si:H ($[PH_3]=[B_2H_6]=1\%$). VB, DB, and $P_{(4)}^0$ are resonances due to holes in the valence-band tail, neutral dangling bonds, and neutral phosphorus donors. Only the high-field resonance of the $P_{(4)}^0$ hyperfine pair is shown.

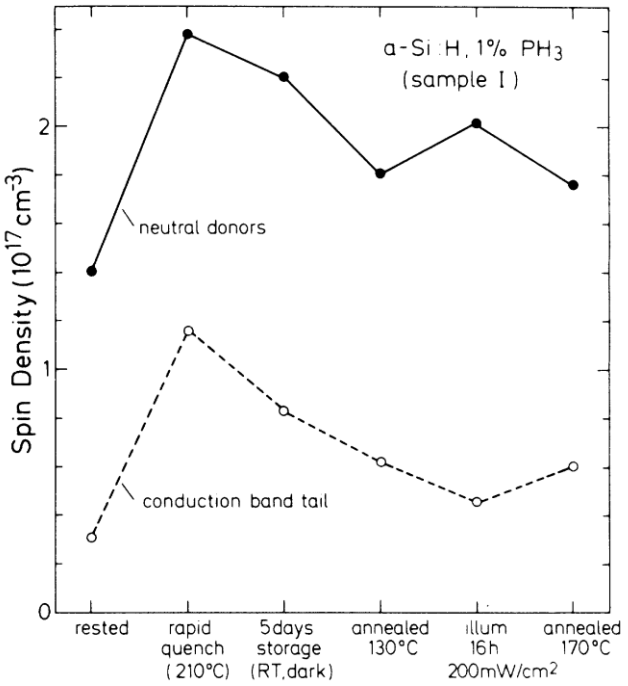

FIG. 1. ESR spin density of neutral donors ($P_{(4)}^0$) and conduction-band-tail states ($g=2.0044$) for various quenching, light-soaking, and annealing treatments in *a*-Si:H doped with 1 vol % PH_3 in the gas phase.

Staebler Wronski Effect

Analyses of Si by EPR

ELSEVIER

Journal of Non-Crystalline Solids 266–269 (2000) 1–22

www.elsevier.com/locate/jnoncrysol

Part I. Amorphous and microcrystalline silicon, germanium and carbon
The Mott Lecture

Spin-dependent processes in amorphous and microcrystalline silicon: a survey

Martin Stutzmann *, Martin S. Brandt, Martin W. Bayerl

Walter Schottky Institut, Technische Universität München, Am Coulombwall, 85748 Garching, Germany

Abstract

Basic concepts of spin-dependent recombination and transport as well as applications in disordered Si-based semiconductors are reviewed. The magnitude of spin-dependent changes in conductivity or luminescence is outlined following the ideas developed by Lepine and Kaplan, Solomon, and Mott. Undoped a-Si:H serves as a model system for the discussion of recombination mechanisms in disordered semiconductors, in particular distant electron–hole pair recombination, recombination via excitonic pairs (spin triplets), and via dangling bond defects. Electrical detection of

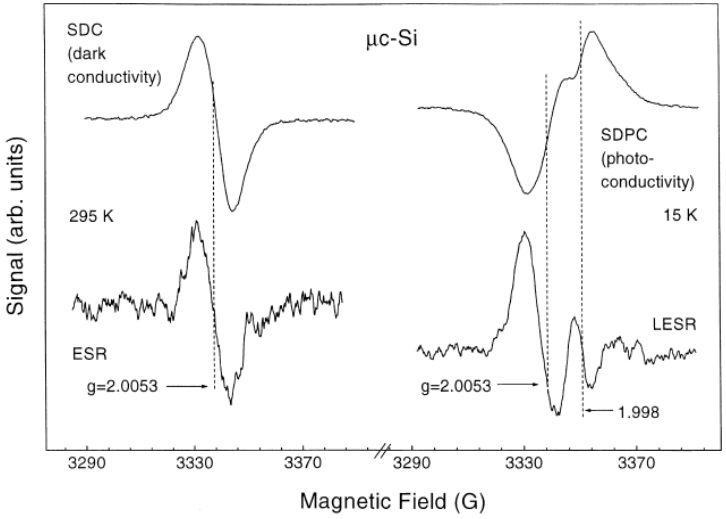

Fig. 11. Left: spin-dependent dark conductivity and equilibrium electron spin resonance spectra of microcrystalline Si at 295 K. Right: spin-dependent photoconductivity and light-induced electron spin resonance of the same sample under illumination at 15 K. Dashed vertical lines indicate the g-values of Si dangling bonds ($g = 2.0053$) and conduction band electrons ($g = 1.998$).

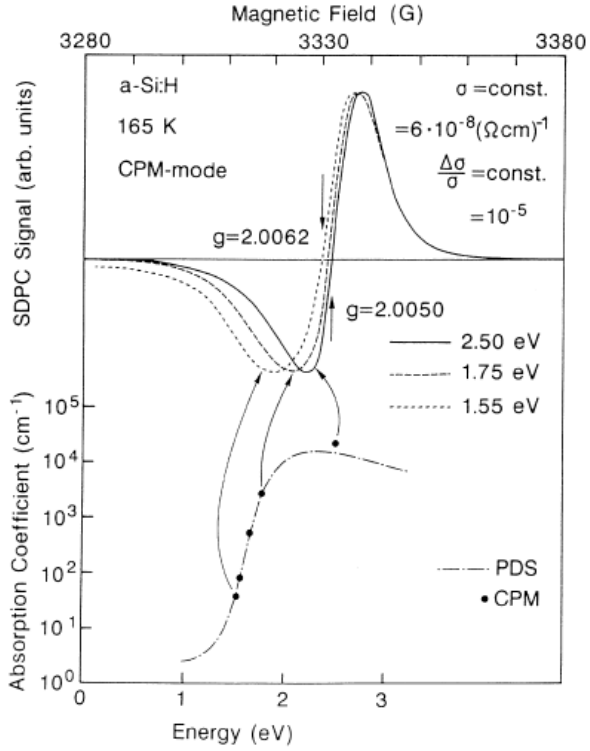

Fig. 7. Dependence of the spin-dependent photoconductivity resonance lineshape on optical excitation energy for undoped a-Si:H at 165 K in the constant photocurrent mode ($\sigma = \text{const}$, $\Delta\sigma/\sigma = \text{const}$). The lower part of the figure shows the absorption coefficient of the sample determined from photothermal deflection spectroscopy (PDS) and the constant photocurrent method (CPM).

Analyses of Si by EPR

ELSEVIER

Journal of Non-Crystalline Solids 266–269 (2000) 1–22

www.elsevier.com/locate/jnoncrysol

Part I. Amorphous and microcrystalline silicon, germanium and carbon
The Mott Lecture

Spin-dependent processes in amorphous and microcrystalline silicon: a survey

Martin Stutzmann *, Martin S. Brandt, Martin W. Bayerl

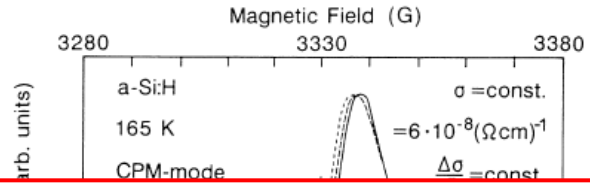

Table 2
Spin dependent transitions in hydrogenated amorphous silicon. e: electron in conduction band tail, h: hole in valence band tail, db: dangling bond

g-value	Linewith (G)	Hyperfine splitting (G)	Technique	Interpretation	Refs.
2.0050 (150 K) 2.0055 (330 K)	≈10	–	EDMR, ODMR	Transition between e and neutral db	[20,21,32–36,42,44]
2.006	≈7	–	EDMR	Hopping in db defect band	[31]
2.009–2.01	≈20	–	EDMR	Hopping of h in VB tail	[21,33–37]
2.007–2.008	≈10	–	EDMR	e–h transition	[34–36]
2.0040–2.0044	≈7	–	EDMR	Hopping of e in CB tail	[16,34–36]
2.003	≈65	250–260	EDMR, ODMR	Hopping in P_4^0 (neutral P-donor) band, P_4^0–db transition, P_4^0–h transition	[34–36,38]
2.003	≈30	125	EDMR, ODMR	P_4^0-donor bound exciton	[34,35,38]
2.008 and ≈4.01	≈210	–	EDMR, ODMR	Exchange coupled e–h pair, triplet-exciton ($\Delta m_s = \pm 1$ and $\Delta m_s = \pm 2$)	[34–36,38–43]
2.0078–2.0085	≈20	–	ODMR	Exchange coupled e–h pair	[42–44]
2.004 and 2.011	≈10 and 20	–	ODMR	Distant e–h pair, Auger recombination	[42,44]
2.0065	≈16	–	ODMR	db–h transition	[42,43,45]
2.011–2.013	≈20	–	ODMR	h in VB tail	[42–45]

Other EPRs of Semiconductors

ELSEVIER

Thin Solid Films 361–362 (2000) 243–247

www.elsevier.com/locate/tsf

Electron-paramagnetic resonance (EPR) and light-induced EPR investigations of $CuGaSe_2$

M. Birkholz*, P. Kanschat, T. Weiss, K. Lips

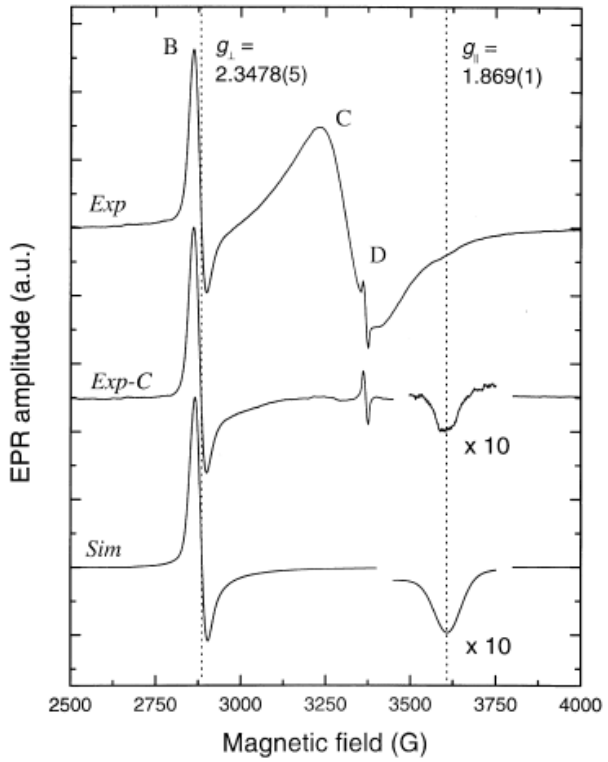

Fig. 1. EPR spectra of $CuGaSe_2$ powder at 5 K. The top spectrum is the measured one, while the middle spectrum has been obtained from experiment by subtracting the C signal. The bottom spectrum gives the simulation of a $S = 1/2$ centre with g-tensor components as indicated.

ELSEVIER

Physica B 308–310 (2001) 66–68

www.elsevier.com/locate/physb

Electron paramagnetic resonance of GaN detected by recombination afterglow

U. Rogulis[1,*], S. Schweizer, J.-M. Spaeth

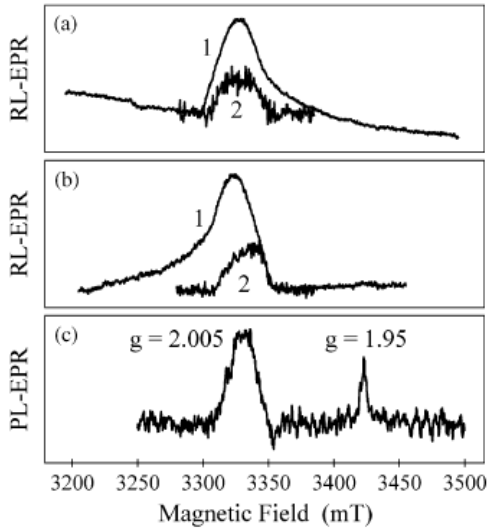

Fig. 2. RL-EPR and PL-EPR spectra of GaN 'lift-off' layer, recorded at 1.5 K in W-band, in the integral luminescence: (a) RL-EPR spectra measured by increasing the magnetic field: curve (1) recorded with an integration time of 6 mT/min, the magnetic field and time dependent background are not subtracted, curve (2) measured as an RL difference by switching 'on' and 'off' the microwave power with a period of 8 s; (b) the same as (a) but measured by decreasing the magnetic field and (c) PL-EPR spectrum of the GaN 'lift-off' layer, recorded at 1.5 K in W-band. The PL was excited at 280 nm and measured with a 380 nm edge filter.

Other EPRs of Semiconductors

ELSEVIER

Physica B 308–310 (2001) 680–683

www.elsevier.com/locate/physb

Neutral and negatively charged silicon vacancies in neutron irradiated SiC: a high-field electron paramagnetic resonance study

P.G. Baranov[a], E.N. Mokhov[a], S.B. Orlinskii[b,*], J. Schmidt[b]

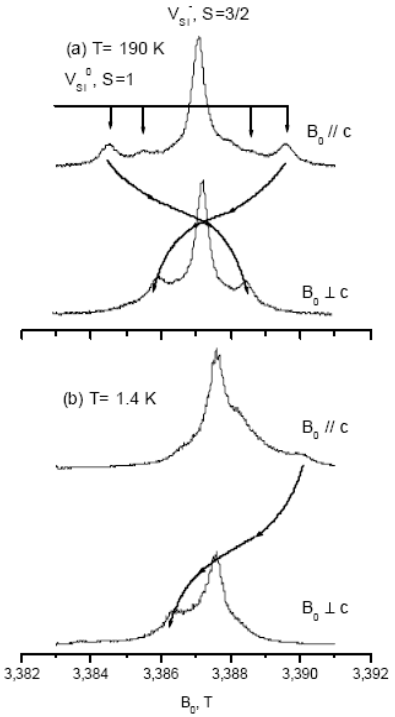

Fig. 1. Angular dependences of the 95 GHz EPR spectra observed in n-irradiated 4H-SiC (10^{18} cm^{-2}) at 190 K (a) and 1.4 K (b). The central line is related to V_{Si}^- whereas the outer, orientation-dependent lines are caused by the triplet state of V_{Si}^0.

PHYSICAL REVIEW B **70**, 235212 (2004)

EPR and theoretical studies of positively charged carbon vacancy in 4*H*-SiC

T. Umeda and J. Isoya
Research Center for Knowledge Communities, University of Tsukuba, Tsukuba 305-8550, Japan

N. Morishita, T. Ohshima, and T. Kamiya
Japan Atomic Energy Research Institute, Takasaki 370-1292, Japan

A. Gali and P. Deák
ment of Atomic Physics, Budapest University of Technology and Economics, Budafoki út 8., H-1111, Budapest, H

N. T. Son and E. Janzén

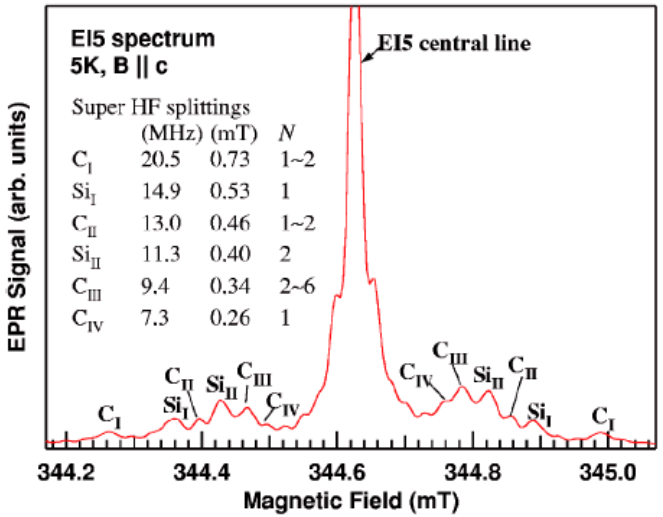

FIG. 5. (Color online) Super HF structures for EI5 (C_{1h}) measured by echo-detected EPR at 9.665 GHz. We have identified their origins (Si or C) by pulsed ENDOR. Also shown in the figure is the number of atoms corresponding to each super HF line (N), which was deduced from a relative intensity of the HF line.

Applications

There are spins everywhere.